Quantum Magnetism in Effective Spin-1/2 Co^{2+}-Triangular Lattice Antiferromagnets

A Dissertation Presented for the

Doctor of Philosophy

Degree

The University of Tennessee, Knoxville

Qing Huang

May 2022

© by Qing Huang, 2022
All Rights Reserved.

To my parents, Lihua Huang and Zhonghuan Hu

Acknowledgements

First and foremost, I would like to thank my advisor, Prof. Haidong Zhou for being an excellent advisor. He spent lots of time training me when I was a naive layperson. And he is always happy to provide guidance and advice, which helps me a lot in my early career as a researcher. I wouldn't be able to finish my Ph.D. without him.

I would also like to thank Dr. Tao Hong from Oak Ridge National Laboratory (ORNL), who co-supervised my Ph.D. work for two years. The discussion between us was always helpful and broadened my horizons in research work.

I am grateful to Prof. Cristian Batista, Prof. Jian Liu, and Prof. Haixuan Xu for serving as my doctoral dissertation committee and for their constructive instructions in my research work.

I wouldn't be able to finish the work described in this dissertation without the collaborations. I would like to express my gratitude to Prof. Jie Ma, Gaoting Lin, Eun Sang Choi, Minseong Lee, Prof. Xuefeng Sun, Na Li, Yiming Qiu, Huibo Cao, Erxi Feng, Wei Tian, Nicolas Butch, Weiwei Xie and all the other collaborators for their contributions to these projects.

I must also acknowledge all my colleagues: Zhiling Dun, Ryan Rawl, Ryan Sinclair, Qiang Chen, Chengkun Xing, Alexander Brassington, Hao Zhang, and Rui Xue for their help, encouragement and collaboration in my Ph.D. life. I am also grateful to all the faculty and staff of the Physics Department for their kind support and advice during my Ph.D. program.

Finally, I wish to thank my parents, family and friends for their support and accompany all my life. I would also thank the cats - Jack, Betsy and Newt - who have lived with me in my Ph.D. life. Their accompany greatly help to soften my pressure.

Preface

Parts of this dissertation are quoted from work during my Ph.D. program published in the last few years. The publication information and corresponding thesis chapters are listed below.

Chapter 3: Evolution of magnetic ordering in the layered structure quantum Heisenberg triangular-lattice antiferromagnet $Ba_3CoSb_2O_9$

N. A. Fortune, Q. Huang, T. Hong, J. Ma, E. S. Choi, S. T. Hannahs, Z. Y. Zhao, X. F. Sun, Y. Takano, and H. D. Zhou

Phys. Rev. B **103**, 184425 (2021)

Chapter 4:

Non-magnetic ion site disorder effects on the quantum magnetism of a spin-1/2 equilateral triangular lattice antiferromagnet

Q. Huang, R. Rawl, W. W. Xie, E. S. Chou, V. S. Zapf, X. X. Ding, C. Mauws, C. R. Wiebe, E. X. Feng, H. B. Cao, W. Tian, J. Ma, Y. Qiu, N. Butch, and H. D. Zhou

Journal of Physics-Condensed Matter **34**, 205401 (2022)

Chapter 5:

Successive Phase Transitions and Multiferroicity in Deformed Triangular-Lattice Antiferromagnets $Ca_3MNb_2O_9$ (M=Co, Ni) with Spatial Anisotropy

Q. Huang, M. Lee, E. S. Choi, J. Ma, C. Dela Cruz, and H. D. Zhou

Submitted to Journal of Solid State Science and Technology

Chapter 6: Possible itinerant excitations and quantum spin state transitions in the effective spin-1/2 triangular lattice antiferromagnet $Na_2BaCo(PO_4)_2$

N. Li, Q. Huang, X. Y. Yue, W. J. Chu, Q. Chen, E. S. Choi, X. Zhao, H. D. Zhou, and X. F. Sun

Co-first author

Nature Communications **11**,4216 (2020)

Abstract

The geometrically frustrated magnetism(GFM) is an energetic field of condensed matter physics. The frontier of the GFM research has been greatly expanded from the prediction of the exotic quantum spin liquid to the ubiquitous topological physics. As one of the simplest geometrically frustrated systems, the spin 1/2 triangular antiferromagnet(TLAF) system has recently attracted lots of attention. In this dissertation, a series of Co^{2+}-based effective spin 1/2 TLAFs with single crystalline form were systematically studied by DC, AC magnetic susceptibility, magnetic torque, specific heat, thermal conductivity, and neutron scattering measurements. In chapters 1 and 2, the background material of TLAFs and the experimental methods are introduced. From Chapter 3 to 6, the research results of four Co^2+-based effective spin 1/2 TLAFs are reported. In chapter 3, the phase diagrams as functions of the magnetic field, temperature, and the orientation of field to the crystal axis were mapped for $Ba_3CoSb_2O_9$(BSCO) with easy plane anisotropy. In chapter 4, we probed the effect of nonmagnetic site disorder in Sr-doped BSCO $Ba_2.87Sr_0.13CoSb_2O_9$. In chapter 5, an isosceles triangular lattice system $Ca_3CoNb_2O_9$(CCNO) was studied to reveal the effect of lattice distortion in TLAFs. And in chapter 6, we reported the observation of the possible itinerant excitation and quantum spin state transitions in $Na_2BaCo(PO_4)_2$(NBCPO).

Table of Contents

1 Introduction **1**

1.1 GFM in spin 1/2 TLAFs 1

1.2 Triple-perovskite sample $Ba_3CoSb_2O_9$ 4

1.2.1 Quantum spin state transitions 4

1.2.2 Spin dynamics 5

1.2.3 Other compounds in the triple-perovskite family 6

2 Experimental methods **7**

2.1 Sample synthesis 7

2.1.1 Solid state reaction method 7

2.1.2 Flux method 7

2.1.3 Floating zone method 8

2.2 X-ray diffraction and Laue measurement 8

2.3 Specific heat 9

2.4 DC susceptibility and magnetization 9

2.5 AC susceptibility 10

2.6 Dielectric constant and polarization 10

2.7 Thermal conductivity 11

2.8 Neutron scattering 12

2.8.1 Powder neutron diffraction 12

2.8.2 Single crystal neutron diffraction 12

2.8.3 Inelastic Neutron scattering 13

3 $Ba_3CoSb_2O_9$ **14**

3.1 Motivation . . . 14

3.2 Sample preparation . . . 15

3.3 Results . . . 15

3.4 Phases diagrams and discussion . . . 17

3.4.1 H ∥ a . . . 17

3.4.2 H ∥ c . . . 18

3.4.3 From H ∥ a to H ∥ c . . . 19

3.5 Summary . . . 19

4 $Ba_{2.87}Sr_{0.13}CoSb_2O_9$ **21**

4.1 Motivation . . . 21

4.2 Sample preparation . . . 22

4.3 Crystal and magnetic structure . . . 23

4.4 DC and AC magnetic susceptibility . . . 24

4.5 Specific heat . . . 25

4.6 Magnetic phase diagrams . . . 25

4.7 Inelastic neutron scattering spectra . . . 26

4.8 Discussions . . . 26

4.9 Summary . . . 29

5 $Ca_3CoNb_2O_9$ **30**

5.1 Motivation . . . 30

5.2 Sample preparation . . . 31

5.3 Lattice and magnetic structure . . . 31

5.4 DC and AC susceptibility . . . 32

5.5 Specific heat . . . 34

5.6 Dielectric constant . . . 34

5.7 Discussion . . . 35

5.8 Summary . . . 37

6 $Na_2BaCo(PO_4)_2$ **38**

6.1 Motivation . . . 38

6.2 Sample preparation . . . 39

6.3 Magnetic susceptibility . . . 39

6.4 Thermal conductivity . . . 39

6.5 Specific heat . . . 40

6.6 Residual thermal conductivity . . . 41

6.7 Field dependence of thermal conductivity and AC susceptibility . . . 43

6.8 Phase diagram . . . 44

6.9 Summary . . . 45

7 Summary **46**

Bibliography **48**

List of Publications **67**

Appendix **71**

Vita **108**

List of Tables

4.1 Data of crystallographic refinement for Sr-BCSO at 296 (2)K 72

4.2 Atomic coordinates and equivalent isotropic displacement parameters of Sr-BCSO system.(U_{eq} is defined as one-third of the trace of the orthogonalized U_{ij} tensor ($Å^2$)) 73

5.1 Structural parameters of CCNO at 300K 74

List of Figures

1.1 The illustration of geometrical frustration in triangular lattice (a) and kagome lattice (b). 75

1.2 The illustration of resonating valence bond state. 76

1.3 Theoretically proposed spin ordering states for the quantum $S = 1/2$ Heisenberg triangular antiferromagnet in the 2D limit. (a-f) are 120-degree, Y, UUD, V, umbrella, and Ψ (fan) phase, respectively. The figures are adopted from [1]. 77

1.4 Theoretically proposed spin orderings for a quantum $S = 1/2$ Heisenberg triangular antiferromagnet with interlayer coupling in a 2 layer model. Spins 1 - 3 correspond to layer 1; spins 4 - 6 to layer 2. The orderings are named as follows: (a) the zero field 120° structure, (b) distorted combined Y ,(c) alternating ordered Y, (d) parallel ordered Y, (e) UUD, (f) V, (g) distorted V, (h) V′, (i) staggered V′, (j) ψ (fan) spin structure. Ordering (k) corresponds to the classically expected cone (umbrella) phase. The figures are adopted from [1]. 78

2.1 The illustration of IR-image furnace and floating zone method. 79

3.1 For all data, H ∥ a-axis. Field dependence of C_p (a) and τ (b); Field dependence (c) and temperature dependence (d) of κ;(e) Field dependence of the peak intensity for magnetic Bragg peaks [1/3 1/3 0] and [1/3, 1/3, 2] measured by neutron diffraction; (f) Temperature dependence of the peak intensity for [1/3, 1/3, 0], [1/3, 1/3, 1] and [1/3, 1/3, 2]. 80

3.2 For all data, H ∥ c-axis. Field dependence of C_p (a) and τ (b); Field dependence (c) and temperature dependence (d) of κ. 81

3.3 Field dependence of C_p (a), τ (b) and its derivative (c) and (d) when H rotates from a-axis (90°) to c-axis (0°). All data were obtained at $T = 0.32$ K. . . . 82
3.4 (a) The magnetic phase diagram with H ∥ a-axis. (b) The magnetic phase diagram with H ∥ c-axis. (c) The angle-dependent phase diagram at 0.32 K based on experiment data. The x-coordinate represents the angle between the a and c-axis; (d) the theoretically calculated phase boundaries. 83
4.1 (a) An illustration of the crystallographic structure of Sr-BCSO. (b) An illustration of the canted 120-degree spin structure. 84
4.2 (a) The temperature dependence of the intensity for a magnetic peak [1/3 1/3 1] and [1/3 1/3 0]. The intensity of [1/3 1/3 0] is timed by a factor 20 for the visibility. Error bars represent one standard deviation. (b) The refinement result of the single crystal neutron diffraction data with a canted 120-degree spin structure. 85
4.3 The field dependence of the intensity for magnetic peak [1/3 1/3 1] (a) and [1/3 1/3 2] (b) measured at 1.5 K. Error bars represent one standard deviation. 86
4.4 The temperature dependence of the DC susceptibility under different magnetic fields with H ∥ ab-plane (a, b) and H ∥ c-axis (d, e) for Sr-BCSO. The second-order derivative of the χ-T curves under high magnetic fields for H ∥ ab-plane (c) and H ∥ c-axis (f). 87
4.5 The dc magnetization (black line) and its derivative (red line) measured at 1.5 K with H ∥ ab-plane (a) and H ∥ c-axis (b). The dashed line represents the Van Vleck paramagnetic background. 88
4.6 The AC susceptibility measured at 50 mK with H ∥ ab-plane (a) and c-axis (b). 89
4.7 The temperature dependence of C_p measured with H ∥ ab-plane (a) and H ∥ c-axis (b). 90
4.8 The magnetic phase diagram for H ∥ ab-plane (a) and H ∥ c-axis (b). 91

4.9 The zero field INS spectra along the [H H 1] (a) and [1/3 1/3 L] (b) directions, which were measured at 300 mK using the wavelength $\lambda = 5\,\text{Å}$; For (c, d), the zero field INS spectra were measured at 300 mK using the wavelength $\lambda = 3.5\,\text{Å}$. The INS spectra measured at 1.6 K with H ∥ ab-plane and μ_0H = 9 T along [H H 1] (e) and [1/3 1/3 L] (f) directions. 92

4.10 (a) The energy cut at [1/3 1/3 1] as the function of magnetic field with H ∥ ab-plane. Comparison of the energy cut between Sr-BCSO and BCSO at the [1/3 1/3 1] position at zero field (b) and applied field (c), which is 9 T for Sr-BCSO and 11.5 T for BCSO. 93

5.1 (a) Neutron diffraction patterns (black dots) and Rietveld refinements (red line) for CCNO at 300 K. Blue line at the bottom of each panel is the difference curve. The green and red ticks are the reflection positions for the nuclear phases and Al-can, respectively. The refinements were done with the P121/c1 space group. (b) The lattice structure with the Co-triangular lattice of CCNO. The blue and yellow spheres represent Co1 and Co2 on two different sites, respectively. 94

5.2 (a) Illustration of the transform of the unit cell from monoclinic (blue) to hexagonal (red) for CCNO. Here only the Co1 (blue sphere) and Co2 (yellow sphere) are plotted. (b) An illustration of spin structure proposed for CCNO. 95

5.3 (a) The isothermal dc magnetization curve and its derivative (dM/dH) of CCNO measured at 1.0 K and 1.5 K with H ∥ a-axis. (b) Temperature dependence of the dc susceptibility measured at 0.1 T. Inset: the inverse dc susceptibility. The lines are Curie-Weiss fittings at two different temperature regions ($T \leq 50$ K for the green line and 100 K $\leq T \leq$ 300 K for the red line). 96

5.4 (a) The temperature dependence of ac susceptibility measured with dc field H ∥ a-axis. (b) The temperature dependence of ac susceptibility measured with dc field H ∥ c*-axis. (c) The field dependence of ac susceptibility with the dc field H ∥ a-axis. 97

5.5 The temperature dependence of specific heat of CCNO with H ∥ a-axis (a) and H ∥ c*-axis (b). 98

5.6 Temperature dependence of $\epsilon'(T)$ of CCNO at different fields with H ∥ a (a) and H ∥ c*-axis (b). Data was offset by 0.003. The field dependence of ϵ'(H) at different temperatures with H ∥ a-axis (c) and H ∥ c*-axis(d). Inset of (c): the derivative of the ϵ' with respect field. 99

5.7 (a)-(d) Temperature dependence of the pyroelectric current of CNNO with H and E applied along the different crystallographic directions. (e)-(h) Temperature dependence of polarization of CNNO with H and E applied along different directions. 100

5.8 The magnetic phase diagrams of CCNO with H ∥ a-axis (a) and H ∥ c*-axis (b). 101

6.1 (a) The crystallographic structure. (b) The triangular lattice of Co^{2+} ions in the ab plane. (c) The inverse of the DC susceptibility measured with 0.1 T magnetic field along the ab plane. The solid lines are the Curie–Weiss fittings to high temperature or low-temperature data. 102

6.2 (a) The zero-field thermal conductivity of NBCPO in temperature range of 70 mK – 30 K. The heat current is along the a axis. The peak at 12 K is the so-called phonon peak. Also shown are the thermal conductivity in 14 T magnetic field along the c or the a axis. In most of this temperature region, high magnetic field enhances the thermal conductivity. (b) Data in zero field plotted in κ/T vs T^2. The solid line is a linear fit of the data at $T < 700$ mK. A nonzero residual thermal conductivity $\kappa_0/T = 0.0062$ WK^2 m^1 is resolved. The inset shows a magnified view of the lowest-temperature data. There is a very weak anomaly at $T < 100$ mK. (c), (d) Thermal conductivity in 14 T magnetic field plotted as κ/T vs T^2. The solid lines are a linear fits for data at $T < 550$ mK (for H ∥ c) and at $T < 500$ mK (for H ∥ a). There is no residual term ($\kappa_0/T = 0$). 103

6.3 (a), (c) The zero-field data and those in different magnetic fields along the c axis or the a axis. The temperature range is 50 mK to 4 K. (b), (d) The magnetic entropy for H ∥ c and H ∥ a, obtained by integrating the magnetic specific heat. 104

6.4 (a) Specific heat of NBCPO single crystal at 1.9 – 40 K and in various magnetic fields up to 14 T. (b) Zero-field data. The solid line shows the fitting to data at $T > 10$ K by using the formula of phonon specific heat, $C_{ph} = \beta T^3 + \beta_5 T^5 + \beta_7 T^7$. 104

6.5 (a) Magnetic-field dependence of thermal conductivity at different temperatures. For clarifying, the 151 mK, 252 mK and 380 mK curves are shifted upward by 0.5, 1.0 and 1.5, respectively. At 92 mK, there are four minima indicated by arrows. With increasing temperature, the minima become weaker and disappear above 380 mK. (b) Temperature dependence of κ in different fields. At low fields of 0.5 and 1 T, there is a clear slope change of $\kappa(T)$ curves around 310 mK, which has good correspondence to the specific-heat anomaly. (c) AC magnetic susceptibility at different temperatures. There are three peaks in the low-temperature curves. (d) Magnetization curves obtained by integrating the AC susceptibility data and renormalized with the 3 T value. The lower dashed line indicates a $\sim$1/3 plateau and the upper dashed line indicates the Van Vleck paramagnetic background. 105

6.6 (a) Magnetic-field dependence of thermal conductivity at different temperatures. For clarifying, the 151 mK, 252 mK and 380 mK curves are shifted upward by 0.5, 1.0 and 1.5, respectively. At very low temperatures, there are two minima on the κ(H) curves which disappear above 252 mK. (b) Temperature dependence of κ in different fields. No clear anomaly is observed. (c) AC magnetic susceptibility at different temperatures. There are two peaks in the low-temperature curves. (d) Magnetization curves obtained by integrating the AC susceptibility data and renormalized with the 3 T value. The dashed line indicates the Van Vleck paramagnetic background. 106

6.7 The magnetic phase diagrams of NBCPO for H ∥ c (a) and H ∥ a (b). The data points are obtained from the AC susceptibility (AC), specific heat (C_p) and temperature or field dependence of thermal conductivity ($\kappa(T)$ and κ(H)) measurements. The dashed lines are phase boundaries. For H ∥ c, there are four phases (I, II, III, and IV) in the low-temperature and low-field region. Whereas, there are two phase (I and II) at low-temperature and low-field for H ∥ a. The dashed lines are a guide to the eye. 107

Chapter 1

Introduction

In this chapter, I intend to give a brief introduction to geometrically frustrated magnetism (GFM). I will start with a general discussion of geometrical frustration in the triangular lattice antiferromagnets(TLAFs). A brief review of theoretical and experimental studies on TLAF systems will be provided. Then one specific TLAF, the triple perovskite, will be introduced in detail, including the well-studied $Ba_3CoSb_2O_9$(BCSO). This compound leads to all the other related systems that we studied in this dissertation.

1.1 GFM in spin 1/2 TLAFs

In physics, frustration, which often leads to exotic properties of materials, refers to the presence of competing forces that can't be simultaneously satisfied. Frustration in magnetism means localized magnetic moments, or spins, interact through competing exchange interactions that can't be simultaneously satisfied. In antiferromagnets, frustration usually origins from geometry. As shown in figure 1.1 (all the figures and tables are in Appendix), on the triangular (a) and kagome (b) lattice, the three spins on a triangular cannot be antiparallel to each other simultaneously. When a pair of spins are aligned antiparallelly through a bond, the third spin is frustrated. Then depending on the circumstance, the spins fluctuate, or order, in a less obvious manner.

As one of the simplest geometrically frustrated systems, the spin 1/2 TLAFs have attracted extensive theoretical and experimental studies due to their exotic quantum magnetism. One

celebrated example is the two dimensional (2D) gapless quantum spin liquid (QSL) state[2, 3, 4, 5]. Historically, it was pointed out that Ising spins residing on a triangular lattice fail to order by leaving massive residual entropy even at zero temperature, an apparent violation of the third law of thermodynamics[6]. Anderson predicted QSL state, an exotic ground state in the context of strongly fluctuating antiferromagnetically correlated S-1/2 Heisenberg spins. As shown in Figure 1.2, in such a state, each pair of spin can form a singlet and the ground state is the superposition of all the specific ways of forming. So it can also be called the resonating valence bond state. Anderson further proposed it as a possible mechanism to realize high-T_c superconductivity in a triangular lattice system [7, 8]. Moreover, the recent researches have shown that the 2D gapless QSL state can host non-abelian quasiparticle[9] and fractional excitations[10, 11] known as spinons[12, 13].

Experimentally, there are three widely accepted evidences that can suggest the existence of spinons, including (i) a broad magnetic continuum in the inelastic neutron scattering(INS) spectrum[10, 14, 15], (ii) a large magnetic specific heat with power law ($C \sim T^{\alpha}$) temperature dependence[16, 17, 18], (iii) a non-zero residual thermal conductivity κ_0/T in the zero-temperature limit[19, 20, 21, 22]. For example, the heavily studied spin 1/2 TLAF system $YbMgGaO_4$(YMGO) has been argued to have a QSL state. Because earlier studies on YMGO show that: its inelastic neutron scattering (INS) spectrum has a continuum mode [15, 14, 23, 24], the specific heat behaves as $C_p \sim T^{0.7}$ [25], its Muon spin relaxation (MuSR) rate exhibits a temperature-independent plateau [26], and its DC susceptibility saturates below $0.1 \sim 0.2$ K[27]. All of these results suggest that YMGO has a gapless QSL state. More recently, the reports including no residual κ_0/T term on the thermal conductivity observed[28] and the frequency dependent AC susceptibility peak[29], suggest a glassy ground state in YMGO. However, a most recent study on high quality YMGO single crystals reveals a residual κ_0/T term and series of quantum spin state transitions at the zero temperature limit. It suggests the survival of itinerant excitations and quantum spin state transitions in YMGO[30]. So the existence of QSL state in YMGO is still controversial.

Another example of exotic magnetism in spin 1/2 TLAFs is the quantum spin state transitions(QSSTs). In isotopic 2D limit, many theories suggested that TLAFs with nearest-neighbor(NN) interaction have a long-range ordered state at zero temperature with reduced

sublattice magnetizations[31, 32, 33, 34]. The spin structure of the long-range ordered state is called a coplanar 120-degree state, in which three spins point at 120 degrees from one another in the same plane, as shown in Figure 1.3(a). In the presence of an external magnetic field, theories predict that the ground state should satisfy the constraint of M = H/(3J), where M, H, and J are net magnetization of a triangular plaquette, magnetic field, and NN exchange interaction, respectively[35, 36]. However, a unique minimum energy state cannot be selected under this constraint. Consequently, massive degeneracies continue until the magnetization is fully saturated. Therefore, the ground state at a finite magnetic field of a spin 1/2 TLAF is ultimately determined by quantum fluctuations[37, 38].

With the increase of the external magnetic field, theory predicts the 120-degree state will firstly evolve into a coplanar phase in which the spins order in the shape of a Y, as shown in Figure 1.3(b). The two spins forming the top branches of the Y are driven by the magnetic field. The angle between them is thus smaller than 120 degrees, and its exact value depends on the strength of the applied magnetic field [39].

At a stronger applied field which is around 3/10 of the saturation magnetic field H_s, the system is predicted to enter the collinear up-up-down(UUD) spin state shown in Figure 1.3(c). In the UUD phase, two of the spins are parallel to the magnetic field while the other one is antiparallel to the field. So the UUD phase usually exhibits itself as a plateau in the magnetization curve at 1/3 of the saturation moment.

Another coplanar spin ordering phase named as V phase is predicted under higher magnetic field. In this phase, two of the three spins are parallel to each other, forming a rotated V shape, as shown in Figure 1.3(d). The system will then finally evolve into the fully polarized state at the saturation field.

In most compounds studied in this dissertation, a weak easy-plane anisotropy aligns all spins in the triangular plane. And when the magnetic field is applied perpendicular to the easy-plane, the system will firstly evolve into an umbrella phase (Figure 1.3(e)), then followed by a high field coplanar phase (Figure 1.3(d) or (f)) and a fully polarized phase. Furthermore, weak interlayer interaction and easy-plane anisotropy are expected to lead to more possible ordered phases under magnetic field, as we need to take the spin configurations on the adjacent layer into consideration under this condition[40, 41, 42, 43, 44, 45, 46]. The

possible spin ordering states under magnetic fields when we take the interlayer coupling into account are shown in Figure 1.4.

1.2 Triple-perovskite sample $Ba_3CoSb_2O_9$

While searching for the ideal realization of spin 1/2 TLAFs, the triple-perovskite sample BSCO caught our attention. As shown in Figure 1.5(a) and (b), BSCO has a hexagonal lattice structure. Both Co and Sb ions are surrounded by six oxygen ions, forming CoO_6 and SbO_6 octahedra. Co and Sb ions are stacked layer by layer along the c-axis and both of them form triangular lattice in the ab-plane. So the magnetic ions Co^{2+}-layers are separated by two layers of nonmagnetic face-shared SbO_6 octahedra, resulting in a quasi-2D spin sublattice. In the CoO_6 oxygen environment, it is reported that the energy levels of ^4F state of Co^{2+} will be split by the cubic crystal field and spin-orbit coupling (Figure 1.5(c))[47]. And the ground state is a Kramer doublet with $j_{eff} = 1/2$. So we can treat the BCSO as an effective spin 1/2 system at low temperature.

1.2.1 Quantum spin state transitions

The exotic quantum magnetism of BCSO has been well documented. The first aspect is the realization of QSSTs. Under zero field, the spins form a 120-degree ordering state under $T_N = 3.8$ K. All spins lie in the ab-plane because of a weak easy-plane anisotropy. As mentioned in the previous section, theories predicted the quantum spin fluctuations stabilize a novel UUD phase while approaching zero temperature with the applied field parallel to either easy plane or easy axis[39, 48]. The UUD phase exhibits itself as a magnetization plateau within a certain magnetic field regime and with one-third of the saturation moment ($1/3M_s$). Experimentally, the magnetization[49, 50, 51](Figure 1.6), specific heat[52], magnetic torque[52], NMR[44], ESR[50], ultrasonic[53, 54], and neutron diffraction[55, 46], all consistently confirmed the existence of the UUD phase between 9 $\sim$ 15 T with applied field H $\parallel$ ab plane (the easy plane). Detailed studies further reveal a series of QSSTs in BCSO. With increasing field along the ab plane, its 120-degree spin structure at zero field is followed by a canted 120-degree spin structure, the UUD phase, a coplanar

phase (the V phase), and another coplanar phase (the V' phase) before entering the fully polarized state [40, 41, 42, 43, 44, 45, 46]. While for H ∥ c-axis, the 120-degree spin structure will be followed by an umbrella spin structure, and the V phase.

1.2.2 Spin dynamics

The second interesting part of BSCO is its exotic features in spin dynamics measurements. Many experimental [55, 56, 38, 57, 58] and theoretical studies [59, 60, 61] have been performed on this topic. Y. Kamiya et al.[55] reported the spin excitation spectrum in the UUD phase with magnetic field μ_0H = 10.5 T applied in ab-plane (Figure 1.7). The in-plane dispersion in Figure 1.7(a) includes a gapless branch at **q** = (1/3, 1/3, -1) Figure 1.7 (c)), and two gapped modes centered around 1.6 and 2.7 meV. The dispersions along the c-direction are nearly flat(Figure 1.7 (b) and (c)). And compared with the calculated dispersion shown in Figure 1.7 (d), (e), and (f), the spin excitation spectrum can be well captured by a spin wave theory (SWT) + 1/S treatment for a spin Hamiltonian including easy-plane anisotropy and interlayer couplings. However, the zero-field dispersions observed from inelastic neutron scattering measurements haven't been quantitatively described by the calculation. For example, the excitation spectrum reported by David Macdougal et al.[56] is shown in Figure 1.8 (a). Two sharp, well-defined magnon branches are clearly resolved: one gapless and linearly dispersing at low energies, and the other one gapped ($E_{gap} \sim 0.7meV$) at the magnetic Bragg position. These modes correspond to the gapless Goldstone mode associated with rotation of the spins in the ab plane and an out-of-plane mode that is gapped in the presence of easy-plane (exchange) anisotropy, respectively. Meanwhile, there is considerable inelastic signal above the sharp magnon dispersions in the form of a highly structured continuum. David Macdougal et al.[56] pointed out, as shown in Figure 1.8(b), the measured dispersion is heavily downward renormalized compared to the linear spin wave theory (LSWT) dispersion. Such renormalization may be resulted from the transfer of spectral weight from the one-magnon modes to the higher-energy continuum scattering. Furthermore, even taking the two-magnon continuum into consideration, the large scattering weight in the experimentally observed continuum can't be captured. So the explanation of the spectrum of BCSO is still incomplete.

1.2.3 Other compounds in the triple-perovskite family

The triple perovskite structure for BCSO is very flexible in its chemical composition. For example, We can replace Sb^{5+} ions with Nb^{5+} or Ta^{5+} ions[62, 63, 64] while keeping the Co-triangular lattice. It was reported that such replacement drastically changed their properties. $Ba_3CoNb_2O_9$[62] exhibits a two-step ordering process at 1.36 K and 1.10 K with an easy-axis anisotropy and also exhibits the QSSTs. Meanwhile, $Ba_3CoNb_2O_9$ shows clearly ferroelectricity which is not observed in BCSO. Unfortunately, so far, no single crystalline form of $Ba_3CoNb_2O_9$ has been prepared, which limits its studies. On the other hand, neither QSSTs nor ferroelectricity was observed in $Ba_3CoTa_2O_9$. One can also replace Ba^{2+} ions with Sr^{2+} or Ca^{2+} ions[65, 66]. Such replacement will cause lattice distortion, leading to an isosceles triangular Co lattice. The study on the influence of this distortion is still limited. The flexibility on the chemical composition greatly broadens the research on the triple perovskite systems, leading to the studies that I will describe in chapters 4 and 5.

In this dissertation, I will introduce the work we have done on four Co^{2+} based effective spin 1/2 TLAFs. The rest of this dissertation is organized as follows. In Chapter 2, I will briefly introduce the experiment methods we used for the dissertation. In Chapter 3, I will start with the work performed on BCSO. Completed magnetic phase diagrams for H $\parallel$ a and c-axis and angular dependence at 0.32 T were constructed for BCSO. In Chapter 4, Sr-doped BSCO is reported to study the effect of non-magnetic site disorder in this system. Then in Chapter 5, $Ca_3CoNb_2O_9$(CCNO) was studied to reveal how the distortion of triangular lattice can affect magnetism. At last, a new TLAF compound $Na_2BaCo(PO_4)_2$(NBCPO) is studied. NBCPO has attracted lots of attention as a QSL candidate and a rare example of TLAF with easy-axis anisotropy of which high quality single crystal can be obtained. I will report the possible itinerant excitations and QSSTs in this compound.

Chapter 2

Experimental methods

2.1 Sample synthesis

In this part, I will generally introduce the methods that I used to prepare the samples studied in this dissertation. The detailed process of sample preparation can be found in the following chapters.

2.1.1 Solid state reaction method

The solid state reaction method was used to synthesize polycrystalline samples. In this method, stoichiometric amounts of starting materials are mixed with pestle and mortar and compressed into pallets. Then the pallets are annealed in the furnace in specific atmospheres.

2.1.2 Flux method

The flux method was used to obtain single crystal samples. In this method, the components of the desired substance are dissolved in a solvent (flux)[67]. And the solvent is cooled down slowly to let the substance precipitate and form single crystalline samples. It takes place in a crucible made of highly stable, non-reactive material. We usually use Al_2O_3 and Pt crucible for flux growth.

2.1.3 Floating zone method

The floating zone method was performed by an IR-heated image furnace (as shown in Fig 2.1) to synthesize single crystal samples. The polycrystalline samples were compressed as two rods, named as feed and seed rod. These two rods are attached on the upper and lower shaft, respectively. The light of the two halogen lamps is focused by two mirrors, resulting in a high-temperature zone. One end of the feed rod is moved in the high-temperature zone and melted. Then the seed rod is connected to the melted part. The upper and lower shaft are moved down together so that the melted sample solidifies on the seed rod and forms single crystals. The upper and lower shaft usually rotate in opposite directions to make a uniform liquid zone.

2.2 X-ray diffraction and Laue measurement

As a powerful tool to study the lattice structure, X-ray powder diffraction (XRD) measurements are performed on all the reported compounds to check their phase purity and obtain lattice information. The measurements using a HUBER imaging-plate Guinier camera 670 with Cu Kα radiation ($\lambda = 1.5418$ Å) were conducted at room temperature between $4° \leq 2\theta \leq 100°$. The XRD patterns were refined with the Rietveld method using the conventional refinement program FullProf. The background type was selected to be linear interpolation between a set of back ground point with refinable heights. Peak shape was fitted by the pseudo-Voigt function convoluted with an axial divergence asymmetry function.

The single crystal x-ray diffraction measurements were conducted on $Ba_{2.87}Sr_{0.13}CoSb_2O_9$ to determine the exact doping ratio and check the existence of phase separation. The measurements were performed on a Bruker D8 Quest Eco diffractometer with Mo radiation ($\lambda K_\alpha = 0.71073$ Å), which is equipped with Photon II detector. The crystal structure, especially the atomic mixture and disorders, was refined using SHELXTL package with full matrix least-squares on F^2 model[68].

The single crystal samples were oriented and aligned with the Laue back diffraction technique. The Laue patterns were analyzed by the program Orientex to allow the magnetic

field to be applied in the ab-plane or along the c-axis of the samples in all the bulk measurements introduced later.

2.3 Specific heat

The specific heat measurements were performed to observe phase transitions between different spin states. The specific heat ($C_p(T)$) as a function of temperature in different temperature ranges are measured on commercial physical property measurement system (PPMS, Quantum Design) equipped with a He3-He4 dilution refrigerator insert (0.05 K $\leq T \leq$ 5 K) and He3 insert ($0.3K \leq T \leq 9K$), respectively. The high temperature $C_p(T)$ measurements ($2K \leq T \leq 10K$) were also performed by PPMS. The specific heat measurements C_p(H, T, ϕ) as a function of temperature, magnetic field, and field orientation between 0.3 K and 6 K in fields between 0 and 35 T using custom-built single-axis rotation micro-calorimeters [69, 70] cross-calibrated in magnetic field to correct for magnetoresistance of the thermometers [71].

2.4 DC susceptibility and magnetization

The DC magnetic susceptibility (χ_{DC}) measurements under magnetic fields up to 6.5 T were performed with a Magnetic Properties Measurement System (MPMS) with a superconducting interference device (SQUID) magnetometer. χ_{DC} measurements under magnetic fields up to 14 T were conducted using a vibrating sample magnetometer (VSM) option in a PPMS. The Weiss temperature (θ_w) was obtained by Curie-Weiss (CW) fit of the inversed susceptibility. The isothermal magnetization up to 35 T was measured with a VSM at the National High Magnetic Field Laboratory (NHMFL), Tallahassee. Another magnetization measurement up to 40 T using compensated induction coil with sample-in/sample-out background subtraction was performed at the NHMFL, Los Alamos.

2.5 AC susceptibility

The ac susceptibility measurements are also used to characterize the magnetic properties of all compounds in this dissertation, especially the successive phase transitions under the magnetic field. The AC susceptibility measurements can reveal weak features in magnetization because they represent the derivative of M(H) (dM/dH). So AC susceptibility measurements are sensitive to the field induced phase transitions.

AC susceptibility measurements were performed at SCM1 and SCM2 of NHMFL with the conventional mutual inductance technique with the ac coils and sample immersed in He3 liquid (SCM2) or in a mixing chamber of a dilution fridge (SCM1). The 18 T superconducting magnet was used to apply DC magnetic field. The voltage controlled current source (Stanford Research, CS580) was used to generate ac excitation field. The frequency of the ac excitation field range from 81 to 2147 Hz. The signal was read by lock-in amplifiers (Stanford Research, SR830). The phases of the lock-in amplifiers are set to read the linear component (first harmonic response) and the nonlinear components (second and third harmonic responses) with respect to the oscillating ac field frequency.

2.6 Dielectric constant and polarization

The dielectric constant and polarization measurements were conducted on CCNO, and for comparison, on $Ca_3NiNb_2O_9$(CNNO), as shown in chapter 5. Samples were polished to have a parallel capacitor geometry with typical dimensions of 4.7 $mm^2\times$ 0.4 mm. Silver epoxy was painted on the two opposite parallel surfaces for the electrical contacts. A commercial capacitance bridge (Andeen-Hagerling, AH-2700A model) was used to measure the dielectric constant. The external magnetic and electric fields were applied parallel to the a and c* axis of the monoclinic system. The polarization measurements were performed on the same set of samples prepared for the dielectric constant measurements. The pyroelectric current was recorded while the temperature was rapidly increased $\sim$ 10 K/min under various magnetic fields. To calculate the polarization, the pyroelectric currents were integrated in the time domain. The electric fields along the a-axis and c*-axis were 700 kV/m and 590

kV/m, respectively, while cooling down the samples to form monodomains that give rise to maximized the pyroelectric current signal.

2.7 Thermal conductivity

Temperature dependence of thermal conductivity $\kappa(T)$ were measured on NBCPO to check the existence of quantum spin liquid state in this compound since the non-zero residual thermal conductivity κ_0/T in the zero-temperature limit has been widely accepted as evidence of spinon[19, 20, 21, 22]. Meanwhile, both field and temperature dependence of thermal conductivity (κ(H) and $\kappa(T)$) measurements were conducted on BCSO and NBCPO to probe the successive phase transitions under magnetic field.

Thermal conductivity (κ) was measured by using a "one heater, two thermometers" technique in a He3-He4 dilution refrigerator and in a He3 refrigerator, equipped with a 14 T superconducting magnet[72, 73, 74, 75, 76, 77, 78, 79, 80, 81, 82]. The sample was cut precisely along the crystallographic axes, where the longest and the shortest dimensions are along the a and the c axes, respectively. The heat currents were applied along the a axis while the magnetic fields were applied along either the a or c axis.

For low-temperature thermal conductivity measurements, calibrating the magnetoresistance effect of resistor thermometers is a basic requirement. The thermometers (RuO_2) used at 300 mK to 30 K in the He3 refrigerator are precalibrated by using a capacitance sensor (Lakeshore Cryotronics) as the reference[74, 76, 77, 78]; the thermometers (RuO_2) used at 50 mK to 1 K in the dilution refrigerator are precalibrated by using a RuO_2 reference sensor (Lakeshore Cryotronics) mounted at the mixture chamber (the superconducting magnet was equipped with a cancellation coil at the height of mixture chamber)[79, 80, 81]. The resolution of the κ measurements is typically better than 3% (better at a higher temperature). The sample size was determined by using microscopy and has an uncertainty of $< 5\%$. Therefore, the total error bar of is κ always $< 8\%$. The uncertainty of κ_0/T caused by the fitting is $\sim 2\%$.

2.8 Neutron scattering

2.8.1 Powder neutron diffraction

High-resolution neutron powder diffraction measurements were performed on CCNO by a neutron powder diffractometer, HB2A, at the High flux Isotope Reactor (HFIR) of Oak Ridge National Laboratory (ORNL). Around 3 g of powder sample were loaded in an Al-cylinder can and mounted in a closed-cycle refrigerator. The neutron wavelength is $\lambda = 1.5424$ Å with a collimation of 120-open-60. .

2.8.2 Single crystal neutron diffraction

Single crystal neutron diffraction measurements on CCNO were performed by the Fixed-Incident-Energy Triple-Axis Spectrometer (HB-1A) at HFIR, ORNL. At HB-1A, the diffraction data were collected at 0.3 K and 5 K with the wavelength $\lambda = 2.36$ Å . From the magnetic wavevector of ($n_1 \pm 1/3$, $n_2 \pm 1/3$, $n_3 \pm 1/3$), 20 magnetic Bragg peaks had been measured.

Single crystal neutron diffraction measurements on BCSO were made using a ^{3}He insert at the Cold Neutron Triple-Axis Spectrometer CG-4C at HFIR, with the crystal aligned on the [HHL] scattering plane and in a vertically directed magnetic field. The neutron wavelength is $\lambda = 4.1282$ Å .

Single crystal neutron diffraction measurements of $Ba_2.87Sr_0.13CoSb_2O_9$ were performed at HFIR, ORNL. The zero field measurements were carried out at 300 mK with the wavelength of $\lambda = 1.5424$ Å in the Oxford cryogen-free HelioxVT refrigerator at the single crystal diffractometer DEMAND[83], HB-3A and at 1.5 K with the wavelength of $\lambda = 4.2636$ Å in the orange cryostat on the CG-4C. The measurements under magnetic field were conducted at 1.5 K with the wavelength of $\lambda = 2.3779$ Å in an 8T Vertical Asymmetric Field Cryomagnet on the HB-1A.

All the diffraction data were analyzed by the Rietveld refinement with the program FullProf[84]. The magnetic structure compatible with the lattice symmetry was obtained by SARAH software.

2.8.3 Inelastic Neutron scattering

The INS measurements under zero field for $Ba_2.87Sr_0.13CoSb_2O_9$ were performed at 300 mK on the Disk Chopper Spectrometer (DCS) with the He-3 Dipper insert in the NIST Center for Neutron Research (NCNR). The INS measurements under applied magnetic field were conducted at 1.6 K in an 11 T magnet on the Multi Axis Crystal Spectrometer (MACS) in NCNR[85].

Chapter 3

$Ba_3CoSb_2O_9$

3.1 Motivation

Up to now, despite all the extensive studies on BCSO, a completed magnetic phase diagram for either H ∥ ab-plane or H ∥ c-axis is still not available. Most of the reported phase diagrams mainly focus on the UUD phase. The open questions include (i) for H ∥ ab-plane, what is the exact phase boundary for the V-V' phase transition? Is there any possibility of the existence of new magnetic phases beyond the theoretical prediction? (ii) for H ∥ c-axis, the NMR results suggested two more possible spin state transitions around 22 T and 29 T[44], which however have not been confirmed by further experimental studies; (iii) while there is a theoretically predicted angle-dependent magnetic phase diagram, the absence of experimental measurements as a function of magnetic-field orientation has left other predictions of these models untested. How the spin state transitions evolve from ab-plane to c-axis is still elusive. This Chapter includes the results of specific heat, magnetic torque, thermal conductivity, and neutron scattering measurements on BCSO. Based on these results, we mapped out the completed magnetic phase diagrams of BCSO as functions of magnetic field, temperature and the direction of field to answer these questions.

3.2 Sample preparation

The polycrystalline samples of BCSO are prepared by solid state reaction method. The starting materials $BaCO_3$, $CoCO_3$ and Sb_2O_3 were mixed together and annealed in air at 1300 °C for 20 hours. The single crystal samples of BCSO are grown by traveling-solvent floating-zone technique. The growth was carried out in 90% Ar and 10% O_2. The feed and seed rod rotated in opposite directions at 25 rpm. And the crystal grew at a rate of 30 mm/h.

3.3 Results

Figure 3.1 summarizes the results for H ∥ a-axis. The C_p at 0.52 K (Figure 3.1(a)) exhibits four obvious peaks at $H_{a1} \sim 6$ T, $H_{a2} \sim 10$ T, $H_{a3} \sim 15$ T, and $H_{a5} \sim 32$ T, respectively, and a broad hump around $H_{a4} \sim 24$ T. With increasing temperatures, (i) the H_{a1} peak quickly disappears with $T \geq 1$ K; (ii) H_{a2} barely changes; (iii) the H_{a3} peak becomes weaker and shifts to higher fields; (iv) the H_{a4} hump gradually changes to a peak and shifts to lower fields; (v) the H_{a5} peak shifts to lower field; and (vi) at 3.63 K, the H_{a3}, H_{a4}, H_{a5} peaks merge into one peak. The derivative of τ measured at 0.32 K (Figure 3.1(b)) exhibits four anomalies, which positions agree well with the H_{a2}, H_{a3}, H_{a4} and H_{a5} obtained from the C_p measurement.

The field dependence of κ at 0.36 K (Figure 3.1(c)) clearly shows a double peak feature. The first peak is between $H_{a1} \sim 6$ T and $H_{a2} \sim 10$ T (or H_{a1} and H_{a2} are two positions for the minimums) and the second peak starts at H_{a2}. Since the highest field for the κ measurement is 14 T, the upper critical field of the second peak can't be seen here. With increasing temperatures, the fist peak becomes weaker and disappears with $T \geq 0.97$ K and the second peak becomes broader and shifts to lower fields. The reported κ data measured at 2.8 K also show a similar peak[86] (the second peak here). Figure 3.1(d) shows the temperature dependence of κ measured in several fields. The zero field data clearly shows a minimum around $T_N \sim 3.6$ K, where the long-range magnetic ordering occurs. For the 14 T data,

a slope change occurs around 5 K. For the 8.5 T data, three slope changes are observed, indicating transition temperatures at 4.4 K, 2.6 K, and 1 K.

Figure 3.1(e) shows the field dependence of the [1/3, 1/3, 0] and [1/3, 1/3, 2], two magnetic Bragg peaks' intensity measured at 0.32 K, which suddenly appears above 3 T and 4.6 T, respectively. Thereafter, the intensity for both peaks increases with increasing field and shows a slope change around H_{a1}. The temperature dependence of the intensity for these two peaks and another magnetic Bragg peak [1/3, 1/3, 1] measured at 8 T all consistently shows a fast increase below $T_N \sim 4.3$ K, a constant regime between 2.5 K and 1 K, and a slow decrease below 1 K.

Figure 3.2 summarizes the results for H $\parallel$ c-axis. The C_p at 0.35 K (Figure 3.2(a)) exhibits four anomalies at $H_{c1} \sim 12.5$ T, $H_{c2} \sim 21$ T , $H_{c3} \sim 29$ T, and $H_{c4} \sim 33$ T. With increasing temperatures, (i) the H_{c1} slightly shifts to lower fields; (ii) the H_{c3} anomaly becomes stronger and shifts to lower fields; and (iii) the H_{c4} peak becomes weaker and shifts to lower fields. The derivative of τ measured at 0.32 K (Figure 3.2(b)) exhibits three anomalies, which positions agree well with the H_{c1}, H_{c2} and H_{c4} obtained from the C_p measurement. The field dependence of κ measured between 0.36 K and 3 K (Figure 3.2(c)) clearly shows an anomaly at $H_{c1} \sim 12.5$ T. Figure 3.2(d) shows the temperature dependence of κ measured in several fields. The zero field data and 14 T data clearly show a slope change at 3.4 K and 4 K, respectively, which represents the magnetic ordering temperatures. For the 12 T data, two slope changes at 4 K and 3.2 K are observed.

Figure 3.3 summarizes the angle dependent data measured at 0.32 K. While H rotates from the a-axis (90°) to c-axis (0°), the C_p data (Figure 3.3(a)) shows that (i) the peak at H_{a1} disappears within 47° from the c-axis; (ii) H_{a2} increases and evolves into H_{c1}; (iii) H_{a3} increases and H_{a4} doesn't change too much and they show the tendency to merge; (iv) the anomaly at H_{c3} begins to appear within 53° from the c-axis. The evolution of the critical fields also can be observed from the τ measured at different angles (Figure 3.3(b) and its derivative (Figure 3.3(c) and (d)). One noteworthy observation is that the feature at H_{c2} for $d\tau/dH$ only exists while H is near c-axis.

3.4 Phases diagrams and discussion

By using the critical fields and ordering temperatures presented above, three magnetic phase diagrams were constructed in Figure 3.4.

3.4.1 H ∥ a

In the phase diagram with H ∥ a-axis (Figure 3.4(a)), several new features are observed by comparing to the reported phase diagrams.

First, a new phase boundary (between phase I_a and phase II_a) was observed around 6 T with temperature below 1 K. While the peak at H_{a1} for C_p and the double peak feature for κ strongly support the existence of this phase boundary, no new magnetic Bragg peaks were observed in phase II_a by comparing to those observed for phase I_a (the phase between 3 T and 10 T and with temperature below T_N). The spin structure for phase I_a and II_a seems to be similar. One subtle change is that with decreasing temperatures the intensity of [1/3, 1/3, 2], [1/3, 1/3, 0] and [1/3, 1/3, 1] peaks decreases after entering phase II_a while keeps a constant value in phase I_a. This change suggests that below 1 K, the ordered moment, not only the moment along the H direction but also the moment of the other two pair spins, becomes smaller. One possible reason for this could be that below 1 K, the strong QSFs begin to suppress the ordered moment. Actually, an early study predicted a possible magnetic-field induced phase transition between two Y phases with differing interplanar coupling below UUD (III_a) phase[40], but the expected temperature dependence of the phase transition is inconsistent with our experimental result. So the determination of the exact nature and the true microscopic spin ordering of this low field phase need future studies.

Second, the phase boundary between the IV_a and V_a phases was clearly resolved. The broad feature shown in specific heat and torque measurement indicates the second order nature of this transition, which agrees with earlier experimental results from magnetization [50], NMR [44], and neutron diffraction measurements [46]. However, it is contrary to a first order phase transition predicted by calculation at this field[40, 44, 45]. And the neutron scattering measurements suggest either a first-order transition from the distorted V spin state (Figure 1.4(g)) to a V' (Figure 1.4(h)) or a second-order transition to the Ψ (fan) spin structure

(Figure 1.4(j))[46]. So here we tentatively assign phase IV_a and V_a to be the distorted V and the Ψ phase, respectively.

Third, a tetracritical point connecting the paramagnetic, UUD, IV_a and V_a phases could be found at (3.8 K, 17 T). The splitting of the low and high field phases for H $\parallel$ a-axis and the existence of at least one tetracritical point indicate that there is an antiferromagnetic coupling of magnetically ordered spins between the *ab* planes. So that the spins can alternate orientations within the planes from one to another at low fields, and, co-align with each other at higher fields. Moreover, it is actually pretty rare to observe tetracritical point in magnetic materials. To our knowledge, the other examples exhibiting the tetracritical point only include $K_2Mn_{0.978}Fe_{0.022}F_4$[87], $GdAlO_3$[88], and $CsMnBr_3$[89].

3.4.2 H $\parallel$ c

The phase diagram with H $\parallel$ c-axis is shown in Figure 3.4(b). Phase I_c below 12 T was identified as the classically expected umbrella spin structure (Figure 1.4(k)). At higher magnetic field, two new features were observed, including (i) the C_p and τ data supported the appearance of a phase transition around 22 T at 0.32 K. The magnetization calculated from a semiclassical energy density modeling has demonstrated that the phase transition near to $\sim 3/5M_s$ (the transition from II_c to III_c phase) for H $\parallel$ a-axis also exists for H $\parallel$ c-axis but becomes less evident. Theoretically, a first order transition from the umbrella phase to the distorted V phase is predicted at H_{c1}, which is consistent with the sharp features we observed in the C_p and τ measurement[44]. So we assign II_c phase to be the distorted V phase. However, the broad features at H_{c2} are inconsistent with the first order transition from the distorted V phase to the staggered V phase (Figure 1.4(g)) predicted by theory at this field[44]. So more research is required to solve the exact spin structure of phase III_c. (ii) A phase boundary around 30 T, just below the saturation field, was resolved. The exact spin structure for this new phase (phase IV_c) between 30 T and the saturation field (around 33 T) has not been established. On the other hand, one theoretical work from Starykh *etal*[61]. proposed that a two dimensional Heisenberg TLA with spin-1/2, such as BCSO, can possess a rich phase diagram near saturation in a field due to competition between the classical and quantum order. One proposed scenario is that between the commensurate coplanar and fully

polarized state, two intermediate phases can exist, one with coplanar incommensurate spin order and the other one with noncoplanar double-Q spiral order. It will be interesting to investigate whether phase IV_c belongs to one of them in the future.

3.4.3 From H ∥ a to H ∥ c

The observed angle-dependent phase diagram at 0.32 K was compared to the one calculated by using semiclassical energy density modeling[44]. The most profound differences are of course the new phase transitions around 6 T with H ∥ a and 29 T with H ∥ c in our diagram. Except the new phase boundaries, the observed phase diagram agrees well with the calculated one under low fields. In both diagrams, the Y phase with H ∥ a continuously evolves into the umbrella phase with H ∥ c. Similarly, the UUD phase continuously evolves into the distorted V phase.

At higher field, the predicted critical fields for the phase boundaries are also in good agreement with our measurements shown at high angles (H is close to a-axis). However, a significant difference between theory and experiment is found at lower angles: two-layer model calculations of interlayer coupling predict that, with the field rotating from a-axis to c-axis, the phase boundaries of the 'upper-intermediate-field' (UIF) phase will get close to each other and merge around 18°. And the merged phase boundary evolves into the boundary between phase II_c and phase III_c. As a result, there predicted to be a field-rotation-induced phase transition round 18° and the UIF should terminate there. However, the results of our measurement indicate the UIF phase still exists until H rotates to c-axis. And the upper phase boundary of the UIF phase is likely to evolve into the new phase transition we observed around 30 T.

3.5 Summary

In summary, by performing low temperature and high field measurements on specific heat, thermal conductivity, magnetic torque, and neutron diffraction, completed magnetic phase diagrams for H ∥ a and c-axis and angular dependence at 0.32 T were constructed for BCSO. While the general features of the phase diagrams with all phase boundaries clearly resolved

are consistent with the theoretical proposals, several newly observed features including new phase boundaries appearing below 1 K and around 6 T for H ∥ a-axis and around 30 T for H ∥ c-axis are not expected. The experimental angle- dependent phase diagram also deviates from the theoretically predicted one on several aspects. All these new findings challenge the existing theories on spin-1/2 TLAF with XXZ anisotropy and call for further studies.

Chapter 4

$Ba_{2.87}Sr_{0.13}CoSb_2O_9$

4.1 Motivation

Recently, much attention has been paid to the disorder effects in the TLAFs, since materials inevitably have defects and/or random disorder. Compared to the disorder on magnetic ion sites which usually destroys the magnetic interactions and leads to glassy or paramagnetic states, the disorder on non-magnetic ion sites remains more intriguing and illusive. How such kind of disorder affects the magnetism on the chemically ordered magnetic sublattice is a challenging question with limited knowledge so far.

A good example of non-magnetic ion site disorder is the YMGO introduced in previous chapter. In YMGO, the Yb^{3+} ions with effective spin-1/2 form a geometrically frustrated triangular layer[25, 90], between these layers the site mixture of Mg^{2+}/Ga^{3+} ions cause the intrinsic disorder of the non-magnetic ion sites. Such disorder actually contributes to the controversial magnetic ground state of YMGO since the glassy ground state in YMGO suggested by the thermal conductivity[28] and the frequency dependent AC susceptibility[29] measurement could be due to this site disorder[90, 91]. Several theoretical models which include this site disorder effect have been proposed for YMGO: highly anisotropic nearest-neighbor interactions[92], the random singlet (RS) state[93, 94], randomness-induced QSL state[95], the mimicry of a spin liquid[96, 97], and randomness induced spin-liquid-like phase

in J_1-J_2 model[98, 99, 100, 101, 102, 103, 104]. Of these, the RS state and randomness-induced QSL have also been applied to other quantum magnets with disorder[105, 106, 107, 108, 109, 110, 111, 112, 113, 114, 115, 116, 117, 118, 119, 120, 121, 122, 123].

The controversial magnetic ground state of YMGO reflects of the complex role that the disorder on the non-magnetic ion sites plays in quantum magnets. To better understand this role, more studies on quantum magnets with such kind of disorder is highly desirable. Just as described before, BCSO is a rare example of an equilateral TLAF with effective spin-1/2 (for Co^{2+} ions) and easy-plane anisotropy. The exotic quantum magnetism and flexibility in chemical composition make BCSO an ideal system to incorporate the non-magnetic ion site disorder and thereafter study its effects on quantum magnetism. In this paper, we successfully grew single crystals of $Ba_{2.87}Sr_{0.13}CoSb_2O_9$ to introduce the disorder (the mixture of Ba/Sr ions) on the non-magnetic Ba^{2+} ion sites and studied its magnetic properties by performing DC and AC susceptibility, specific heat(C_p), elastic and inelastic neutron scattering measurements. By comparing the obtained results to those of the parent compound BCSO, we learned that such disorder on the non-magnetic ion sites significantly tunes the magnetic ground state, phase diagram, and spin dynamics of this spin-1/2 equilateral TLAF.

4.2 Sample preparation

Polycrystalline Sr-doped $Ba_3CoSb_2O_9$ (Sr-BCSO) are prepared by solid state reaction method. The starting materials $BaCO_3$, $SrCO_3$, $CoCO_3$ and Sb_2O_3 were mixed together and annealed in air at 1300 °C for 20 hours. The single crystal samples of Sr-BCSO are grown by traveling-solvent floating-zone technique. The growth was carried out in 90% Ar and 10% O_2. The feed and seed rod rotated in opposite directions at 25 rpm. And the crystal grew at a rate of 30 mm/h.

4.3 Crystal and magnetic structure

The refinement of the single crystal x-ray data confirms that the composition for the as-grown crystal is $Ba_{2.87}Sr_{0.13}CoSb_2O_9$. It ha hexagonal structure with the space group $P6_3/mmc$ and lattice parameters a =5.847(3) Å and c = 14.507(6) Å. The detailed refinement and crystallographic information is listed in table 4.1 and 4.2. The results show $\sim 4\%$ Sr mixed on Ba site. Moreover, no atomic vacancies were observed on Co, Sb and O sites. As shown in Figure 4.1(a), in this structure, each Co^{2+} ion is surrounded by six O^{2-} ions, forming a CoO_6 octahedron. The layers of the triangular lattice of CoO_6 octahedra in the ab plane are separated by two face-shared SbO_6 octahedra. The intralayer and interlayer distances between the Co^{2+} ions are 5.847(3) Å and 7.253(5) Å, respectively, which results in a quasi-2D triangular lattice system.

Elastic neutron scattering measurements under zero and varying applied magnetic fields were performed to probe the magnetic structure of Sr-BCSO. As shown in Figure 4.2(a), the temperature dependence of the intensity for a magnetic peak [1/3 1/3 1] measured at zero field shows a rapid increase below T_{N1} = 2.8 K, which indicates a magnetic ordering. Moreover, a set of magnetic peaks indexed by propagation vector [1/3 1/3 1] were collected in a single crystal neutron scattering measurement. As shown in Figure 4.2(b), the data can be fitted by a 120-degree spin structure in the ab plane. The refined magnetic moment is 1.24(7) μ_B/Co. Meanwhile, a weak intensity at zero field for the magnetic peak [1/3 1/3 0] below T_{N1} was also observed, as shown in Figure 4.2(a). The existence of vector [1/3 1/3 0] suggests that spins in the ab plane should have a weak ferromagnetic moment. One possible scenario is the canted 120-degree spin structure, in which the sum of the magnetic moments of the three sublattice spins is nonzero but lead to a resultant magnetic moment, as shown in Figure 4.1(b). Unfortunately, the exact spin structure can't be solved due to the limited data resolution we obtained. Therefore, while the data suggests a canted spin structure as the ground state for Sr-BCSO, we still use the 120-degree spin structure to obtain the ordered moment.

The field dependence of the intensities for the [1/3 1/3 1] and [1/3 1/3 2] peaks measured at 1.5 K are shown in Figure 4.3(a) and (b), respectively. For the [1/3 1/3 1] peak, its intensity

is basically a constant from 0 T to 6 T, and then shows a drastic drop around $\mu_0 H_{a1} = 6$ T. For the [1/3 1/3 2] peak, its intensity increases with increasing field but with a slope change around 6 T. These features suggest there is a spin state transition around H_{a1}.

4.4 DC and AC magnetic susceptibility

The temperature dependence of the DC magnetic susceptibility, $\chi(T)$, under magnetic fields is shown in Figure 4.4. As H ∥ ab-plane is increased (Figure 4.4(a-c)), $\chi(T)$ shows several features. (i) A broad peak appears around 6 K with $\mu_0 H < 5$ T; (ii) A peak appears around 3 K at $\mu_0 H = 5$ T, which is labeled as T_{N1} and shifts to lower temperatures with increasing field; (iii) In addition to the peak at T_{N1}, at $\mu_0 H = 7$ T the data shows that $\chi(T)$ increases rapidly below 5 K. Here we use the peak position of its second-order derivative (Figure 4.4(c)) to represent this feature, labeled as T_{N2}. With increasing field, T_{N2} shifts to higher temperatures between 7 T $\leq \mu_0 H \leq$ 11 T; (iv) with $\mu_0 H \geq 12$ T, the feature at T_{N2} involves to be a peak again (Figure 4.4(b)).

For H ∥ c-axis, the peak at T_{N1} is not as strong as that for H ∥ ab-plane and appears when $\mu_0 H \geq 7$ T (Figure 4.4(d)). The feature at T_{N2} also appears when $\mu_0 H > 11$ T (Figure 4.4(e, f)). Compared to the H ∥ ab-plane case, for the H ∥ c-axis, both features appear at a higher magnetic field.

As shown in Figure 4.5, the DC magnetization, M(H), measured at 1.5 K by using a VSM shows a weak plateau feature for H ∥ ab-plane while only a slope change for H ∥ c-axis. Accordingly, the derivative dM/dH for H ∥ ab-plane shows a peak-valley-peak feature with two critical fields $\mu_0 H_{a1} = 7.5$ T and $\mu_0 H_{a2} = 16.4$ T. Meanwhile, the derivative for H ∥ c-axis only shows one peak at $\mu_0 H_{c1} = 8.7$ T. The saturation field is around 33 T for both directions. The saturation moments are 1.8 μ_B/Co and 1.9 μ_B/Co for H ∥ ab-plane and H ∥ c-axis, respectively. For H ∥ ab-plane, the DC magnetization was also measured at 0.7 K by using a compensated induction coil with sample-in/sample-out background subtraction (not shown here), which shows similar behavior to the 1.5 K data.

Since the field dependent AC magnetic susceptibility, $\chi'(H)$, is basically equivalent to dM/dH, we measured $\chi'(H)$ at 50 mK to double check the critical fields. As shown in Figure 4.6, two

critical fields at $\mu_0 H_{a1} = 8.1$ T and $\mu_0 H_{a2} = 16.0$ T for H ∥ ab-plane and one at $\mu_0 H_{c1} = 9.8$ T for H ∥ c-axis were observed. This is consistent with the DC M(H) results. Since the χ'(H) signal is on top of the coil background, it appears less pronounced than dM/dH in Figure 4.5.

4.5 Specific heat

Figure 4.7 shows the temperature dependence of the specific heat, C_p, measured at different fields. At zero field, C_p shows two sharp peaks at $T_{N1} = 2.7$ K and $T_{N2} = 3.3$ K, respectively, which indicates a two-step magnetic ordering. The T_{N1} value is consistent with the ones determined by the neutron diffraction and $\chi(T)$ data. With increasing field H ∥ ab-plane, these two peaks at T_{N1} and T_{N2} become less pronounced while their positions remain almost unchanged. The peak at T_{N1} disappears around 6.5 T while the peak at T_{N2} disappears around 8 T. At around 7 T, another broad peak start to appear, labeled as T_{N3} (Figure 4.7(a)). This peak becomes stronger and shifts to higher temperatures with increasing field. For H ∥ c-axis (Figure 4.7(b)), the peak at T_{N1} becomes weaker with increasing field and is unrecognizable around 8 T. Meanwhile, the peak at T_{N2} doesn't change obviously. Apparently, the evolution of C_p under field is quite different between the H ∥ ab-plane and H ∥ c-axis cases.

4.6 Magnetic phase diagrams

Magnetic phase diagrams for H ∥ ab-plane and H ∥ c-axis were constructed by using the critical temperatures and fields obtained above, as shown in Figure 4.8. Besides the high temperature paramagnetic phase and high field fully polarized phase, the H ∥ ab-plane phase diagram includes three phases while the H ∥ c-axis one has two phases.

4.7 Inelastic neutron scattering spectra

The INS spectra of Sr-BCSO were measured at zero field and 9 T in the *ab* plane, which allows us to study the spin dynamics in phase I and II in Figure 4.8 (a). Figure 4.9(a) and (b) show the INS spectra dispersion up to ~ 2.5 meV along the [H H 1] and [1/3 1/3 L] directions at zero field, respectively. While the intralayer dispersion is sharp and the interlayer dispersion is quite broad, both of them only show one gapped mode. The energy cut at the zone center of [1/3 1/3 1] plotted in Figure 4.10(b) shows no intensity near zero energy but a broad peak around 0.5 meV, which further confirms that there is only one gapped mode with the gap around 0.5 meV for the INS spectra. Another noteworthy feature is that there is no intensity at the M point for the intralayer dispersion. Fig 9 (c) and (d) show the INS spectra up to 5 meV along the two directions, both of them show no obvious intensity at energy above 1.5 meV.

The spectra under 9 T are shown in Figure 4.9(e) and (f) for the two directions, respectively. It is obvious that there are two modes with broad dispersion along the H direction but two flat modes along the L direction. The energy cut at [1/3 1/3 1] plotted in Figure 4.10(c) further confirms that one mode is gapless and the other mode is gapped, with a gap at around 2.5 meV. The more detailed field scan of the cut at [1/3 1/3 1] is shown in Figure 4.10(a). It shows that with increasing field, the gapped mode at zero field splits into two modes, one of which decreases to zero at fields above 6 T while the other mode increases.

4.8 Discussions

To learn the effects of non-magnetic ion site disorder, we compare several aspects of the observed magnetic properties of Sr-BCSO to those of the parent compound BCSO.

(i) *Anisotropy* The anomaly at T_{N1} for $\chi(T)$ measured at low fields such as 5 T and the magnetization plateau feature are only observed for H $\parallel$ ab-plane in Sr-BCSO. Both features are similar to those of BCSO, which indicates that the Sr-BCSO has the same anisotropy, the easy-plane anisotropy, as BCSO.

(ii) *Magnetic ground state* The magnetic ground state for Sr-BCSO is a two-step transition with a weak ferromagnetic moment, or a possible canted 120-degree spin structure, as evidenced by the appearance of the [1/3 1/3 0] and [1/3 1/3 2] magnetic peaks at zero field. This is different from that of BCSO, which is a one step transition with a 120-degree spin structure showing no ferromagnetic moment[52, 51, 38]. In BCSO, the [1/3 1/3 0] and [1/3 1/3 2] magnetic peaks only appear under applied fields. The room temperature single crystal diffraction measurement confirms that Sr-BCSO is isostructural to BCSO with an equilateral Co^{2+} triangular layer. The low temperature single crystal neutron diffraction measurements further show no evidence of structural distortion below the magnetic ordering temperatures for Sr-BCSO. Moreover, as argued in (i), both samples have the same easy-plane anisotropy. Therefore, it is surprising to see that the Sr-doping can lead to such a different magnetic ground state in Sr-BCSO.

One possible scenario is that the Sr doping can cause local structural distortion of the CoO_6 octahedra and therefore introduce a spatial anisotropy into the system. This spatial anisotropy, on top of the easy-plane anisotropy, can lead to a two-step transition with canted spins. For example, $Ba_3NiNb_2O_9$ has an equilateral triangular lattice for spin-1 Ni^{2+} ions and orders at 4.9 K with a 120-degree spin structure in the *ab* plane[65]. By replacing Ba^{2+} ion with Ca^{2+} ion with smaller ionic size, a structural distortion is introduced into the system and therefore $Ca_3NiNb_2O_9$ now has a isosceles triangular lattice for Ni^{2+} ions. One consequence is that $Ca_3NiNb_2O_9$ orders with a two-step transition at 4.2 K and 4.8K[65]. Future studies on the local structure of Sr-BCSO is desirable to exam this possibility and better understand its magnetic ground state.

(iii) *Ordering temperature and ordered moment* The ordering temperature of Sr-BCSO is around 3.3 K, which is 13% reduction of the ordering temperature, 3.8 K, for BCSO. From the structural view, Sr-BCSO should have higher ordering temperature due to its shorter Co-Co intralayer distance since the Sr doping leads to a smaller lattice parameter a, which is 5.847 Å. For BCSO, it is 5.856 Å. Therefore, this lower ordering temperature could be related to the randomization of exchange interactions due to the Ba/Sr mixture. Meanwhile, the ordered moment for Sr-BCSO is around 1.24 μ_B/Co, which is smaller than the 1.5 μ_B/Co of BCSO. For BCSO, we also performed single crystal neutron diffraction measurements and

obtained this ordered moment through refinement by using a 120-degree spin structure (the data is not shown here). In fact, both of these ordered moments are smaller than the saturation moment around $1.8 \sim 2\ \mu_B$/Co. In a spin-1/2 triangular lattice antiferromagnet, the reduced ordered moment could be due to the quantum spin fluctuations. Therefore, the even smaller ordered moment of Sr-BCSO indicates that the Sr-doping enhances such kind of spin fluctuations. This enhancement could be another factor for the reduced ordering temperature.

(iv) *Field induced spin state transitions* For H ∥ ab-plane, it is noted that the magnetization at H_{a1} and H_{a2} for Sr-BCSO is 0.5 μ_B and 1.1 μ_B, respectively, which is around 1/3, and $\sqrt{3}/3$ of the saturation value (1.8 μ_B, Figure 4.5(a)). For BCSO we described in the previous section, with increasing field along the *ab* plane, its 120-degree spin structure at zero field is followed by a canted 120-degree spin structure, the UUD phase, a coplanar 2:1 canted phase (V phase) with one spin in the 120-degree spin structure rotated to be parallel with another spin, which gives $\sqrt{3}/3\ M_s$; and another coplanar phase before entering the fully polarized state[49, 50, 52, 51, 40, 41, 42, 43, 44, 45, 46]. Therefore, here we tend to assign the phases I, II, and III for H ∥ ab-plane of Sr-BCSO as the canted 120-degree spin structure, the UUD phase, and the V phase. It is obvious that the magnetization plateau feature in Sr-BCSO is much weaker than that of BCSO, which could be due to the Sr-doping disorder effect. In another triangular lattice antiferromagnet $Rb_{1-x}K_xFe(MoO_4)_2$, the disorder introduced by the K-doping also weakens the magnetization plateau feature related to the UUD phase[124]. As learned from BCSO, while for H ∥ c-axis, its 120-degree spin structure will be followed by an umbrella spin structure and a several coplanar phases. However, for Sr-BCSO, the magnetic ground state is the canted 120-degree spin structure, which also should be the spin structure for phase I in its H ∥ c-axis phase diagram. Therefore, it is difficult to make the analogy between the H ∥ c-axis phase diagrams for Sr-BCSO and BCSO. The nature of the phase II for Sr-BCSO needs future studies to clarify.

(v) *Spin dynamics* The observed INS spectra of Sr-BCSO have several differences from those of BCSO. (a) At zero field, only one gapped mode for Sr-BCSO but two modes (one gapless mode and one gapped mode with gap around $6 \sim 7$ meV) for BCSO[57, 58, 38, 56]; (b) Under field in the UUD phase, two modes for Sr-BCSO but three modes for BCSO[55]. The

comparison of the energy cut at the [1/3 1/3 1] position (Figure 4.10 (b, c)) further highlights these two differences. It is noticed that the two modes at low energy in the UUD phase for BCSO (the data measured at 11.25 T) may merge into each other in the UUD phase for Sr-BCSO (the data measured 9 T), as shown in Figure 4.10(c); (c) No intensity at M point for Sr-BCSO but a flat mode and a rotonlike minimum at M point for BCSO[57, 58, 38, 56]; (d) No intensity above 1.5 meV for Sr-BCSO but a columnar continuum extending to at least 6 meV for BCSO[57, 58, 38, 56].

For BCSO, the modes at zero field correspond to the gapless Goldstone mode associated with rotation of the spins in the *ab* plane and an out-of-plane mode that is gapped in the presence of an easy-plane anisotropy, respectively. The rotonlike minimum at M point has been related to a magnon decay[38], but is under debate[56]. The origin for the continuum at high energy is not clear so far. As we proposed above, the Sr-doping possibly introduces local spatial anisotropy to account for its two-step magnetic ordering. This spatial anisotropy will break the rotational symmetry of the spins in the *ab* plane. Whether such kind of effect will lead to the disappearance of the gapless mode, or furthermore, the disappearance of the intensity at M point and the continuum, needs future theoretical studies to clarify.

4.9 Summary

In summary, the Sr-doping on the non-magnetic Ba^{2+} ion sites in BCSO affects its magnetic properties profoundly, including the reduction of the ordering temperature and suppression of the magnetization plateau through the randomization of exchange interactions, the reduction of the ordered moment by enhancing quantum spin fluctuations, and the modification of the magnetic ground states, phase diagrams, and spin dynamics by possibly introducing extra spatial anisotropy through local structural distortion.

Chapter 5

$Ca_3CoNb_2O_9$

5.1 Motivation

In the two previous chapters, we mainly focus on the exotic QSSTs in the two TLAF compounds. Besides that, the multiferroicity in TLAFs is also an vibrant field of the research in the last decade[125, 126, 127, 128, 129]. It was proposed that frustration driven multiferroicity can overcome the weak magnetoelectric effect observed in the conventional type I multiferroic compounds[130]. Several microscopic models[131, 132, 133] and phenomenological[134] theories have been proposed to describe the strong coupling between the non-collinear antiferromagnetic phase and the ferroelectricity. It was also pointed out that both spin chirality and spin helicity are relevant order parameters for the multiferroicity[135]. A recent study suggested that the multiferroicity in the Y phase of RbFe(MoO4)2 is mainly associated with the spin chirality[136]. More intriguing multiferroic phases have been found in $Ba_3CoNb_2O_9$ (Co^{2+}, S = 1/2)[62], and $Ba_3NiNb_2O_9$ (Ni^{2+}, S = 1)[137]. In these compounds, ferroelectricity emerges unexpectedly in all magnetically ordering phases, including the collinear phases. And $Ba_3CoSb_2O_9$ with similar magnetically ordering phases doesn't show any ferroelectricity. Therefore, the picture of multiferroicity in TLAF is still incomplete.

In all the $Ba_3MB_2O_9$ systems described above, the magnetic ions form an equilateral triangular lattice. As discussed before, it has been reported that the substitution of Ba with Ca in triple perovskite system can lead to a lattice distortion in $Ca_3MNb_2O_9$ (M = Co,

Ni), and therefore forms an isosceles triangular lattice of the M ions[65]. In this chapter, we aim to study the effects on magnetism due to this spatial anisotropy induced by the lattice distortion in the TLAFs. Single crystalline isosceles TLAFs, CCNO was prepared for this purpose. The previous study reported that in CNNO, such lattice distortion doesn't change the 120-degree ordering state[65]. However, in this study, we found that the magnetic ordered state under zero field in CCNO is not a 120-degree ordering state, but a stripe ordered state through neutron diffraction measurements. The DC and AC susceptibility, specific heat measurements were also performed to construct the magnetic phase diagrams of CCNO. Furthermore, the dielectric constant and pyroelectric current measurements were performed to check the existence of multiferroicity in CCNO.

5.2 Sample preparation

The polycrystalline samples of CCNO are prepared by solid state reaction method. The starting materials $CaCO_3$, CoO, and Nb_2O_5 were mixed and annealed in air at 1350 °C for 40 hours. The single crystal samples of CCNO are grown by traveling-solvent floating-zone technique. Growth was carried out in air with feed and seed rod rotating in opposite directions at 25 rpm. The growth rate was 10 mm/h.

5.3 Lattice and magnetic structure

The NPD pattern of the polycrystalline CCNO at 300 K is presented in Figure 5.1(a). No additional impurity peak is found in the whole diffraction range from 10° to 125°. Similar to the previous reports[138, 139], the diffraction pattern could be fitted with a monoclinic unit cell with a = 9.6104(4) Å , b = 5.4717(7) Å , c = 16.8532(3) Å , and β = 125.713(4)°. The space group is P121/c1 with cobalt atoms at 2a (0, 0, 0) site and 2d (1/2, 1/2, 0) site. The other atoms (Ca, Nb, and O) are all located at the 8f (x, y, z) site. Detailed information of the atomic coordinates is shown in Table 5.1. The final weighted residual error $R_{wp} = 3.12$. Unlike the hexagonal Ba-based triple-perovskites, $Ba_3MB_2O_9$ (M = Co, Ni, Mn, and B = Nb, Sb) with one M atomic position, the lattice distortion from hexagonal to monoclinic structure

in CCNO leads to two Co atomic positions Figure 5.1(b). Although the Co-triangular layers still exist in the ab plane, the c axis now is not perpendicular to those triangular planes.In CCNO, the isosceles Co-triangle in ab plane now has one short side (Co1-Co1 5.4714(7) Å) and two long sides (Co1-Co2 5.5297(7) Å), respectively. The magnetic Co-layers are apart by 6.8420(3) Å and separated by the two non-magnetic Nb layers. It is noted that the interlayer distance of CCNO is shorter than that of $Ba_3CoNb_2O_9$ (7.0808(3) Å)[62] due to the monoclinic structure. Based on this structure, the applied field in the following measurements is parallel to the triangular lattice plane (a-axis) and perpendicular to the triangular plane (c*-axis), respectively.

The single-crystal neutron diffraction measurements on CCNO performed at 300 mK indicate a propagation vector (1/3 1/3 1/3) in the monoclinic system. As shown in Figure 5.2(a), if we only take the magnetic ions Co^{2+} into consideration, we can still treat this system as a slightly distorted hexagonal lattice with a = b = 5.5208(9) Å , c = 13.668(3) Å , α = 89.182(13)°, β = 90.818(13)°, and γ= 120.704(12)°. Such a small distortion allows us to simplify the refinement of the magnetic structure by working on this hexagonal lattice with one Co ions site (0 0 0). The propagation vector can be thus transformed to be (1/3 0 2/3) in the hexagonal structure. Due to the limited number of magnetic peaks and the resolution of the data, we can't exactly solve the magnetic structure. However, the k vector (1/3 0 2/3) clearly leads to a stripe ordering model, as illustrated in Figure 5.2(b). The c component of each spin can't be solved by our data. If only considering the spin projections in the ab plane, we can tell that along one long side of the triangular, all the spin projections are parallel to each other. And along the other long side as well as the short side, the spin projections are 120 degrees from the nearest neighbor spins. Such a 'triple stripe' magnetic structure is quite different from the typical 120-degree spin structure predicted in TLAFs or observed in CNNO[65].

5.4 DC and AC susceptibility

The isothermal (T = 1.0 and 1.5 K) DC magnetization curves of CCNO with applied magnetic field H ∥ a-axis are shown in Figure 5.3(a). The first derivative of the magnetization

(dM/dH) at T = 1.0 K exhibits a very sharp peak around H_{a1} = 1.3 T, followed by a small peak around H_{a2} = 3.4 T. Although one-third magnetization (1/3 M_s) is close to H_{a1}, the expected magnetization plateau with 1/3 M_s in the UUD phase is not clearly observed. Nevertheless, the features of the dM/dH at the location of the 1/3 M_s still suggest that UUD phase is stabilized between H_{a1} and H_{a2}. The saturation field H_s = 5.7 T was assigned at the broad hump on the first derivative with a saturation moment 2.0 μ_B/Co^{2+}, which leads to a g-factor as 4. The g-factor is rather large, suggesting a strong spin-orbit coupling due to the orbital degeneracy. From this saturation field and the relation $g\mu_B\mu_0 H_s = 9JS$ for a triangular lattice[36], we obtained a nearest neighbor exchange interaction J $\sim$ 3.4(3) K. Figure 5.3(b) shows the temperature dependence of the DC magnetic susceptibility χ of the polycrystalline CCNO sample at 0.1 T down to 2 K. The Curie-Weiss fit of the inverse susceptibility yields μ_{eff} = 5.47 μ_B and θ_{CW} = 57.8 K for the high temperature region and μ_{eff} = 4.03 μ_B and θ_{CW} = 9.7 K for low temperature region (shown in the inset). The effective magnetic moment values agree well with a previous report[62]. The negative Weiss temperature indicates an antiferromagnetic spin-exchange interaction. The decrease of effective moment indicates a crossover of spin state for Co^{2+} ions from high (S = 3/2) to low (S = 1/2) spin state due to the spin-orbital coupling, which is commonly observed in other Co-oxides with Co^{2+} ions in an octahedral environment[50, 1, 62].

Figure 5.4 shows the temperature dependence of the AC susceptibility (χ'(T)) of CCNO measured with H $\parallel$ a-axis (a) and H $\parallel$ c*-axis (b). At zero field, two anomalies appear at T_{N1} = 1.2 K and T_{N2} = 1.5 K. The peak positions are independent of the frequency of the ac field (not shown here), indicating a two-step magnetic ordering. For H $\parallel$ a-axis, both T_{N1} and T_{N2} decrease with increasing field. The T_{N1} feature disappears with field above 1.5 T. For H $\parallel$ c*-axis, T_{N1} and T_{N2} decrease with increasing field too. The features of T_{N1} and T_{N2} don't show obvious differences between them.

Measurements on magnetic field dependence of AC susceptibility (χ'(H)) were also carried out for CCNO. The scans with H $\parallel$ c*-axis didn't show any clear features and were not shown here. The scans with H $\parallel$ a-axis were plotted in Figure 5.4(c). To clarify possible phase transitions, we used the 2.5 K data as a background and subtracted it from other low temperature data. Therefore, the data shown in Figure 5.4 (c) is $\Delta\chi = \chi'(H,T)$ –

χ'(H,2.5K). The data at 0.02 K shows two clear anomalies at H_{a1} = 1.4 T and H_{a2} = 3.3 T below saturation field H_S = 5.8 T. These features agree well with what we observed from the dc magnetization data and again suggest the existence of UUD phase. The similarity between dM/dH and the χ'(H) data is expected from the nature of χ(H) (directly probing the derivative of the DC magnetization). Both H_{a1} and H_{a2} decrease with increasing temperatures.

5.5 Specific heat

Figure 5.5 (a) and (b) show the temperature dependence of specific heat of CCNO ($C_p(T)$) with H ∥ a-axis and H ∥ c*-axis, respectively. At zero field, two sharp peaks show at T_{N1} = 1.2 K and T_{N2} = 1.5 K, again supporting a two-step magnetic ordering. With increasing field along the a-axis and c*-axis, both T_{N1} and T_{N2} decrease and only T_{N2} is visible above 2 T. We note here that Dai et al. suggested a long-range anti-ferromagnetic order at 1.45 K followed by a spin glass ground state below 1.2 K from their works based on polycrystalline samples[138]. Considering the sharp $C_p(T)$ anomalies at both T_Ns from our data and the frequency-independent peaks in ac susceptibility, it is more likely that both transitions are with long-range ordering nature.

5.6 Dielectric constant

Figure 5.6(a) and (b) show the temperature dependence of the real part of the dielectric constant $\epsilon'(T)$ of CCNO with both H and electric field (E) applied along the a-axis or c*-axis, respectively. With H ∥ a-axis, a small peak appears at a temperature close to T_{N1} and there is no noticeable feature around T_{N2}. With increasing fields, the T_{N1} peak shifts to lower temperatures and becomes weaker. It disappears eventually above 1 T. With H ∥ c*-axis, the $\epsilon'(T)$ curve shows two anomalies at T_{N1} = 1.3 K and T_{N2} = 1.5 K. And both T_{N1} and T_{N2} decrease with increasing fields. As shown in Figure 5.6(c), with H ∥ a-axis, the field dependence of ϵ'(H) measured at 0.3 K and 0.7 K show a broad peak between 1 T and 3 T. The derivative of ϵ'(H) shows two anomalies more clearly at 1.3 T and 3.4 T, which are

again consistent with H_{a1} and H_{a2} observed from the ac susceptibility and dc magnetization. The peak becomes weaker as the temperature increases. The ϵ'(H) curve with H ∥ c*-axis also shows two anomalies. Here we assign them as H_{c1} and the saturation field H_s, respectively. To investigate whether the anomalies in the dielectric constant origin from the ferroelectricity, we measured pyroelectric current while sweeping the temperature across the transitions. No noticeable pyroelectric current signals were observed (not shown here), hence no spontaneous electric polarization in CCNO. This is different from $Ba_3CoNb_2O_9$, where the ferroelectricity with spontaneous electric polarization of an order of $0.3\mu C/m^2$ exist at all magnetically ordered states[62]. Actually, the weak feature in the dielectric constant in Figure 5.6 already indicates a lack of a ferroelectric order, which would give a stronger dielectric constant anomaly[140]. The absence of ferroelectricity in CCNO and appearance of ferroelectricity in $Ba_3CoNb_2O_9$ could be related to their different magnetic ground states, which are stripe order in CCNO but 120-degree ordering in $Ba_3CoNb_2O_9$.

To confirm the relation between the existence of ferroelectricity and the magnetic ground state, polarization measurements were also performed on CNNO, which also has distorted lattice but keeps the 120-degree magnetic ground state. Figure 5.7 (a)-(d) show the pyroelectric current measurements with different combinations of H and E directions. Figure 5.7 (e)-(h) show the corresponding spontaneous polarization (P), which was obtained by integrating the pyroelectric current with respect to time. The sharp peak of the pyroelectric current observed below 4 K for all conditions and the reversible polarization confirms the ferroelectric ground state in CNNO.

5.7 Discussion

Based on all the data presented above, magnetic phase diagrams of CCNO are constructed. The phase diagram with H ∥ a-axis (Figure 5.8(a)) shows more features than the one with H ∥ c*-axis (Figure 5.8(b)) for CCNO. Therefore, we argue this compound has an easy-plane anisotropy. The theories have predicted successive magnetic phase transitions in TLAFs between Y, UUD with $1/3M_s$ and an oblique phase under the magnetic field[44, 141, 43]. In our work, three magnetic phases are identified in addition to the paramagnetic phase above

T_{N2} and the polarized phase above H_s with H ∥ a-axis, which are quantitatively consistent with the theoretical studies. However, as we discussed in the previous section, the long-range ordered phase in this system at zero field is a stripe spin structure other than a 120-degree spin structure. The distortion in the triangular lattice induces spatial anisotropy and could be the reason for the appearance of a stripe ordered state. On the other hand, for CNNO, with similar lattice distortion, it still shows a 120-degree spin structure. Therefore, how the lattice distortion exactly affects the magnetic ground state could also depend on the spin number of $Ca_3MNb_2O_9$.

Since the zero-field ordered phase in CCNO is different from the theories on the ideal triangular lattice. It is reasonable to argue that the low-field phase for H ∥ a-axis, I_a, is not the Y phase under the assumption. Here we name it as canted stripe phase. Phase II_a is assigned to be UUD because of the peak-valley-peak features around the 1/3 M_s in AC susceptibility measurements. The appearance of the UUD phase indicates that the Zeeman energy of spins in a higher magnetic field has dominated the Hamiltonian and the geometrical frustration persists under magnetic field so that the magnetic phase of our system starts to agree with the theories on the ideal triangular lattice. Following this consideration, we argue the phase III_a to be oblique phase since the magnetic field is even higher. Meanwhile, the UUD phase regime becomes larger with the decreasing temperature near TN's until its field range is almost unchanged below 1.0 K. This implies that the quantum fluctuations are influential in stabilizing the UUD phase. Chubukov[37] estimated the critical fields for such UUD phase in the case of isotropic Heisenberg TLAF using the spin-wave approach. Up to the first order of 1/S expansion, they obtained H_{a1}=H_s/3(10.084/S) and H_{a2}=H_s/3(1 + 0.215/S). In our case, with H_s = 5.7 T and S = 1/2, it gives H_{a1} = 1.58 T, and H_{a2} = 2.72 T. Experimentally, H_{a1} from our measurements agrees excellently with the calculation, while H_{a2} is larger than the calculated one by 23%. This discrepancy may be due to the model being based on the equilateral TLAFs. The overall features of the UUD phase are similar to those of the low spin TLAFs such as $Ba_3CoNb_2O_9$ (Co^{2+}, S = 1/2)[62] and $Ba_3NiNb_2O_9$ (Ni^{2+}, S = 1)[137] but different from the large spin TLAFs such as $Ba_3MnNb_2O_9$ (Mn^{2+},S = 5/2)[142], $RbFe(MoO_4)_2$ (Fe^{3+}, S = 5/2)[143, 144], where the UUD phase become less stable at low temperatures as the thermal fluctuations decrease. The fact that these two

distinct groups can be classified solely by the magnitude of the spin is important evidence of the role of quantum fluctuations for the UUD phase. In Figure 5.8 (b), the magnetic phase diagram with H ∥ c*-axis only shows two phases before fully polarized. More work is required to reveal the detailed spin configurations of these two phases. Here we tentatively assigned phase IIc as an oblique phase.

Another notable feature is the two-step phase transition from the paramagnetic phase to the ordering states at low fields (H << $H_s/3$) in both directions. It has been predicted that when the magnetic anisotropy energy is negative, a two-step phase transition can be observed[145]. It also suggests that the transitions at T_{N2} and T_{N1} correspond to a phase transition into the UUD phase and another phase transition into the low-field co-planar phase, respectively. Experimentally, a few compounds with easy-axis anisotropy showed the two-step phase transition at low fields[146, 147, 148]. On the other hand, a single-step phase transition appears in a system with easy-plane anisotropy at low field regime[143, 149]. In our case, the extra spatial anisotropy in the ab plane related to the lattice distortion, on top of the easy plane anisotropy, could be the reason for the two-step ordering process.

5.8 Summary

In conclusion, our experiments on single crystalline CCNO showed the spatial anisotropy on TLAFs is likely to lead to a two-step magnetic ordering even with weak easy-plane anisotropy and lead to rearrangement of spin configuration in magnetic ordering state. Starting from the stripe long-range ordering spin structure under zero field, we observed a series of magnetic phase transitions with H ∥ a and H ∥ c*. Meanwhile, the ferroelectricity is found to be absent in this compound. Considering the existence of ferroelectricity in the isostructure compound CNNO with 120-degree spin structure as ground state, we confirmed that the ferroelectricity in such TLAFs is related to the 120-degree magnetic ordering structure.

Chapter 6

$Na_2BaCo(PO_4)_2$

6.1 Motivation

In this chapter, we are going to include both the possible QSL state and QSSTs in the study. Recently, R. Zhong et al. reported a new Co-based triangular lattice antiferromagnet NBCPO[150] as a QSL candidate. This compound caught our attention because it is a rare example of TLAFs with easy-axis anisotropy of which we can obtain high quality single crystalline samples. This system has a trigonal crystal structure with lattice parameter a = 5.3185 Å and c = 7.0081 Å. The magnetic CoO_6 octahedra form a triangular network in the ab plane, separated by a layer of nonmagnetic BaO_{12} polyhedra. Meanwhile, the Na^+ ions fill the gaps in the CoO_6 layers (Figure 6.1 (a) and (b)). Overall, no site mixture among the ions has been observed. The magnetic susceptibility, INS spectrum, and specific heat data show no magnetic ordering down to 50 mK but with large magnetic specific heat and localized low-energy spin fluctuations. To confirm whether this system is a truly gapless QSL or not, it is crucial to look for the possible existence of itinerant spinons. Moreover, until now, no magnetic phase diagram has been reported for this new TLAF and its possibility for QSSTs is awaiting exploration.

6.2 Sample preparation

Single crystals of NBCPO were synthesized by the flux method. Dried Na_2CO_3, $BaCO_3$, CoO, and $(NH_4)_2HPO_4$ were mixed stoichiometrically and ground well with the flux media NaCl in a molar ratio of 1:5. The mixed starting materials were loaded in an platinum crucible and then heated up to 950 °C for 2 h followed by a slow cooling procedure of 3 °C/h to 750 °C. The obtained pink single crystals were manually separated from the crucible in water.

6.3 Magnetic susceptibility

Figure 6.1(c) shows its inverse of the DC magnetic susceptibility ($1/\chi$) with applied field H $\parallel$ ab plane. A change of slope is observed around 50 K. The effective moment is estimated to be 5.37 μ_B for $150 \leq T \leq 300K$ and 4.0 μ_B for $2 \leq T \leq 20K$ by using the linear Curie-Weiss fittings. This decrease of effective moment indicates a crossover of spin state for Co^{2+} ions from S = 3/2 at high temperatures to an effective spin-1/2 at low temperatures. The θ_{CW} = -2.5 K obtained at low temperatures fitting represents its intrinsic antiferromagnetic exchange interaction energy level. According to the mean field theory, θ_{CW} is given as $(-zJS(S+1))/3k_B$, where J is the exchange interaction of the Heisenberg Hamiltonian $J\sum_{(i,j)} S_iS_j$, and z is the number of nearest neighbors. For the effective S = 1/ 2 triangular lattice with z = 6, we obtained $J/k_B = -2/3\theta_{CW} = 1.7K$.

6.4 Thermal conductivity

Figure 6.2(a) shows the zero-field thermal conductivity of NBCPO in temperature range from 70 mK to 30 K. It behaves like a usual insulting crystal. The peak at 12 K with a large value of 90 W/Km can be understood as the so-called phonon peak. It is notable such a large phonon peak indicates high quality of the single crystal samples. Also shown are the thermal conductivity in 14 T field, either along the c or the a axis, which can increase the κ at most temperatures up to 7 K.

Figures 6.2(b)-(d) shows the ultralow-temperature thermal conductivity at 0 and 14 T fields. Several features are noteworthy. First, all these data are well fitted by $\kappa/T = \kappa_0/T + bT^2$ with b as a constant in a very broad temperature range (from several tens to 500 mK or more), while the fitting parameters κ_0/T and b are clearly different for them. Second, in zero field the fitting gives $\kappa_0/T = 0.0062 W/K^{-2}m^{-1}$, that is, the presence of a residual value in κ/T while extending to zero temperature is clearly resolved. Third, the fitting curves in Figure 6.2 yield intercepts of $0 \pm 0.0005 WK^{-2}m^{-1}$ for data with 14 T $\parallel$ c and 14 T $\parallel$ a. The error is at least one order of magnitude smaller than the zero-field κ_0/T value, which indicates zero κ_0/T for the 14 T data.

6.5 Specific heat

As shown in the inset to Figure 6.2(b), the zero-field $\kappa(T)$ data also shows a very weak anomaly around 100 mK. To learn the nature of this anomaly, the specific heat (C_p) was measured at very low temperatures down to 50 mK, as shown in Figure 6.3. At zero field, the C_p exhibits a broad peak around 630 mK followed by a small and sharp peak at 148 mK. This sharp peak should represent an antiferromagnetic ordering, which is likely related to the anomaly observed from the zero field $\kappa(T)$. With increasing field along the c axis, this peak's position shifts to $\sim$ 310 mK for μ_0H = 0.5 and 1 T; meanwhile, its intensity abruptly increases for μ_0H = 0.5 and 1 T and then this peak disappears for μ_0H = 1.5 T, as shown in Figure 6.3(a). By assuming that the lattice contribution can be described by $C_{ph} = \beta T^3 + \beta_5 T^5 + \beta_7 T^7$ with $\beta = 8.83 \times 10^{-4} JK^{-4}mol^{-1}$, $\beta_5 = -3.32 \times 10^{-7} JK^{-6}mol^{-1}$, and $\beta_7 = 6.67 \times 10^{-11} JK^{-8}mol^{-1}$(Figure 6.4), the change of magnetic entropy below 4 K, ΔS_m, was calculated by integrating $(C_p - C_{ph})/T$ (Figure 6.3(b)). The obtained values are 5.1 and 5.4 $JK^{-1}mol^{-1}$ for μ_0H = 0 and 1 T, respectively, which are approaching the value of Rln2. This is another strong evidence that NBCPO can be treated as an effective spin-1/2 system. At zero field, the recovered entropy below 200 mK (where the peak starts) is 1.6 $JK^{-1}mol^{-1}$. This is only 28% of Rln2, which indicates the strong spin fluctuations above T_N. A small upturn of the specific heat is observed at the lowest temperatures, which could be attributed to a contribution from the nuclear entropy. Figure 6.3(c) shows the specific

heat data for H ∥ a. Similar to the results for H ∥ c, the low magnetic fields along the a axis can also change the position of the peak at 148 mK but with weaker field dependence.

6.6 Residual thermal conductivity

It is abnormal for NBCPO to exhibit a non-zero κ_0/T term extrapolated from the data above T_N. One possible scenario is that it behaves as a QSL above $T_{\rm N}$ with gapless magnetic excitations, which give rise to power-law temperature dependences of the low temperature physical properties. Indeed, the reported INS spectrum[150] and specific heat data reported here support the presence of strong spin fluctuations above $T_{\rm N}$. While the 2D QSL is stable at zero temperature in the strict sense, it is also known that QSL behavior, such as spinon excitations can survive at a finite temperature regime if the temperature scale is smaller than the exchange interaction, J. To our knowledge, a couple of quantum magnets exhibit quantum spin disordered states including QSL in a temperature range $T_N < T <$ J due to the combination of strong geometrical frustration with enhanced quantum spin fluctuations for spin-1/2, as present in NBCPO with $T_N = 148$ mK and J $\sim$ 1.7 K. One good example is the Volborthite, $Cu_3V_2O_7(OH)_2 \cdot 2H_2O$, with a 2D distorted kagome lattice of Cu^{2+} (S = 1/2) ions, which antiferromagnetically orders at $T_N \sim 1$ K with exchange constant J $\sim$ 60 K [16, 151]. A finite linear T-dependent contribution of specific heat extrapolated to T = 0 K[16] and a negative thermal Hall conductivity observed above T_N[151] both strongly support the presence of a QSL state with gapless spin excitations above T_N for Volborthite. While no clear non-zero κ_0/T term was observed for Volborthite due to its relatively high ordering temperature, the estimated mean free path of the spin excitations from the 8 K magnetic thermal conductivity is about 80 times its inter-spin distance, which indicates its spin excitations are highly mobile[151]. The related theoretical work also proposes the existence of spinon Fermi surface in Volborthite above κ_0/T[152, 153]. Another relevant example is pyrochlore $Yb_2Ti_2O_7$ with effective spin-1/2 Yb^{3+} ions, which ferromagnetically orders at $T_C \sim 0.2$ K[154]. For $Yb_2Ti_2O_7$, the XY and off diagonal components of the interactions, $J_\perp \sim 0.58$ K and $J_{z^+} \sim 1.7$ K, respectively, produce quantum spin fluctuations[155, 156]. It's reported specific data suggests strong quantum fluctuations above T_C [157, 158]. Its

observed diffuse scattering and pinch point structure of the INS spectrum and related model calculation further suggest the presence of a quantum spin ice state above T_C[159]. Lately, the unusual behavior of the magneto-thermal conductivity[160] and thermal Hall conductivity[161] suggests the emergence of highly itinerant quantum magnetic monopoles in this quantum spin ice state.

By following Ref.[21]'s method, we estimate the mean free path (l_s) and life time of the spin excitation (τ_s) of the quasiparticles responsible for the excitations by calculating $\frac{\kappa_0}{T} = \frac{\pi k_B^2}{9\hbar}\frac{l_s}{ad} = \frac{\pi}{9}(\frac{k_B}{\hbar})^2\frac{J}{d}\tau_s$. Here a ($\sim 5.32$ Å) and d (~ 7.01 Å) are nearest-neighbor and interlayer spin distance, respectively. From the observed $\kappa_0/T = 0.0062W/K^2m$, the l_s is obtained as 36.6 Å , indicating the excitations are mobile to a distance 7 times as long as the inter-spin distance without being scattered. By using J = 1.7 K, the obtained τ_s is 3.0910^{-11} s. Third, in high magnetic field of 14 T, although the is much larger than the zero-field data, the fitting gives a negligibly small value of, or vanishing κ_0/T. It is very reasonable since 14 T is strong enough to polarize all spins and completely suppress the spinon excitations of the QSL state. Thus, the 14 T data should be a result of pure phonon heat transport. From the specific heat data, it is found that the phonon specific heat can be approximated as $C_{ph} = \beta T^3$ at very low temperatures with the coefficient $\beta = 8.8310^{-4}J/K^4mol$. The phonon velocity can be calculated from the β value as $v_{ph} = 2430m/s$. The phonon thermal conductivity in the ballistic scattering limit is $\kappa_{ph} = (1/3)C_{ph}v_{ph}l_{ph}$, where the phonon mean free path is determined by the averaged sample width of $l_{ph} = 2\sqrt{A/\pi} = 0.32mm$, for this sample. Thus, the phonon thermal conductivity at low temperature is expected as $\kappa_{ph} = 2.21T^3W/Km$. Note that this estimation is different from the 14 T data by only a factor of 2, which is acceptable. If one assume the 14 T data is purely phonon term, much smaller data in zero field indicates that the phonon ballistic scattering limit is not achieved although they show a pretty good behavior of $\kappa_0/T + bT^2$. Therefore, in zero field the phonons are always suffering some scattering effect besides the boundary. Apparently, at very low temperatures only the magnetic excitations can take the role of phonon scattering.

Another possible scenario is that this non-zero κ_0/T term is related to other abnormal quasiparticles besides spinon, which means the high-T ($> T_N$) phase may not be ascribed to

the QSL. Either way, future studies are desirable to learn the exact origin for this interesting residual thermal conductivity in NBCPO.

6.7 Field dependence of thermal conductivity and AC susceptibility

The dramatic change of the C_p peak with H $\parallel$ c suggests the possibility of spin state transitions. For further investigation, more detailed κ and AC susceptibility in magnetic fields were measured. For H $\parallel$ c, the κ(H) curve at 90 mK exhibits four minimums at H_{c1}, H_{c2}, H_{c3}, and H_{c4} (Figure 6.5(a)). With increasing temperatures, κ(H) only exhibits two minimums at 151 mK and no minimum at $T > 300$ mK (not shown here). The $\kappa(T)$ measured at 0.5 and 1.0 T (Figure 6.5(b)) clearly shows slope change around 300 mK, which is consistent with the Cp peaks' position measured at the same fields. The AC susceptibility, χ', measured at 20 mK (Figure 6.5(c)) shows three peaks at H_{c1}, H_{c2}, and H_{c3}, the values of which are consistent with those observed from κ(H). With increasing temperature, the H_{c1} peak shifts to higher fields and the H_{c2} and H_{c3} peaks shifts to lower fields. At $T > 280$ mK, the peaks almost disappear. Since the χ' represents the derivative of the DC magnetization M(H), here we calculated M(H) by integrating χ' measured at 20 mK. The obtained M(H) (Figure 6.5(d)) clearly shows a plateau regime between H_{c1} and H_{c2} and a slope change at H_{c3} followed by the saturation around 2.5 T. Although we do not know the absolute value of M(H) here, it is obvious that the magnetization of the plateau (around 0.31, here we scaled the maximum value of the M(H) to 1) is 1/3 of the saturation value (around 0.92 after we subtract the Van Vleck paramagnetic background, which is the dashed line in Figure 6.3(f)). For comparison, the above measurements were also performed for H $\parallel$ a. The κ(H) curve (Figure 6.6(a)) at 92 mK shows two minimums at $H_{a1} = 0.31$ T and $H_{a2} = 1.46$ T, while the $\kappa(T)$ (Figure 6.6(b)) at 0.5 and 1 T shows no anomaly. The χ' (Figure 6.6(c) measured at 20 mK shows a broad peak around H_{a1} and a sharp peak around H_{a2}. With increasing temperature, the H_{a1} and H_{a2} shift to higher and lower fields, respectively, and

both disappear at $T > 290$ mK. The calculated M(H) at 20 mK shows a slope change around 1/3 M_s position. All these results are clearly different from those for H ∥ c.

6.8 Phase diagram

Based on the critical fields and ordering temperatures presented above, the magnetic phase diagrams for H ∥ c and H ∥ a are constructed in Fig. 6.7. For H ∥ a, since both the κ(H) and χ' data consistently show two critical fields and H_{a2} is very close to the field where the magnetization becomes flat (or saturated), it is natural for us to assign H_{a2} as the saturation field and H_{a1} as a critical field for a spin state transition. On the other hand, for H ∥ c, the κ(H) exhibits four critical fields while the χ' shows three. Here we assign the H_{c4} as the saturation field for two reasons: (i) if we assign H_{c3} as the saturation field, it will be difficult to understand why there is still a possible spin state transition at $H_{c4} > H_{c3}$ after all spins have been polarized; (ii) a close look of the calculated M(H) curve shows that H_{c3} represents a slope change before the magnetization becomes flat, which most likely represents a spin state transition. One possible situation is that since this H_{c3} peak of χ' data is so close to the saturation field position, it may smear out the expected χ' peak at H_{c4}. Accordingly, besides the paramagnetic phase at high temperatures and fully polarized phase at high fields, with increasing field, there are four phases for H ∥ c (Fig. 7.6(a)) and two phases for H ∥ a (Fig. 7.6(b)). Now we compare the phase diagrams of NBCPO to those of BCSO. For H ∥ c we are confident that the phase II is the UUD phase based on the 1/3M_s plateau observed at 22 mK. Since the 120-degree spin structure is a pre-required phase for the appearance of UUD phase, we ascribe the phase I as the canted 120-degree spin structure. Whether the phase III and IV are the V and V' phase or the phase I and II for H ∥ a are the umbrella and V phases or not cannot be said at this stage. Further studies such as neutron diffraction are needed to address this question. We emphasize that in NBCPO, the UUD phase only survives for H ∥ c, which strongly suggests its easy axis anisotropy as the theory predicted[48]. $Ba_3CoSb_2O_9$ and $AYbCh_2$ are both TLAFs with easy plane anisotropy. To our knowledge, NBCPO is a very rare example of spin-1/2 TLAF with single crystalline form to exhibit series of QSSTs along the easy axis. Another two examples for spin-1/2 TLAFs with easy axis anisotropy to

show UUD phase are $Ba_3CoNb_2O_9$[62, 64] and $Ba_2La_2CoTe_2O_{12}$[162], but both of them are polycrystalline form.

6.9 Summary

In summary, we clearly observed a nonzero residual thermal conductivity, κ_0/T, extrapolated from the data above T_N ($\sim$148 mK) in an effective spin-1/2 triangular antiferromagnet NBCPO. This abnormal feature indicates that NBCPO possibly behaves as a gapless QSL with itinerant spin excitations above T_N. Moreover, its strong quantum spin fluctuations persist below TN and help to stabilize a series of spin state transitions while approaching zero temperature. With applied field along the c axis, this includes the UUD phase with a $1/3M_s$ magnetization plateau. This makes NBCPO a unique TLAF with easy axis anisotropy to exhibit a UUD phase.

Chapter 7

Summary

This dissertation focused on the exotic magnetism of spin 1/2 TLAFs. Starting from a well studied system BSCO, we have done a systematic work to probe the effects of different perturbations (site disorder, lattice distortion, and the change of spin anisotropy) on its exotic quantum magnetism .

In chapter 3, we mapped out the complete magnetic phase diagrams of BCSO for H $\parallel$ a and c-axis and angular dependence at 0.32 T by using low temperature and high field measurements on specific heat, thermal conductivity, magnetic torque, and neutron diffraction. Several newly observed features including new phase boundaries appearing below 1 K and around 6 T for H $\parallel$ a-axis and around 30 T for H $\parallel$ c-axis are not expected by current theory. The experimental angle-dependent phase diagram also deviates from the theoretically predicted one on several aspects. Our results indicate that the present $S = 1/2$, two layer $J - J_z - J'$ Heisenberg antiferromagnetic model captures many aspects of the behavior of BCSO but must now be modified or expanded in some way to account for the second order nature of the phase transitions observed here, the unexpected emergence of additional phase transitions at low temperature, and the evolution of the phase diagram with field orientation.

In chapter 4, we reported the profound effect of Sr-doping on the non-magnetic Ba^{2+} ion sites in BCSO. We argued that (i)the randomness in exchange interactions reduce the ordering temperature and suppress the magnetization plateau feature of UUD phase. (ii)The enhanced quantum spin fluctuations suppress the ordered magnetic moment. (iii) The doping probably induce an extra spatial anisotropy through local structural distortion so that the

magnetic ground state in modified slightly. And such a slight modification of magnetic ground state under zero field evolves into large discrepancies under magnetic field, which greatly change the magnetic phase diagram and INS spectrum. This study serves as a good example for demonstrating that disorder on non-magnetic ion sites play a complex role on quantum magnetism beyond the expected disruption of the exchange interactions. In fact, such kind of disorder can be treated as an perturbation to efficiently tune the magnetic properties of quantum magnets.

In chapter 5, our studies on single crystalline CCNO show that it is a TLAF with spatial anisotropy. This spatial anisotropy is likely to lead to a two-step magnetic ordering with weak easy-plane anisotropy. We observed a series of magnetic phase transitions with H $\parallel$ a-axis and H $\parallel$ c*-axis, starting from the stripe long-range ordering spin structure under zero field. This spin structure also eliminates the ferroelectricity in this compound. Meanwhile, the dielectric constant and pyroelectric current measurements for CNNO with 120-degree spin structure as the ground state clearly show coexistence of ferroelectricity and spin state transitions, as observed for $Ba_3CoNb_2O_9$[62] and $Ba_3NiNb_2O_9$[137]. It confirms that the ferroelectricity in such TLAFs is related to the 120-degree magnetic ordering structure.

In chapter 6, although our research on the quantum spin liquid candidate NBCPO confirmed a long range magnetic ordering below T_N ($\sim$148 mK), the clear nonzero residual thermal conductivity κ_0/T, extrapolated from the data above T_N, suggests a possible gapless QSL state with itinerant spin excitations above T_N. Furthermore, we observed a series of QSSTs under magnetic field stablized by the strong quantum spin fluctuations persisting below T_N in NBCPO. Its magnetic phase diagrams were constructed accordingly with field applied along a and c-axis. With applied field along the c axis, a UUD phase with a $1/3M_s$ magnetization plateau was reported. This makes NBCPO a unique TLAF with easy-axis anisotropy to exhibit a UUD phase.

Bibliography

[1] Nathanael Alexander Fortune, Qing Huang, Tao Hong, J Ma, ES Choi, Scott T Hannahs, ZY Zhao, XF Sun, Y Takano, and HD Zhou. Evolution of magnetic field induced ordering in the layered quantum heisenberg triangular-lattice antiferromagnet ba 3 cosb 2 o 9. *Physical Review B*, 103(18):184425, 2021. xii, 33, 77, 78

[2] Leon Balents. Spin liquids in frustrated magnets. *Nature*, 464(7286):199–208, 2010. 2

[3] Lucile Savary and Leon Balents. Quantum spin liquids: a review. *Reports on Progress in Physics*, 80(1):016502, 2016. 2

[4] Yi Zhou, Kazushi Kanoda, and Tai-Kai Ng. Quantum spin liquid states. *Reviews of Modern Physics*, 89(2):025003, 2017. 2

[5] Johannes Knolle and Roderich Moessner. A field guide to spin liquids. *Annual Review of Condensed Matter Physics*, 10:451–472, 2019. 2

[6] GH Wannier. Antiferromagnetism. the triangular ising net. *Physical Review*, 79(2):357, 1950. 2

[7] Philip W Anderson. Resonating valence bonds: A new kind of insulator? *Materials Research Bulletin*, 8(2):153–160, 1973. 2

[8] Philip W Anderson. The resonating valence bond state in La_2CuO_4 and superconductivity. *science*, 235(4793):1196–1198, 1987. 2

[9] Chetan Nayak, Steven H Simon, Ady Stern, Michael Freedman, and Sankar Das Sarma. Non-abelian anyons and topological quantum computation. *Reviews of Modern Physics*, 80(3):1083, 2008. 2

[10] Tian-Heng Han, Joel S Helton, Shaoyan Chu, Daniel G Nocera, Jose A Rodriguez-Rivera, Collin Broholm, and Young S Lee. Fractionalized excitations in the spin-liquid state of a kagome-lattice antiferromagnet. *Nature*, 492(7429):406–410, 2012. 2

[11] Matthias Punk, Debanjan Chowdhury, and Subir Sachdev. Topological excitations and the dynamic structure factor of spin liquids on the kagome lattice. *Nature Physics*, 10(4):289–293, 2014. 2

[12] Masanori Kohno, Oleg A Starykh, and Leon Balents. Spinons and triplons in spatially anisotropic frustrated antiferromagnets. *Nature Physics*, 3(11):790–795, 2007. 2

[13] Zohar Nussinov, CD Batista, Bruce Normand, and SA Trugman. High-dimensional fractionalization and spinon deconfinement in pyrochlore antiferromagnets. *Physical Review B*, 75(9):094411, 2007. 2

[14] Yao Shen, Yao-Dong Li, Hongliang Wo, Yuesheng Li, Shoudong Shen, Bingying Pan, Qisi Wang, HC Walker, Paul Steffens, Martin Boehm, et al. Evidence for a spinon fermi surface in a triangular-lattice quantum-spin-liquid candidate. *Nature*, 540(7634):559–562, 2016. 2

[15] Joseph AM Paddison, Marcus Daum, Zhiling Dun, Georg Ehlers, Yaohua Liu, Matthew B Stone, Haidong Zhou, and Martin Mourigal. Continuous excitations of the triangular-lattice quantum spin liquid ybmggao 4. *Nature Physics*, 13(2):117–122, 2017. 2

[16] Satoshi Yamashita, Tomoya Moriura, Yasuhiro Nakazawa, Hiroyuki Yoshida, Yoshihiko Okamoto, and Zenji Hiroi. Thermodynamic properties of the kagomé lattice in volborthite. *Journal of the Physical Society of Japan*, 79(8):083710, 2010. 2, 41

[17] Olexei I Motrunich. Variational study of triangular lattice spin-1/ 2 model with ring exchanges and spin liquid state in κ-(et) 2 cu 2 (cn) 3. *Physical Review B*, 72(4):045105, 2005. 2

[18] Sung-Sik Lee and Patrick A Lee. U (1) gauge theory of the hubbard model: Spin liquid states and possible application to κ-(bedt- ttf) 2 cu 2 (cn) 3. *Physical review letters*, 95(3):036403, 2005. 2

[19] Cody P Nave and Patrick A Lee. Transport properties of a spinon fermi surface coupled to a u (1) gauge field. *Physical Review B*, 76(23):235124, 2007. 2, 11

[20] Yochai Werman, Shubhayu Chatterjee, Siddhardh C Morampudi, and Erez Berg. Signatures of fractionalization in spin liquids from interlayer thermal transport. *Physical Review X*, 8(3):031064, 2018. 2, 11

[21] Minoru Yamashita, Norihito Nakata, Yoshinori Senshu, Masaki Nagata, Hiroshi M Yamamoto, Reizo Kato, Takasada Shibauchi, and Yuji Matsuda. Highly mobile gapless excitations in a two-dimensional candidate quantum spin liquid. *Science*, 328(5983):1246–1248, 2010. 2, 11, 42

[22] Minoru Yamashita. Boundary-limited and glassy-like phonon thermal conduction in etme3sb [pd (dmit) 2] 2. *Journal of the Physical Society of Japan*, 88(8):083702, 2019. 2, 11

[23] Yuesheng Li, Devashibhai Adroja, David Voneshen, Robert I Bewley, Qingming Zhang, Alexander A Tsirlin, and Philipp Gegenwart. Nearest-neighbour resonating valence bonds in ybmggao 4. *Nature communications*, 8(1):1–6, 2017. 2

[24] Yao Shen, Yao-Dong Li, HC Walker, Paul Steffens, Martin Boehm, Xiaowen Zhang, Shoudong Shen, Hongliang Wo, Gang Chen, and Jun Zhao. Fractionalized excitations in the partially magnetized spin liquid candidate ybmggao 4. *Nature communications*, 9(1):1–7, 2018. 2

[25] Yuesheng Li, Haijun Liao, Zhen Zhang, Shiyan Li, Feng Jin, Langsheng Ling, Lei Zhang, Youming Zou, Li Pi, Zhaorong Yang, et al. Gapless quantum spin liquid ground state in the two-dimensional spin-1/2 triangular antiferromagnet ybmggao 4. *Scientific reports*, 5(1):1–8, 2015. 2, 21

[26] Yuesheng Li, Devashibhai Adroja, Pabitra K Biswas, Peter J Baker, Qian Zhang, Juanjuan Liu, Alexander A Tsirlin, Philipp Gegenwart, and Qingming Zhang. Muon spin relaxation evidence for the u (1) quantum spin-liquid ground state in the triangular antiferromagnet ybmggao 4. *Phys. Rev. Lett.*, 117(9):097201, 2016. 2

[27] Yuesheng Li, Sebastian Bachus, Benqiong Liu, Igor Radelytskyi, Alexandre Bertin, Astrid Schneidewind, Yoshifumi Tokiwa, Alexander A Tsirlin, and Philipp Gegenwart. Rearrangement of uncorrelated valence bonds evidenced by low-energy spin excitations in ybmggao 4. *Phys. Rev. Lett.*, 122(13):137201, 2019. 2

[28] Yang Xu, Jun Zhang, YS Li, YJ Yu, XC Hong, QM Zhang, and SY Li. Absence of magnetic thermal conductivity in the quantum spin-liquid candidate ybmggao 4. *Phys. Rev. Lett.*, 117(26):267202, 2016. 2, 21

[29] Zhen Ma, Jinghui Wang, Zhao-Yang Dong, Jun Zhang, Shichao Li, Shu-Han Zheng, Yunjie Yu, Wei Wang, Liqiang Che, Kejing Ran, et al. Spin-glass ground state in a triangular-lattice compound ybzngao 4. *Phys. Rev. Lett.*, 120(8):087201, 2018. 2, 21

[30] X Rao, G Hussain, Q Huang, WJ Chu, N Li, X Zhao, Z Dun, ES Choi, T Asaba, L Chen, et al. Survival of itinerant excitations and quantum spin state transitions in YbMgGaO4 with chemical disorder. *Nature Communications*, 12(1):4949, 2021. 2

[31] David A Huse and Veit Elser. Simple variational wave functions for two-dimensional heisenberg spin-1/2 antiferromagnets. *Physical review letters*, 60(24):2531, 1988. 3

[32] B Bernu, C Lhuillier, and L Pierre. Signature of néel order in exact spectra of quantum antiferromagnets on finite lattices. *Physical review letters*, 69(17):2590, 1992. 3

[33] N Elstner, RRP Singh, and AP Young. Finite temperature properties of the spin-1/2 heisenberg antiferromagnet on the triangular lattice. *Physical review letters*, 71(10):1629, 1993. 3

[34] Luca Capriotti, Adolfo E Trumper, and Sandro Sorella. Long-range néel order in the triangular heisenberg model. *Physical review letters*, 82(19):3899, 1999. 3

[35] Hikaru Kawamura. Spin-wave analysis of the antiferromagnetic plane rotator model on the triangular lattice–symmetry breaking in a magnetic field. *Journal of the Physical Society of Japan*, 53(8):2452–2455, 1984. 3

[36] Hikaru Kawamura and Seiji Miyashita. Phase transition of the heisenberg antiferromagnet on the triangular lattice in a magnetic field. *Journal of the Physical Society of Japan*, 54(12):4530–4538, 1985. 3, 33

[37] Andrey V Chubukov. Chiral, nematic, and dimer states in quantum spin chains. *Physical Review B*, 44(9):4693, 1991. 3, 36

[38] Jie Ma, Yoshitomo Kamiya, Tao Hong, HB Cao, Georg Ehlers, Wei Tian, CD Batista, ZL Dun, HD Zhou, and Masaaki Matsuda. Static and dynamical properties of the spin-1/2 equilateral triangular-lattice antiferromagnet $Ba_3CoSb_2O_9$. *Physical review letters*, 116(8):087201, 2016. 3, 5, 27, 28, 29

[39] AV Chubukov and DI Golosov. Quantum theory of an antiferromagnet on a triangular lattice in a magnetic field. *Journal of Physics: Condensed Matter*, 3(1):69, 1991. 3, 4

[40] R. S. Gekht and I. N. Bondarenko. Triangular antiferromagnets with a layered structure in a uniform field. *J. Exp. Theor. Phys.*, 84:345, 1997. 3, 5, 17, 28

[41] Ru Chen, Hyejin Ju, Hong-Chen Jiang, Oleg A Starykh, and Leon Balents. Ground states of spin-1/2 triangular antiferromagnets in a magnetic field. *Physical Review B*, 87(16):165123, 2013. 3, 5, 28

[42] Oleg A Starykh, Wen Jin, and Andrey V Chubukov. Phases of a triangular-lattice antiferromagnet near saturation. *Physical Review Letters*, 113(8):087204, 2014. 3, 5, 28

[43] Daisuke Yamamoto, Giacomo Marmorini, and Ippei Danshita. Quantum phase diagram of the triangular-lattice xxz model in a magnetic field. *Physical review letters*, 112(12):127203, 2014. 3, 5, 28, 35

[44] G Koutroulakis, T Zhou, Y Kamiya, JD Thompson, HD Zhou, CD Batista, and SE Brown. Quantum phase diagram of the s= 1 2 triangular-lattice antiferromagnet $Ba_3CoSb_2O_9$. *Physical Review B*, 91(2):024410, 2015. 3, 4, 5, 14, 17, 18, 19, 28, 35

[45] Daisuke Yamamoto, Giacomo Marmorini, and Ippei Danshita. Microscopic model calculations for the magnetization process of layered triangular-lattice quantum antiferromagnets. *Physical review letters*, 114(2):027201, 2015. 3, 5, 17, 28

[46] XZ Liu, O Prokhnenko, D Yamamoto, M Bartkowiak, N Kurita, and H Tanaka. Microscopic evidence of a quantum magnetization process in the s= 1 2 triangular-lattice heisenberg-like antiferromagnet $Ba_3CoSb_2O_9$. *Physical Review B*, 100(9):094436, 2019. 3, 4, 5, 17, 18, 28

[47] C. Wellm, W. Roscher, J. Zeisner, A. Alfonsov, R. Zhong, R. J. Cava, A. Savoyant, R. Hayn, J. van den Brink, B. Büchner, O. Janson, and V. Kataev. Frustration enhanced by kitaev exchange in a $\tilde{j}_{\text{eff}} = \frac{1}{2}$ triangular antiferromagnet. *Phys. Rev. B*, 104:L100420, Sep 2021. 4

[48] Seiji Miyashita. Magnetic properties of ising-like heisenberg antiferromagnets on the triangular lattice. *Journal of the Physical Society of Japan*, 55(10):3605–3617, 1986. 4, 44

[49] Yutaka Shirata, Hidekazu Tanaka, Akira Matsuo, and Koichi Kindo. Experimental realization of a spin-1/2 triangular-lattice heisenberg antiferromagnet. *Physical review letters*, 108(5):057205, 2012. 4, 28

[50] Takuya Susuki, Nobuyuki Kurita, Takuya Tanaka, Hiroyuki Nojiri, Akira Matsuo, Koichi Kindo, and Hidekazu Tanaka. Magnetization process and collective excitations in the s= 1/2 triangular-lattice heisenberg antiferromagnet $Ba_3CoSb_2O_9$. *Physical review letters*, 110(26):267201, 2013. 4, 17, 28, 33

[51] HD Zhou, Cenke Xu, AM Hallas, HJ Silverstein, CR Wiebe, I Umegaki, JQ Yan, TP Murphy, J-H Park, Yiming Qiu, et al. Successive phase transitions and

extended spin-excitation continuum in the s= 1/2 triangular-lattice antiferromagnet $Ba_3CoSb_2O_9$. *Physical review letters*, 109(26):267206, 2012. 4, 27, 28

[52] A Sera, Y Kousaka, Jun Akimitsu, M Sera, T Kawamata, Y Koike, and K Inoue. S= 1 2 triangular-lattice antiferromagnets $Ba_3CoSb_2O_9$ and $CsCuCl_3$: Role of spin-orbit coupling, crystalline electric field effect, and dzyaloshinskii-moriya interaction. *Physical Review B*, 94(21):214408, 2016. 4, 27, 28

[53] G Quirion, M Lapointe-Major, M Poirier, JA Quilliam, ZL Dun, and HD Zhou. Magnetic phase diagram of $Ba_3CoSb_2O_9$ as determined by ultrasound velocity measurements. *Physical Review B*, 92(1):014414, 2015. 4

[54] M Li, A Zelenskiy, JA Quilliam, ZL Dun, HD Zhou, ML Plumer, and G Quirion. Magnetoelastic coupling and the magnetization plateau in $Ba_3CoSb_2O_9$. *Physical Review B*, 99(9):094408, 2019. 4

[55] Y Kamiya, L Ge, Tao Hong, Yiming Qiu, DL Quintero-Castro, Z Lu, HB Cao, M Matsuda, ES Choi, CD Batista, et al. The nature of spin excitations in the one-third magnetization plateau phase of $Ba_3CoSb_2O_9$. *Nature communications*, 9(1):1–11, 2018. 4, 5, 28

[56] David Macdougal, Stephanie Williams, Dharmalingam Prabhakaran, Robert I Bewley, David J Voneshen, and Radu Coldea. Avoided quasiparticle decay and enhanced excitation continuum in the spin-1 2 near-heisenberg triangular antiferromagnet ba 3 cosb 2 o 9. *Phys. Rev. B*, 102(6):064421, 2020. 5, 28, 29

[57] Saya Ito, Nobuyuki Kurita, Hidekazu Tanaka, Seiko Ohira-Kawamura, Kenji Nakajima, Shinichi Itoh, Keitaro Kuwahara, and Kazuhisa Kakurai. Structure of the magnetic excitations in the spin-1/2 triangular-lattice heisenberg antiferromagnet $Ba_3CoSb_2O_9$. *Nature communications*, 8(1):1–6, 2017. 5, 28, 29

[58] Ruben Verresen, Roderich Moessner, and Frank Pollmann. Avoided quasiparticle decay from strong quantum interactions. *Nature Physics*, 15(8):750–753, 2019. 5, 28, 29

[59] M Mourigal, WT Fuhrman, AL Chernyshev, and ME Zhitomirsky. Dynamical structure factor of the triangular-lattice antiferromagnet. *Physical Review B*, 88(9):094407, 2013. 5

[60] Esteban Agustín Ghioldi, Alejandro Mezio, Luis Oscar Manuel, RRP Singh, J Oitmaa, and Adolfo Emilio Trumper. Magnons and excitation continuum in xxz triangular antiferromagnetic model: Application to $Ba_3CoSb_2O_9$. *Physical Review B*, 91(13):134423, 2015. 5

[61] PA Maksimov, ME Zhitomirsky, and AL Chernyshev. Field-induced decays in xxz triangular-lattice antiferromagnets. *Physical Review B*, 94(14):140407, 2016. 5, 18

[62] M Lee, J Hwang, ES Choi, J Ma, CR Dela Cruz, M Zhu, X Ke, ZL Dun, and HD Zhou. Series of phase transitions and multiferroicity in the quasi-two-dimensional spin-1 2 triangular-lattice antiferromagnet ba 3 conb 2 o 9. *Physical Review B*, 89(10):104420, 2014. 6, 30, 32, 33, 35, 36, 45, 47

[63] M Lee, ES Choi, J Ma, R Sinclair, CR Dela Cruz, and HD Zhou. Magnetic and electric properties of triangular lattice antiferromagnets ba3ata2o9 (a= ni and co). *Materials Research Bulletin*, 88:308–314, 2017. 6

[64] Kazuya Yokota, Nobuyuki Kurita, and Hidekazu Tanaka. Magnetic phase diagram of the s= 1 2 triangular-lattice heisenberg antiferromagnet ba 3 co nb 2 o 9. *Phys. Rev. B*, 90(1):014403, 2014. 6, 45

[65] Z Lu, L Ge, G Wang, M Russina, G Günther, CR dela Cruz, R Sinclair, HD Zhou, and J Ma. Lattice distortion effects on the frustrated spin-1 triangular-antiferromagnet a 3 nin b 2 o 9 (a= ba, sr, and ca). *Physical Review B*, 98(9):094412, 2018. 6, 27, 31, 32

[66] Vicent Primo-Martin and Martin Jansen. Synthesis, structure, and physical properties of cobalt perovskites: Sr3cosb2o9 and sr2cosbo6- δ. *Journal of Solid State Chemistry*, 157(1):76–85, 2001. 6

[67] Kullaiah Byrappa. *Crystal growth technology*. Springer Science & Business Media, 2003. 7

[68] George M Sheldrick. Crystal structure refinement with shelxl. *Acta Crystallographica Section C: Structural Chemistry*, 71(1):3–8, 2015. 8

[69] ST Hannahs and NA Fortune. Heat capacity cell for angular measurements in high magnetic fields. *Physica B: Condensed Matter*, 329:1586–1587, 2003. 9

[70] Nathanael Alexander Fortune and Scott T Hannahs. Top-loading small-sample calorimeters for measurements as a function of magnetic field angle. *J. Phys. Conf. Ser*, 568:032008, 2014. 9

[71] Nathanael Fortune, Gayle Gossett, Lydia Peabody, Katherine Lehe, S Uji, and Hayuyoshi Aoki. High magnetic field corrections to resistance thermometers for low temperature calorimetry. *Review of Scientific Instruments*, 71(10):3825–3830, 2000. 9

[72] X Rao, X Zhao, X-Y Wang, HL Che, LG Chu, G Hussain, T-L Xia, and XF Sun. Quantum oscillation of thermal conductivity and violation of weidemann-franz law in taas _2 and nbas _2. *arXiv preprint arXiv:1906.03961*, 2019. 11

[73] J Takeya, Yoichi Ando, Seiki Komiya, and XF Sun. Low-temperature electronic heat transport in la 2- x sr x cuo 4 single crystals: Unusual low-energy physics in the normal and superconducting states. *Physical review letters*, 88(7):077001, 2002. 11

[74] XF Sun, Kouji Segawa, and Yoichi Ando. Metal-to-insulator crossover in y b a 2 c u 3 o y probed by low-temperature quasiparticle heat transport. *Physical review letters*, 93(10):107001, 2004. 11

[75] Yoichi Ando, S Ono, XF Sun, J Takeya, FF Balakirev, JB Betts, and GS Boebinger. Quantum phase transitions in the cuprate superconductor bi 2 sr 2- x la x cuo 6+ δ. *Physical review letters*, 92(24):247004, 2004. 11

[76] XF Sun, S Ono, Yasushi Abe, Seiki Komiya, Kouji Segawa, and Yoichi Ando. Electronic inhomogeneity and breakdown of the universal thermal conductivity of cuprate superconductors. *Physical review letters*, 96(1):017008, 2006. 11

[77] XF Sun, I Tsukada, T Suzuki, Seiki Komiya, and Yoichi Ando. Large magnetothermal effect and spin-phonon coupling in a parent insulating cuprate pr 1.3 la 0.7 cuo 4. *Physical Review B*, 72(10):104501, 2005. 11

[78] XF Sun, Seiki Komiya, J Takeya, and Yoichi Ando. Magnetic-field-induced localization of quasiparticles in underdoped l a 2- x s r x c u o 4 single crystals. *Physical review letters*, 90(11):117004, 2003. 11

[79] CC Gu, ZY Zhao, XL Chen, M Lee, ES Choi, YY Han, LS Ling, L Pi, YH Zhang, G Chen, et al. Field-driven quantum criticality in the spinel magnet zncr 2 se 4. *Physical Review Letters*, 120(14):147204, 2018. 11

[80] Shi-Peng Shen, Jia-Chuan Wu, Jun-Da Song, Xue-Feng Sun, Yi-Feng Yang, Yi-Sheng Chai, Da-Shan Shang, Shou-Guo Wang, James F Scott, and Young Sun. Quantum electric-dipole liquid on a triangular lattice. *Nature communications*, 7(1):1–6, 2016. 11

[81] ZY Zhao, B Tong, X Zhao, LM Chen, J Shi, FB Zhang, JD Song, SJ Li, JC Wu, HS Xu, et al. Thermal conductivity of ipa-cucl 3: evidence for ballistic magnon transport and the limited applicability of the bose-einstein condensation model. *Physical Review B*, 91(13):134420, 2015. 11

[82] HD Zhou, ZY Zhao, XF Sun, M Nieto Suarez, Beatriz Rivas-Murias, Vladimir Tsurkan, Joachim Deisenhofer, VS Zapf, and Francisco Rivadulla. Low-temperature spin excitations in frustrated zncr 2 o 4 probed by high-field thermal conductivity. *Physical Review B*, 87(17):174436, 2013. 11

[83] Huibo Cao, Bryan C Chakoumakos, Katie M Andrews, Yan Wu, Richard A Riedel, Jason Hodges, Wenduo Zhou, Ray Gregory, Bianca Haberl, Jamie Molaison, et al. Demand, a dimensional extreme magnetic neutron diffractometer at the high flux isotope reactor. *Crystals*, 9(1):5, 2019. 12

[84] Juan Rodríguez-Carvajal. Recent advances in magnetic structure determination by neutron powder diffraction. *Physica B: Condensed Matter*, 192(1-2):55–69, 1993. 12

[85] JA Rodriguez, DM Adler, PC Brand, C Broholm, JC Cook, C Brocker, R Hammond, Z Huang, P Hundertmark, JW Lynn, et al. Macs—a new high intensity cold neutron spectrometer at nist. *Measurement Science and Technology*, 19(3):034023, 2008. 13

[86] K Naruse, T Kawamata, M Ohno, Y Matsuoka, H Sudo, H Nagasawa, Y Hagiya, T Sasaki, and Y Koike. Thermal conductivity in the triangular-lattice antiferromagnet $Ba_3CoSb_2O_9$. In *Journal of Physics: Conference Series*, volume 568, page 042014. IOP Publishing, 2014. 15

[87] L Bevaart, E Frikkee, and LJ de Jongh. Neutron-scattering study of magnetic-field-induced transitions in a two-component antiferromagnetic system with competing spin anisotropies. *Physical Review B*, 19(9):4741, 1979. 18

[88] H Rohrer and Ch Gerber. Bicritical and tetracritical behavior of $GdAlO_3$. *Physical Review Letters*, 38(16):909, 1977. 18

[89] Tsuneaki Goto, Toshiya Inami, and Yoshitami Ajiro. New tetracritical behavior in $CsMnBr_3$. *Journal of the Physical Society of Japan*, 59(7):2328–2331, 1990. 18

[90] Yuesheng Li, Gang Chen, Wei Tong, Li Pi, Juanjuan Liu, Zhaorong Yang, Xiaoqun Wang, and Qingming Zhang. Rare-earth triangular lattice spin liquid: a single-crystal study of ybmggao 4. *Phys. Rev. Lett.*, 115(16):167203, 2015. 21

[91] Yuesheng Li, Devashibhai Adroja, Robert I Bewley, David Voneshen, Alexander A Tsirlin, Philipp Gegenwart, and Qingming Zhang. Crystalline electric-field randomness in the triangular lattice spin-liquid ybmggao 4. *Phys. Rev. Lett.*, 118(10):107202, 2017. 21

[92] Qiang Luo, Shijie Hu, Bin Xi, Jize Zhao, and Xiaoqun Wang. Ground-state phase diagram of an anisotropic spin-1 2 model on the triangular lattice. *Phys. Rev. B*, 95(16):165110, 2017. 21

[93] Itamar Kimchi, Adam Nahum, and T Senthil. Valence bonds in random quantum magnets: Theory and application to ybmggao 4. *Phys. Rev. X*, 8(3):031028, 2018. 21

[94] Edward Parker and Leon Balents. Finite-temperature behavior of a classical spin-orbit-coupled model for ybmggao 4 with and without bond disorder. *Phys. Rev. B*, 97(18):184413, 2018. 21

[95] Hikaru Kawamura and Kazuki Uematsu. Nature of the randomness-induced quantum spin liquids in two dimensions. *J. Phys.: Condens. Matter*, 31(50):504003, 2019. 21

[96] Zhenyue Zhu, PA Maksimov, Steven R White, and AL Chernyshev. Disorder-induced mimicry of a spin liquid in ybmggao 4. *Phys. Rev. Lett.*, 119(15):157201, 2017. 21

[97] Zhenyue Zhu, PA Maksimov, Steven R White, and AL Chernyshev. Topography of spin liquids on a triangular lattice. *Phys. Rev. Lett.*, 120(20):207203, 2018. 21

[98] Han-Qing Wu, Shou-Shu Gong, and DN Sheng. Randomness-induced spin-liquid-like phase in the spin-1 2 j 1- j 2 triangular heisenberg model. *Phys. Rev. B*, 99(8):085141, 2019. 22

[99] Ryui Kaneko, Satoshi Morita, and Masatoshi Imada. Gapless spin-liquid phase in an extended spin 1/2 triangular heisenberg model. *J. Phys. Soc. Jpn.*, 83(9):093707, 2014. 22

[100] Peggy HY Li, Raymond F Bishop, and Charles E Campbell. Quasiclassical magnetic order and its loss in a spin-1 2 heisenberg antiferromagnet on a triangular lattice with competing bonds. *Phys. Rev. B*, 91(1):014426, 2015. 22

[101] Zhenyue Zhu and Steven R White. Spin liquid phase of the s= 1 2 j 1- j 2 heisenberg model on the triangular lattice. *Phys. Rev. B*, 92(4):041105, 2015. 22

[102] Wen-Jun Hu, Shou-Shu Gong, Wei Zhu, and DN Sheng. Competing spin-liquid states in the spin-1 2 heisenberg model on the triangular lattice. *Phys. Rev. B*, 92(14):140403, 2015. 22

[103] Yasir Iqbal, Wen-Jun Hu, Ronny Thomale, Didier Poilblanc, and Federico Becca. Spin liquid nature in the heisenberg j 1- j 2 triangular antiferromagnet. *Phys. Rev. B*, 93(14):144411, 2016. 22

[104] SN Saadatmand and IP McCulloch. Symmetry fractionalization in the topological phase of the spin-1 2 j 1- j 2 triangular heisenberg model. *Phys. Rev. B*, 94(12):121111, 2016. 22

[105] Itamar Kimchi, John P Sheckelton, Tyrel M McQueen, and Patrick A Lee. Scaling and data collapse from local moments in frustrated disordered quantum spin systems. *Nature communications*, 9(1):1–5, 2018. 22

[106] Pavel A Volkov, Choong-Jae Won, DI Gorbunov, Jaewook Kim, Mai Ye, Heung-Sik Kim, JH Pixley, Sang-Wook Cheong, and G Blumberg. Random singlet state in ba 5 cuir 3 o 12 single crystals. *Phys. Rev. B*, 101(2):020406, 2020. 22

[107] S Kundu, Akmal Hossain, Ranjan Das, M Baenitz, Peter J Baker, Jean-Christophe Orain, DC Joshi, Roland Mathieu, Priya Mahadevan, Sumiran Pujari, et al. Signatures of a spin-1 2 cooperative paramagnet in the diluted triangular lattice of y 2 cutio 6. *Phys. Rev. Lett.*, 125(11):117206, 2020. 22

[108] Pengbo Song, Kejia Zhu, Fan Yang, Yuan Wei, Lu Zhang, Huaixin Yang, Xian-Lei Sheng, Yang Qi, Jiamin Ni, Shiyan Li, et al. Evidences for the random singlet phase in a new honeycomb iridate srir _2 o _6. *arXiv preprint arXiv:2103.05820*, 2021. 22

[109] SV Syzranov and AP Ramirez. Hidden energy scale in geometrically frustrated systems: are quantum spin liquids achievable? *arXiv preprint arXiv:2105.08070*, 2021. 22

[110] Lu Liu, Hui Shao, Yu-Cheng Lin, Wenan Guo, and Anders W Sandvik. Random-singlet phase in disordered two-dimensional quantum magnets. *Phys. Rev. X*, 8(4):041040, 2018. 22

[111] Wenshan Hong, Lu Liu, Chang Liu, Xiaoyan Ma, Akihiro Koda, Xin Li, Jianming Song, Wenyun Yang, Jinbo Yang, Peng Cheng, et al. Extreme suppression of antiferromagnetic order and critical scaling in a two-dimensional random quantum magnet. *Phys. Rev. Lett.*, 126(3):037201, 2021. 22

[112] Seung-Ho Baek, Hyeon Woo Yeo, Seung-Hwan Do, Kwang-Yong Choi, Lukas Janssen, Matthias Vojta, and Bernd Büchner. Observation of a random singlet state in a diluted kitaev honeycomb material. *Phys. Rev. B*, 102(9):094407, 2020. 22

[113] Seung-Hwan Do, CH Lee, T Kihara, YS Choi, Sungwon Yoon, Kangwon Kim, Hyeonsik Cheong, Wei-Tin Chen, Fangcheng Chou, H Nojiri, et al. Randomly hopping majorana fermions in the diluted kitaev system α-ru 0.8 ir 0.2 cl 3. *Phys. Rev. Lett.*, 124(4):047204, 2020. 22

[114] YY Huang, Y Xu, Le Wang, CC Zhao, CP Tu, JM Ni, LS Wang, BL Pan, Ying Fu, Zhanyang Hao, et al. Heat transport in herbertsmithite: Can a quantum spin liquid survive disorder? *arXiv preprint arXiv:2105.14749*, 2021. 22

[115] Xiao Hu, Daniel M Pajerowski, Depei Zhang, Andrey A Podlesnyak, Yiming Qiu, Qing Huang, Haidong Zhou, Israel Klich, Alexander I Kolesnikov, Matthew B Stone, et al. Freezing of a disorder induced spin liquid with strong quantum fluctuations. *Phys. Rev. Lett.*, 127(1):017201, 2021. 22

[116] Huan-Da Ren, Tian-Yu Xiong, Han-Qing Wu, DN Sheng, and Shou-Shu Gong. Characterizing random-singlet state in two-dimensional frustrated quantum magnets and implications for the double perovskite sr _2 cute _{1 − x} w _{x} o _6. *arXiv preprint arXiv:2004.02128*, 2020. 22

[117] SJ Gomez, PM Sarte, M Zelensky, AM Hallas, BA Gonzalez, KH Hong, EJ Pace, S Calder, MB Stone, Y Su, et al. Absence of moment fragmentation in the mixed b-site pyrochlore nd 2 gasbo 7. *Phys. Rev. B*, 103(21):214419, 2021. 22

[118] Tokuro Shimokawa, Ken Watanabe, and Hikaru Kawamura. Static and dynamical spin correlations of the s= 1 2 random-bond antiferromagnetic heisenberg model on the triangular and kagome lattices. *Phys. Rev. B*, 92(13):134407, 2015. 22

[119] Hikaru Kawamura, Ken Watanabe, and Tokuro Shimokawa. Quantum spin-liquid behavior in the spin-1/2 random-bond heisenberg antiferromagnet on the kagome lattice. *J. Phys. Soc. Jpn.*, 83(10):103704, 2014. 22

[120] Ken Watanabe, Hikaru Kawamura, Hiroki Nakano, and Toru Sakai. Quantum spin-liquid behavior in the spin-1/2 random heisenberg antiferromagnet on the triangular lattice. *J. Phys. Soc. Jpn.*, 83(3):034714, 2014. 22

[121] Kazuki Uematsu and Hikaru Kawamura. Randomness-induced quantum spin liquid behavior in the s= 1/2 random j 1–j 2 heisenberg antiferromagnet on the honeycomb lattice. *J. Phys. Soc. Jpn.*, 86(4):044704, 2017. 22

[122] Kazuki Uematsu and Hikaru Kawamura. Randomness-induced quantum spin liquid behavior in the s= 1 2 random j 1- j 2 heisenberg antiferromagnet on the square lattice. *Phys. Rev. B*, 98(13):134427, 2018. 22

[123] Kazuki Uematsu and Hikaru Kawamura. Randomness-induced quantum spin liquid behavior in the s= 1/2 random-bond heisenberg antiferromagnet on the pyrochlore lattice. *Phys. Rev. Lett.*, 123(8):087201, 2019. 22

[124] AI Smirnov, TA Soldatov, OA Petrenko, A Takata, T Kida, M Hagiwara, A Ya Shapiro, and ME Zhitomirsky. Order by quenched disorder in the model triangular antiferromagnet rbfe (moo 4) 2. *Phys. Rev. Lett.*, 119(4):047204, 2017. 28

[125] T Kimura, T Goto, H Shintani, K Ishizaka, T-h Arima, and Y Tokura. Magnetic control of ferroelectric polarization. *nature*, 426(6962):55–58, 2003. 30

[126] Nicola A Spaldin and Manfred Fiebig. The renaissance of magnetoelectric multiferroics. *Science*, 309(5733):391–392, 2005. 30

[127] Manfred Fiebig. Revival of the magnetoelectric effect. *Journal of physics D: applied physics*, 38(8):R123, 2005. 30

[128] Yoshinori Tokura. Multiferroics as quantum electromagnets. *Science*, 312(5779):1481–1482, 2006. 30

[129] Sang-Wook Cheong and Maxim Mostovoy. Multiferroics: a magnetic twist for ferroelectricity. *Nature materials*, 6(1):13–20, 2007. 30

[130] KF Wang, J-M Liu, and ZF Ren. Multiferroicity: the coupling between magnetic and polarization orders. *Advances in Physics*, 58(4):321–448, 2009. 30

[131] Hosho Katsura, Naoto Nagaosa, and Alexander V Balatsky. Spin current and magnetoelectric effect in noncollinear magnets. *Physical review letters*, 95(5):057205, 2005. 30

[132] Taka-hisa Arima. Ferroelectricity induced by proper-screw type magnetic order. *Journal of the Physical Society of Japan*, 76(7):073702–073702, 2007. 30

[133] Chenglong Jia, Shigeki Onoda, Naoto Nagaosa, and Jung Hoon Han. Microscopic theory of spin-polarization coupling in multiferroic transition metal oxides. *Physical Review B*, 76(14):144424, 2007. 30

[134] Maxim Mostovoy. Ferroelectricity in spiral magnets. *Physical review letters*, 96(6):067601, 2006. 30

[135] Alexander J Hearmon, Federica Fabrizi, Laurent C Chapon, RD Johnson, Dharmalingam Prabhakaran, Sergey V Streltsov, PJ Brown, and Paolo G Radaelli. Electric field control of the magnetic chiralities in ferroaxial multiferroic rbfe (moo 4) 2. *Physical review letters*, 108(23):237201, 2012. 30

[136] H Mitamura, R Watanuki, Koji Kaneko, N Onozaki, Y Amou, S Kittaka, Riki Kobayashi, Y Shimura, I Yamamoto, K Suzuki, et al. Spin-chirality-driven ferroelectricity on a perfect triangular lattice antiferromagnet. *Physical review letters*, 113(14):147202, 2014. 30

[137] J Hwang, ES Choi, F Ye, CR Dela Cruz, Y Xin, HD Zhou, and P Schlottmann. Successive magnetic phase transitions and multiferroicity in the spin-one triangular-lattice antiferromagnet ba 3 ninb 2 o 9. *Physical review letters*, 109(25):257205, 2012. 30, 36, 47

[138] Jia Dai, Ping Zhou, Peng-Shuai Wang, Fei Pang, T J Munsie, Graeme M Luke, Jin-Shan Zhang, and Weiqiang Yu. Spin frustration and magnetic ordering in triangular

lattice antiferromagnet ca _3 conb _2 o _9. *arXiv preprint arXiv:1512.07792*, 2015. 31, 34

[139] Valeska Ting, Yun Liu, Lasse Norén, RL Withers, DJ Goossens, Michael James, and C Ferraris. A structure, conductivity and dielectric properties investigation of a3conb2o9 (a= ca2+, sr2+, ba2+) triple perovskites. *Journal of Solid State Chemistry*, 177(12):4428–4442, 2004. 31

[140] Shinichiro Seki, Yoshinori Onose, and Yoshinori Tokura. Spin-driven ferroelectricity in triangular lattice antiferromagnets a cro 2 (a= cu, ag, li, or na). *Physical review letters*, 101(6):067204, 2008. 35

[141] Luis Seabra, Tsutomu Momoi, Philippe Sindzingre, and Nic Shannon. Phase diagram of the classical heisenberg antiferromagnet on a triangular lattice in an applied magnetic field. *Physical Review B*, 84(21):214418, 2011. 35

[142] M Lee, ES Choi, X Huang, J Ma, CR Dela Cruz, M Matsuda, W Tian, ZL Dun, S Dong, and HD Zhou. Magnetic phase diagram and multiferroicity of ba 3 mnnb 2 o 9: A spin-5 2 triangular lattice antiferromagnet with weak easy-axis anisotropy. *Physical Review B*, 90(22):224402, 2014. 36

[143] AI Smirnov, H Yashiro, S Kimura, M Hagiwara, Y Narumi, K Kindo, A Kikkawa, K Katsumata, A Ya Shapiro, and LN Demianets. Triangular lattice antiferromagnet $RbFe(MoO_4)_2$ in high magnetic fields. *Physical Review B*, 75(13):134412, 2007. 36, 37

[144] LE Svistov, AI Smirnov, LA Prozorova, OA Petrenko, A Micheler, N Büttgen, A Ya Shapiro, and LN Demianets. Magnetic phase diagram, critical behavior, and two-dimensional to three-dimensional crossover in the triangular lattice antiferromagnet $RbFe(MoO_4)_2$. *Physical Review B*, 74(2):024412, 2006. 36

[145] M.F. Collins and O. A Petrenko. Triangular antiferromagnets. *Canadian Journal of Physics*, 75:605, 1997. 37

[146] RH Clark and WG Moulton. Cs 133 and cl 35 nmr in antiferromagnetic csni cl 3. *Physical Review B*, 5(3):788, 1972. 37

[147] Satoru Maegawa, Toshiro Kohmoto, Takao Goto, and Naoki Fujiwara. Magnetic structures of successively ordered phases in a triangular-lattice antiferromagnet csnibr 3. *Physical Review B*, 44(22):12617, 1991. 37

[148] Hiroaki Kadowaki, Toshiya Inami, Yoshitami Ajiro, Kenji Nakajima, and Yasuo Endoh. Universality class of magnetic phase transition in the triangular lattice antiferromagnet csmni3. *Journal of the Physical Society of Japan*, 60(5):1708–1720, 1991. 37

[149] BD Gaulin, TE Mason, MF Collins, and JZ Larese. Tetracritical behavior of csmnbr 3. *Physical review letters*, 62(12):1380, 1989. 37

[150] Ruidan Zhong, Shu Guo, Guangyong Xu, Zhijun Xu, and Robert J Cava. Strong quantum fluctuations in a quantum spin liquid candidate with a co-based triangular lattice. *Proceedings of the National Academy of Sciences*, 116(29):14505–14510, 2019. 38, 41

[151] Daiki Watanabe, Kaori Sugii, Masaaki Shimozawa, Yoshitaka Suzuki, Takeshi Yajima, Hajime Ishikawa, Zenji Hiroi, Takasada Shibauchi, Yuji Matsuda, and Minoru Yamashita. Emergence of nontrivial magnetic excitations in a spin-liquid state of kagomé volborthite. *Proceedings of the National Academy of Sciences*, 113(31):8653–8657, 2016. 41

[152] Li Ern Chern, Kyusung Hwang, Tomonari Mizoguchi, Yejin Huh, and Yong Baek Kim. Quantum spin liquid and magnetic order in a two-dimensional nonsymmorphic lattice: considering the distorted kagome lattice of volborthite. *Physical Review B*, 96(3):035118, 2017. 41

[153] Li Ern Chern, Robert Schaffer, Sopheak Sorn, and Yong Baek Kim. Fermionic spin liquid analysis of the paramagnetic state in volborthite. *Physical Review B*, 96(16):165117, 2017. 41

[154] Yukio Yasui, Minoru Soda, Satoshi Iikubo, Masafumi Ito, Masatoshi Sato, Nobuko Hamaguchi, Taku Matsushita, Nobuo Wada, Tetsuya Takeuchi, Naofumi Aso, et al.

Ferromagnetic transition of pyrochlore compound yb2ti2o7. *Journal of the Physical Society of Japan*, 72(11):3014–3015, 2003. 41

[155] Kate A Ross, Lucile Savary, Bruce D Gaulin, and Leon Balents. Quantum excitations in quantum spin ice. *Physical Review X*, 1(2):021002, 2011. 41

[156] JA Hodges, Pierre Bonville, Anne Forget, M Rams, Krzysztof Królas, and G Dhalenne. The crystal field and exchange interactions in yb2ti2o7. *Journal of Physics: Condensed Matter*, 13(41):9301, 2001. 41

[157] A Scheie, J Kindervater, S Säubert, C Duvinage, C Pfleiderer, HJ Changlani, S Zhang, Leland Harriger, K Arpino, SM Koohpayeh, et al. Reentrant phase diagram of yb 2 ti 2 o 7 in a¡ 111¿ magnetic field. *Physical review letters*, 119(12):127201, 2017. 41

[158] KE Arpino, BA Trump, AO Scheie, TM McQueen, and SM Koohpayeh. Impact of stoichiometry of yb 2 ti 2 o 7 on its physical properties. *Physical Review B*, 95(9):094407, 2017. 41

[159] Lieh-Jeng Chang, Shigeki Onoda, Yixi Su, Ying-Jer Kao, Ku-Ding Tsuei, Yukio Yasui, Kazuhisa Kakurai, and Martin Richard Lees. Higgs transition from a magnetic coulomb liquid to a ferromagnet in yb2ti2o7. *Nature communications*, 3(1):1–7, 2012. 42

[160] Y Tokiwa, T Yamashita, M Udagawa, S Kittaka, T Sakakibara, D Terazawa, Y Shimoyama, T Terashima, Y Yasui, T Shibauchi, et al. Possible observation of highly itinerant quantum magnetic monopoles in the frustrated pyrochlore yb2ti2o7. *Nature communications*, 7(1):1–6, 2016. 42

[161] Max Hirschberger, Peter Czajka, SM Koohpayeh, Wudi Wang, and N Phuan Ong. Enhanced thermal hall conductivity below 1 kelvin in the pyrochlore magnet yb _2 ti _2 o _7. *arXiv preprint arXiv:1903.00595*, 2019. 42

[162] Yuki Kojima, Masari Watanabe, Nobuyuki Kurita, Hidekazu Tanaka, Akira Matsuo, Koichi Kindo, and Maxim Avdeev. Quantum magnetic properties of the spin-1 2 triangular-lattice antiferromagnet ba 2 la 2 cote 2 o 12. *Physical Review B*, 98(17):174406, 2018. 45

List of Publications

First-Author Publications

1. N. Li, **Q. Huang**, A. Brassington, X. Yue, W. Chu, S. Guang, X. Zhou, P. Gao, E. X. Feng, H. B. Cao, E. S. Choi, Y. Sun, Q. J. Li, X. Zhao, H. D. Zhou, X. F. Sun (2021). "Quantum spin state transitions in spin-1 equilateral triangular lattice antiferromagnet Na2BaNi(PO4)2." Physical Review B 104, 104403.

   Co-first author

2. X. Rao, G. Hussain, **Q. Huang**, W. J. Chu, N. Li, X. Zhao, Z. Dun, E. S. Choi, T. Asaba, L. Chen, L. Li, X. Y. Yue, N. N. Wang, J.-G. Cheng, Y. H. Gao, Y. Shen, J. Zhao, G. Chen, H. D. Zhou and X. F. Sun (2021), "Survival of itinerant excitations and quantum spin state transitions in YbMgGaO4 with chemical disorder." Nature Communications 12, 4949.

   Co-first author

3. N. Li, **Q. Huang**, X. Y. Yue, W. J. Chu, Q. Chen, E. S. Choi, X. Zhao, H. D. Zhou and X. F. Sun (2020). "Possible itinerant excitations and quantum spin state transitions in the effective spin-1/2 triangular-lattice antiferromagnet Na2BaCo(PO4)2." Nature Communications 11, 4216.

   Co-first author

4. **Q. Huang**, R. Rawl, W. W. Xie, E. S. Chou, V. S. Zapf, X. X. Ding, C. Mauws, C. R. Wiebe, E. X. Feng, H. B. Cao, W. Tian, J. Ma, Y. Qiu, N. Butch, H. D. Zhou

(2021). "Non-magnetic ion site disorder effects on the quantum magnetism of a spin-1/2 equilateral triangular lattice antiferromagnet." arXiv: 2108.08893. Accepted by Journal of Physics-Condensed Matter

Collaborative Publications

1. M. Chen, J. Wu, **Q. Huang**, J. Jiao, Z. Dun, G. Wang, Z. Chen, G. Lin, V. Rathinam, C. Li, Y. Pei, F. Ye, H. D. Zhou and J. Ma (2021). "The Transport Properties of Quasi–One-Dimensional Ba3Co2O6(CO3)0.7" Frontiers in Physics 9, 785801.

2. G. Lin, J. Jeong, C. Kim, Y. Wang, **Q. Huang**, T. Masuda, S. Asai, S. Itoh, G. Günther, M. Russina, Zh. Lu, J. Sheng, L. Wang, J. Wang, G. Wang, Q. Ren, C. Xi, W. Tong, L. Ling, Z. Liu, L. Wu, J. Mei, Z. Qu, H. D. Zhou, J. Park, Y. Wan, J. Ma (2021). "Field-induced quantum spin disordered state in spin-1/2 honeycomb magnet Na2Co2TeO6 with small Kitaev interaction." Nature communications 12, 5559.

3. Mauws, C., N. Hiebert, M. L. Rutherford, H. D. Zhou, **Q. Huang**, M. B. Stone, N. P. Butch, Y. Su, E. S. Choi, Z. Yamani and C. R. Wiebe (2021). "Magnetic ordering in the Ising antiferromagnetic pyrochlore Nd2ScNbO7." Journal of Physics-Condensed Matter 33, 245802.

4. Jiao, J. L., H. P. Zhang, **Q. Huang**, W. Wang, R. Sinclair, G. Wang, Q. Ren, G. T. Lin, A. Huq, H. D. Zhou, M. Z. Li and J. Ma (2021). "Orbital competition of Mn3+ and V3+ ions in Mn1+xV2-xO4." Journal of Physics-Condensed Matter 33, 134002.

5. Hu, X., D. M. Pajerowski, D. P. Zhang, A. A. Podlesnyak, Y. M. Qiu, **Q. Huang**, H. D. Zhou, I. Klich, A. I. Kolesnikov, M. B. Stone and S. H. Lee (2021). "Freezing of a Disorder Induced Spin Liquid with Strong Quantum Fluctuations." Physical Review Letters 127, 017201.

6. Fortune, N. A., **Q. Huang**, T. Hong, J. Ma, E. S. Choi, S. T. Hannahs, Z. Y. Zhao, X. F. Sun, Y. Takano and H. D. Zhou (2021). "Evolution of magnetic field induced ordering in the layered quantum Heisenberg triangular-lattice antiferromagnet Ba3CoSb2O9." Physical Review B 103, 184425.

7. Dun, Z. L., M. Daum, R. Baral, H. E. Fischer, H. B. Cao, Y. H. Liu, M. B. Stone, J. A. Rodriguez-Rivera, E. S. Choi, **Q. Huang**, H. D. Zhou, M. Mourigal and B. A. Frandsen (2021). "Neutron scattering investigation of proposed Kosterlitz-Thouless transitions in the triangularlattice Ising antiferromagnet TmMgGaO4." Physical Review B 103, 064424.

8. Bai, X. J., S. S. Zhang, Z. L. Dun, H. Zhang, **Q. Huang**, H. D. Zhou, M. B. Stone, A. I. Kolesnikov, F. Ye, C. D. Batista and M. Mourigal (2021). "Hybridized quadrupolar excitations in the spin-anisotropic frustrated magnet FeI2." Nature Physics 17, 467-472.

9. Zhang, H., **Q. Huang**, L. Hao, J. Y. Yang, K. Noordhoek, S. Pandey, H. D. Zhou and J. Liu (2020). "Anomalous magnetoresistance in centrosymmetric skyrmion-lattice magnet Gd2PdSi3." New Journal of Physics 22, 083056.

10. Zhang, H., L. Hao, J. Y. Yang, J. Mutch, Z. Y. Liu, **Q. Huang**, K. Noordhoek, A. F. May, J. H. Chu, J. W. Kim, P. J. Ryan, H. D. Zhou and J. Liu (2020). "Comprehensive Electrical Control of Metamagnetic Transition of a Quasi-2D Antiferromagnet by In Situ Anisotropic Strain." Advanced Materials 32, 2002451.

11. Lee, M., Q. Chen, E. S. Choi, **Q. Huang**, Z. Wang, L. S. Ling, Z. Qu, G. H. Wang, J. Ma, A. A. Aczel and H. D. Zhou (2020). "Magnetoelectric effect arising from a field-induced pseudo JahnTeller distortion in a rare-earth magnet." Physical Review Materials 4, 094411.

12. Kinsler-Fedon, C., Q. Zheng, **Q. Huang**, E. S. Choi, J. Q. Yan, H. D. Zhou, D. Mandrus and V. Keppens (2020). "Synthesis, characterization, and single-crystal growth of a high-entropy rare-earth pyrochlore oxide." Physical Review Materials 4, 104411.

13. Jiang, Y., J. Wang, T. Zhao, Z. L. Dun, **Q. Huang**, X. S. Wu, M. Mourigal, H. D. Zhou, W. Pan, M. Ozerov, D. Smirnov and Z. Jiang (2020). "Unraveling the Topological Phase of ZrTe5 via Magnetoinfrared Spectroscopy." Physical Review Letters 125, 046403.

14. Cui, Q., **Q. Huang**, J. A. Alonso, D. Sheptyakov, C. R. De la Cruz, M. T. Fernandez-Diaz, N. N. Wang, Y. Q. Cai, D. Li, X. L. Dong, H. D. Zhou and J. G. Cheng (2020). "Complex antiferromagnetic order in the garnet Co3Al2Si3O12." Physical Review B 101, 144424.

15. Che, H. L., Z. Y. Zhao, X. Rao, L. G. Chu, N. Li, W. J. Chu, P. Gao, X. Y. Yue, Y. Zhou, Q. J. Li, **Q. Huang**, E. Choi, Y. Y. Han, Z. Z. He, H. D. Zhou, X. Zhao and X. F. Sun (2020). "Absence of long-range order in an XY pyrochlore antiferromagnet Er2AlSbO7." Physical Review Materials 4, 054406.

16. Wang, G. H., C. Y. Xu, H. B. Cao, T. Hong, **Q. Huang**, Q. Y. Ren, J. Q. Xu, H. D. Zhou, W. Luo, D. Qian and J. Ma (2019). "Magnetic properties of the low-dimensional BaM2Si2O7 system (M = Cu, Co, Mn)." Physical Review B 100, 035131.

17. Rawl, R., L. Ge, Z. Lu, Z. Evenson, C. R. Dela Cruz, **Q. Huang**, M. Lee, E. S. Choi, M. Mourigal, H. D. Zhou and J. Ma (2019). "Ba8MnNb6O24: A model two-dimensional spin-5/2 triangular lattice antiferromagnet." Physical Review Materials 3, 054412.

18. Chen, L., Z. J. Xiang, C. Tinsman, **Q. Huang**, K. G. Reynolds, H. D. Zhou and L. Li (2019). "Anomalous thermal conductivity across the structural transition in SmBaMn2O6 single crystals." Applied Physics Letters 114, 251904.

19. Xin, Y., **Q. Huang**, Z. Shafieizadeh and H. D. Zhou (2018). "B-site cation order/disorder andtheir valence states in Ba3MnNb2O9 perovskite oxide." Journal of Solid State Chemistry 262, 8-15.

20. Shafieizadeh, Z., Y. Xin, S. M. Koohpayeh, **Q. Huang** and H. D. Zhou (2018). "Superdislocations and point defects in pyrochlore Yb2Ti2O7 single crystals and implication on magnetic ground states." Scientific Reports 8, 17202.

21. Chen, L., Z. J. Xiang, C. Tinsman, T. Asaba, **Q. Huang**, H. D. Zhou and L. Li (2018). "Enhancement of thermal conductivity across the metal-insulator transition in vanadium dioxide." Applied Physics Letters 113, 061902.

Appendix

Table 4.1: Data of crystallographic refinement for Sr-BCSO at 296 (2)K

Crystal system	Hexagonal
F.W. (g/mol)	851.74
Space group;Z	$P6_3/mmc$;2
a(Å)	5.847 (3)
c(Å)	14.507(6)
V($Å^3$)	429.5(4)
Extinction Coefficient	0.00044 (7)
θ range (deg)	2.808-34.487
No. reflections; R_int	8552; 0.0254
No. independent reflections)	394
No. parameters)	24
R_1: ωR_2 ($I < 2\delta(I)$)	0.0104; 0.0190
Goodness of fit	1.199
Diffraction peak and hole (e^-/ $Å^3$)	0.804; -0.800

Table 4.2: Atomic coordinates and equivalent isotropic displacement parameters of Sr-BCSO system.(U_{eq} is defined as one-third of the trace of the orthogonalized U_{ij} tensor ($Å^2$))

Atom	site	Occ.	x	y	z	$U_{(eq)}$
Ba/Sr1	2b	0.952(5)/0.048	0	0	0.25	0.009(1)
Ba/Sr2	4f	0.955(4)/0.045	1/3	2/3	0.0101(1)	
Sb	4f	1	1/3	2/3	0.65183(2)	0.0066(1)
Co	2a	1	0	0	0	0.0057 (1)
O1	6h	1	0.5189(2)	0.0378(2)	0.25	0.0094(4)
O2	12k	1	0.8299(2)	0.6597(3)	0.0848(1)	0.0150(3)

Table 5.1: Structural parameters of CCNO at 300K

Atom	site	x	y	z
Ca1	4e	0.2496(2)	0.4962(3)	0.0661(9)
Ca2	4e	0.7549(2)	0.0057(3)	0.1004(9)
Ca3	4e	0.2548(2)	0.0317(16)	0.2339(11)
Co1	2a	0.0000	0.0000	0.0000
Co1	2d	0.5000	0.5000	0.0000
Nb1	4e	0.5019(14)	0.4872(19)	0.3345(8)
Nb2	4e	-0.0008(7)	-0.0049(20)	0.3394(7)
O1	4e	0.9516(17)	0.7134(21)	0.2473(11)
O2	4e	0.5466(14)	0.7875(21)	0.2851(8)
O3	4e	0.2547(22)	0.5921(18)	0.2626(10)
O4	4e	0.9736(14)	0.7108(20)	0.9254(8)
O5	4e	0.0481(17)	0.2068(20)	0.9168(10)
O6	4e	0.4509(14)	0.3262(17)	0.8867(9)
O7	4e	0.5575(17)	0.8083(19)	0.9469(9)
O8	4e	0.7445(22)	0.0982(19)	0.9101(9)
O9	4e	0.2426(18)	0.5840(19)	0.9270(8)

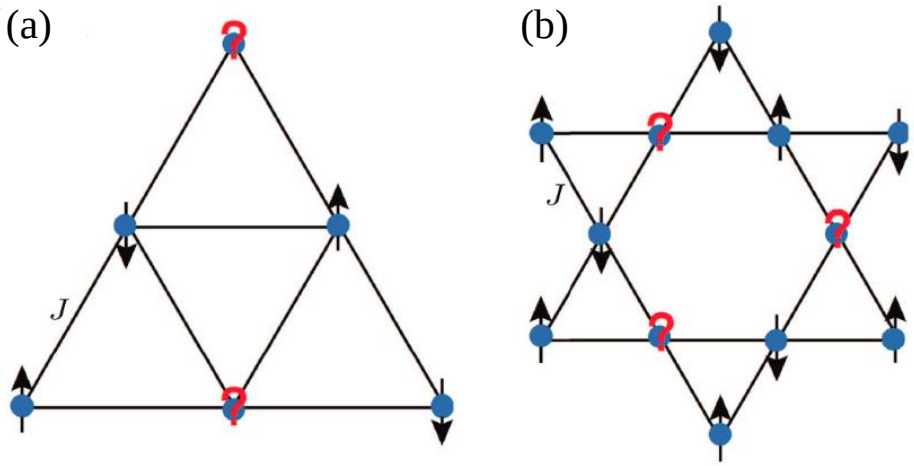

Figure 1.1: The illustration of geometrical frustration in triangular lattice (a) and kagome lattice (b).

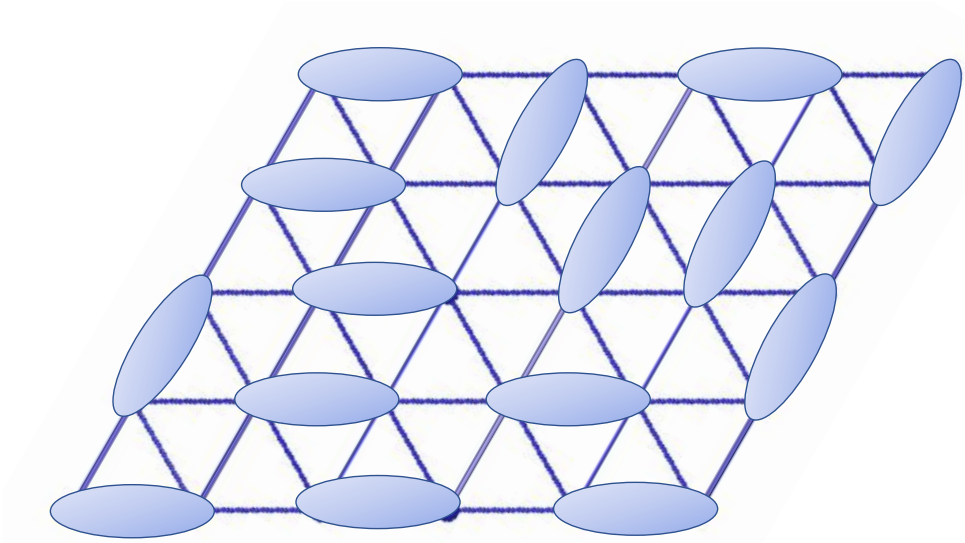

Figure 1.2: The illustration of resonating valence bond state.

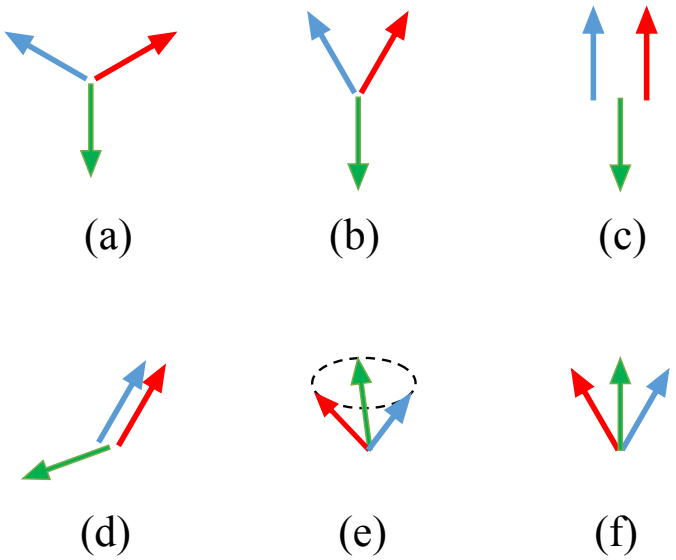

Figure 1.3: Theoretically proposed spin ordering states for the quantum $S = 1/2$ Heisenberg triangular antiferromagnet in the 2D limit. (a-f) are 120-degree, Y, UUD, V, umbrella, and Ψ (fan) phase, respectively. The figures are adopted from [1].

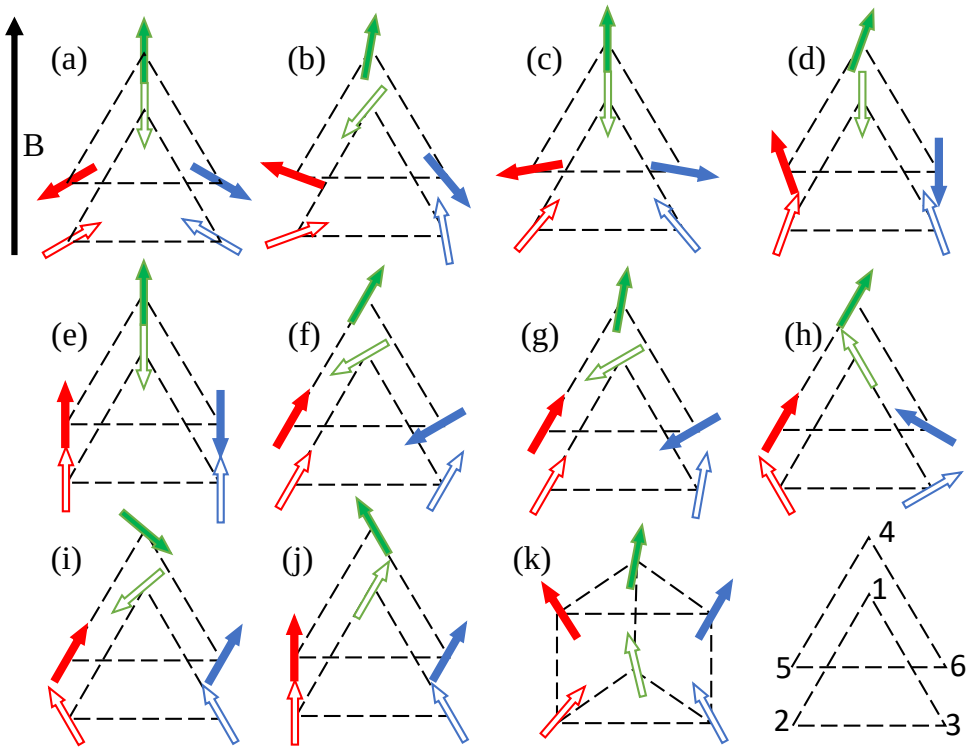

Figure 1.4: Theoretically proposed spin orderings for a quantum $S = 1/2$ Heisenberg triangular antiferromagnet with interlayer coupling in a 2 layer model. Spins 1 - 3 correspond to layer 1; spins 4 - 6 to layer 2. The orderings are named as follows: (a) the zero field 120° structure, (b) distorted combined Y ,(c) alternating ordered Y, (d) parallel ordered Y, (e) UUD, (f) V, (g) distorted V, (h) V′, (i) staggered V′, (j) ψ (fan) spin structure. Ordering (k) corresponds to the classically expected cone (umbrella) phase. The figures are adopted from [1].

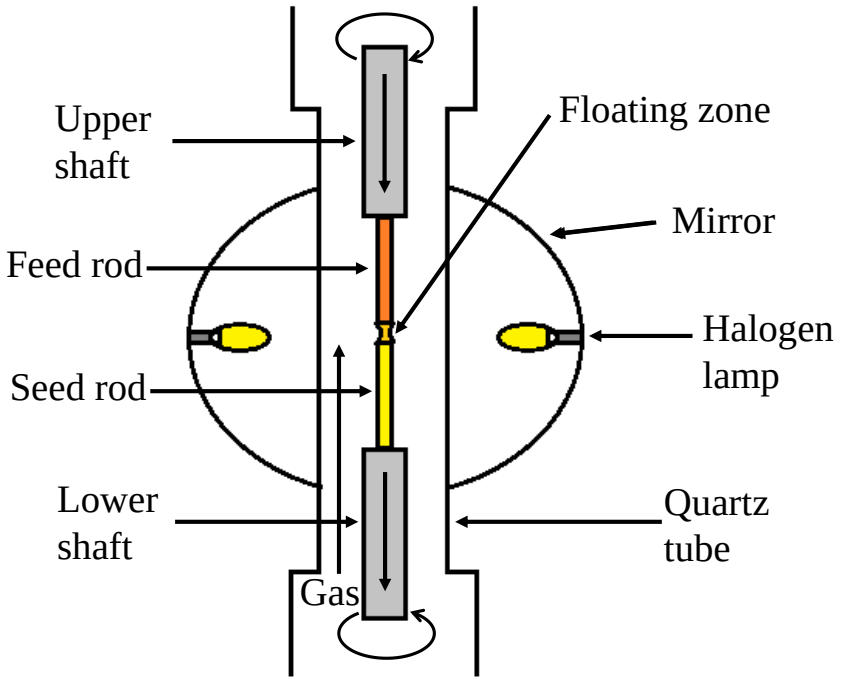

Figure 2.1: The illustration of IR-image furnace and floating zone method.

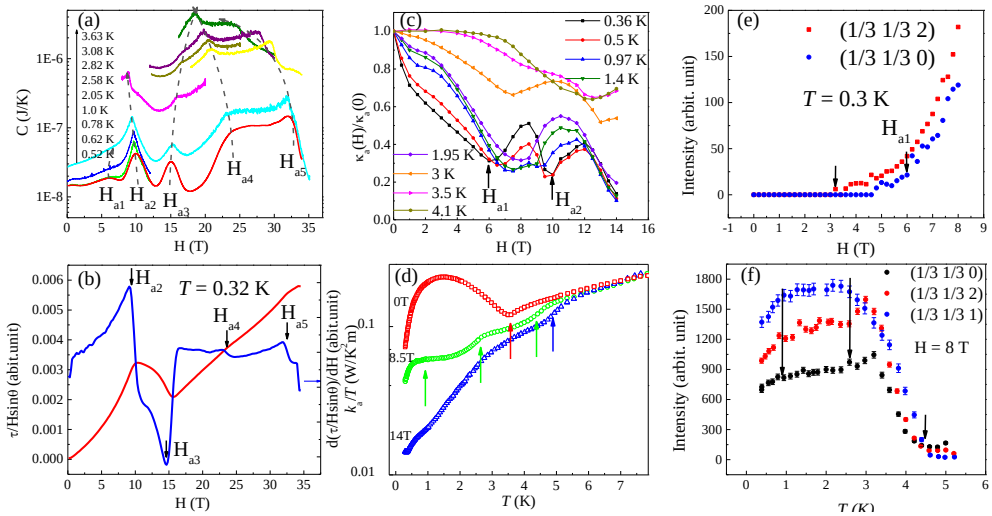

Figure 3.1: For all data, H ∥ a-axis. Field dependence of C_p (a) and τ (b); Field dependence (c) and temperature dependence (d) of κ;(e) Field dependence of the peak intensity for magnetic Bragg peaks [1/3 1/3 0] and [1/3, 1/3, 2] measured by neutron diffraction; (f) Temperature dependence of the peak intensity for [1/3, 1/3, 0], [1/3, 1/3, 1] and [1/3, 1/3, 2].

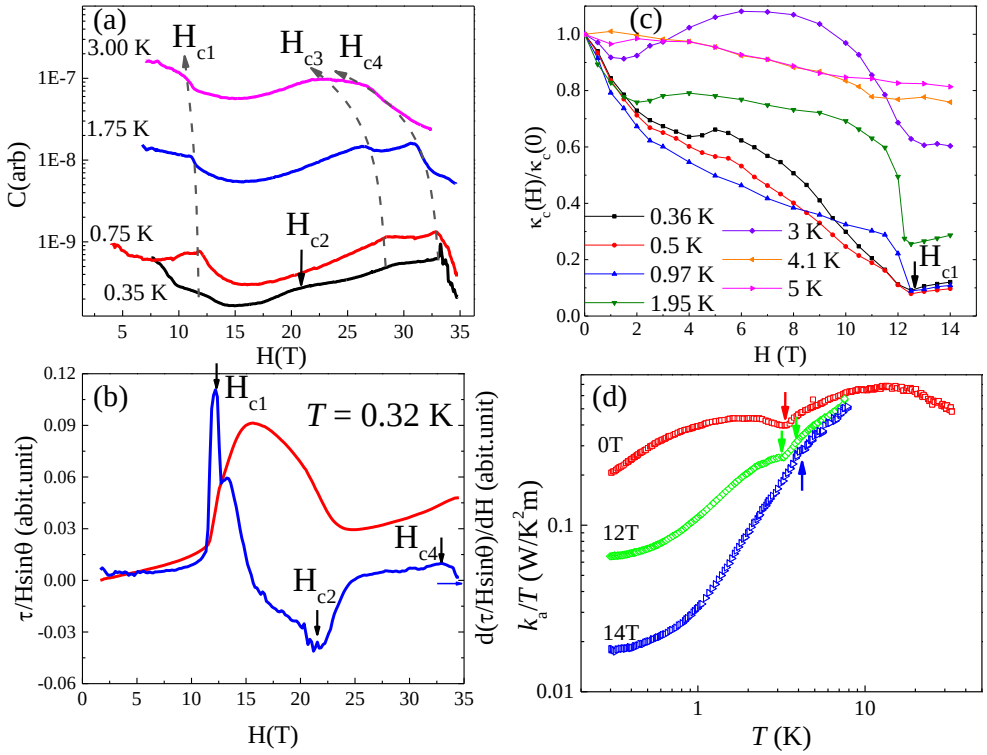

Figure 3.2: For all data, H ∥ c-axis. Field dependence of C_p (a) and τ (b); Field dependence (c) and temperature dependence (d) of κ.

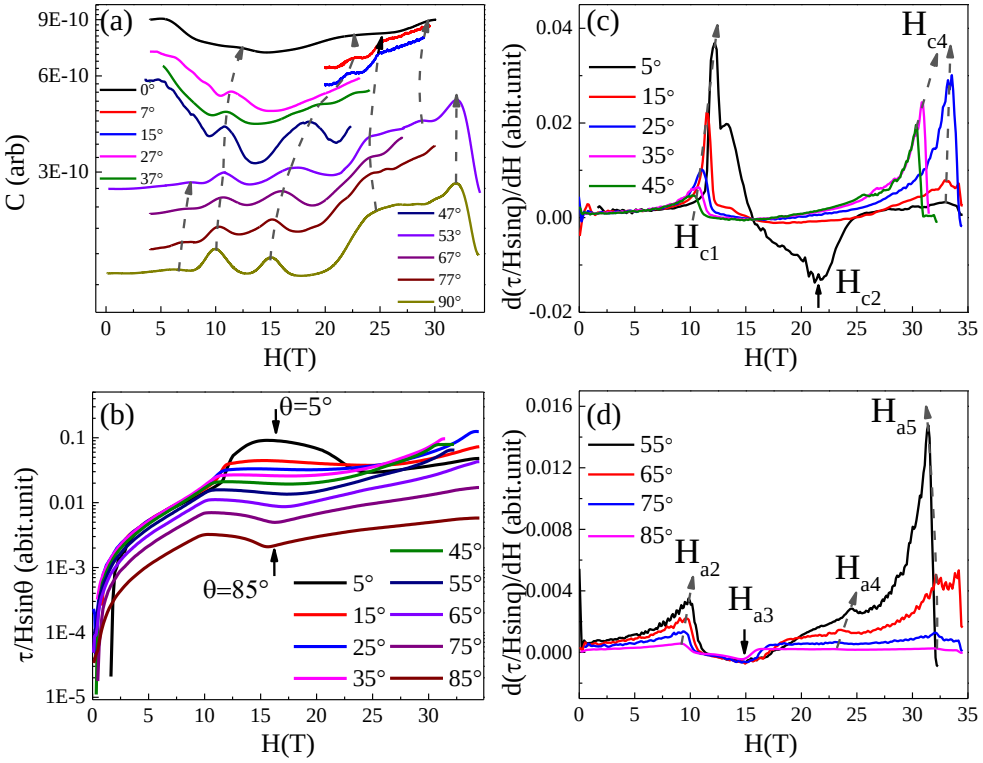

Figure 3.3: Field dependence of C_p (a), τ (b) and its derivative (c) and (d) when H rotates from a-axis (90°) to c-axis (0°). All data were obtained at $T = 0.32$ K.

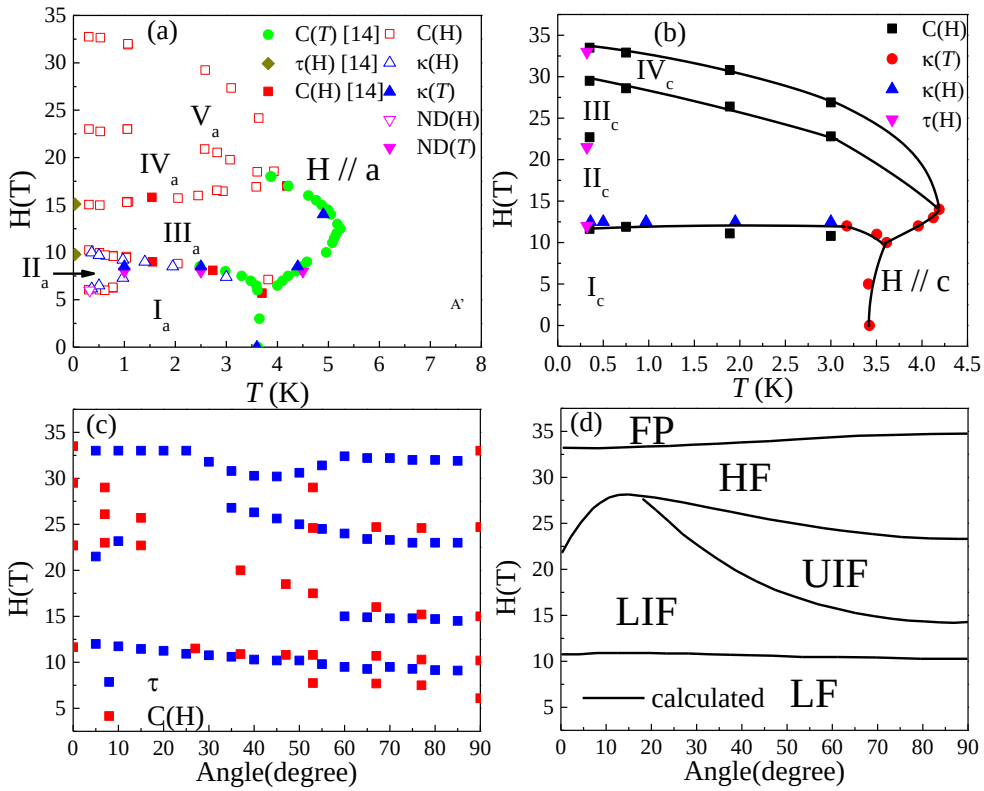

Figure 3.4: (a) The magnetic phase diagram with H ∥ a-axis. (b) The magnetic phase diagram with H ∥ c-axis. (c) The angle-dependent phase diagram at 0.32 K based on experiment data. The x-coordinate represents the angle between the a and c-axis; (d) the theoretically calculated phase boundaries.

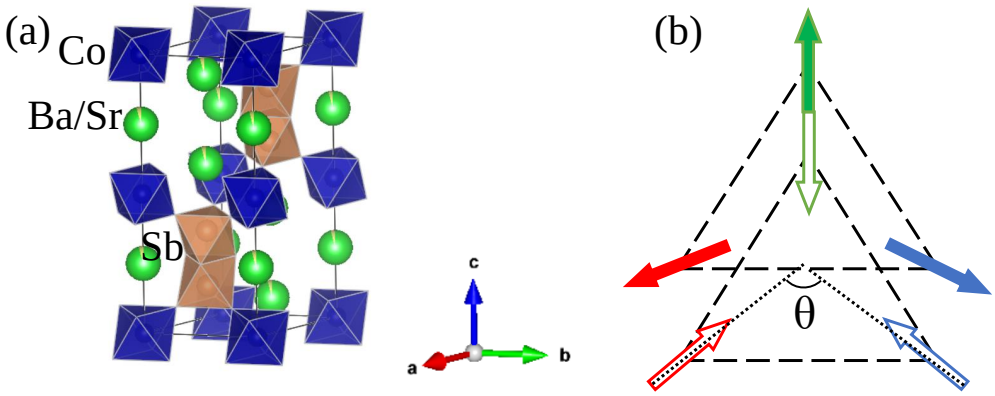

Figure 4.1: (a) An illustration of the crystallographic structure of Sr-BCSO. (b) An illustration of the canted 120-degree spin structure.

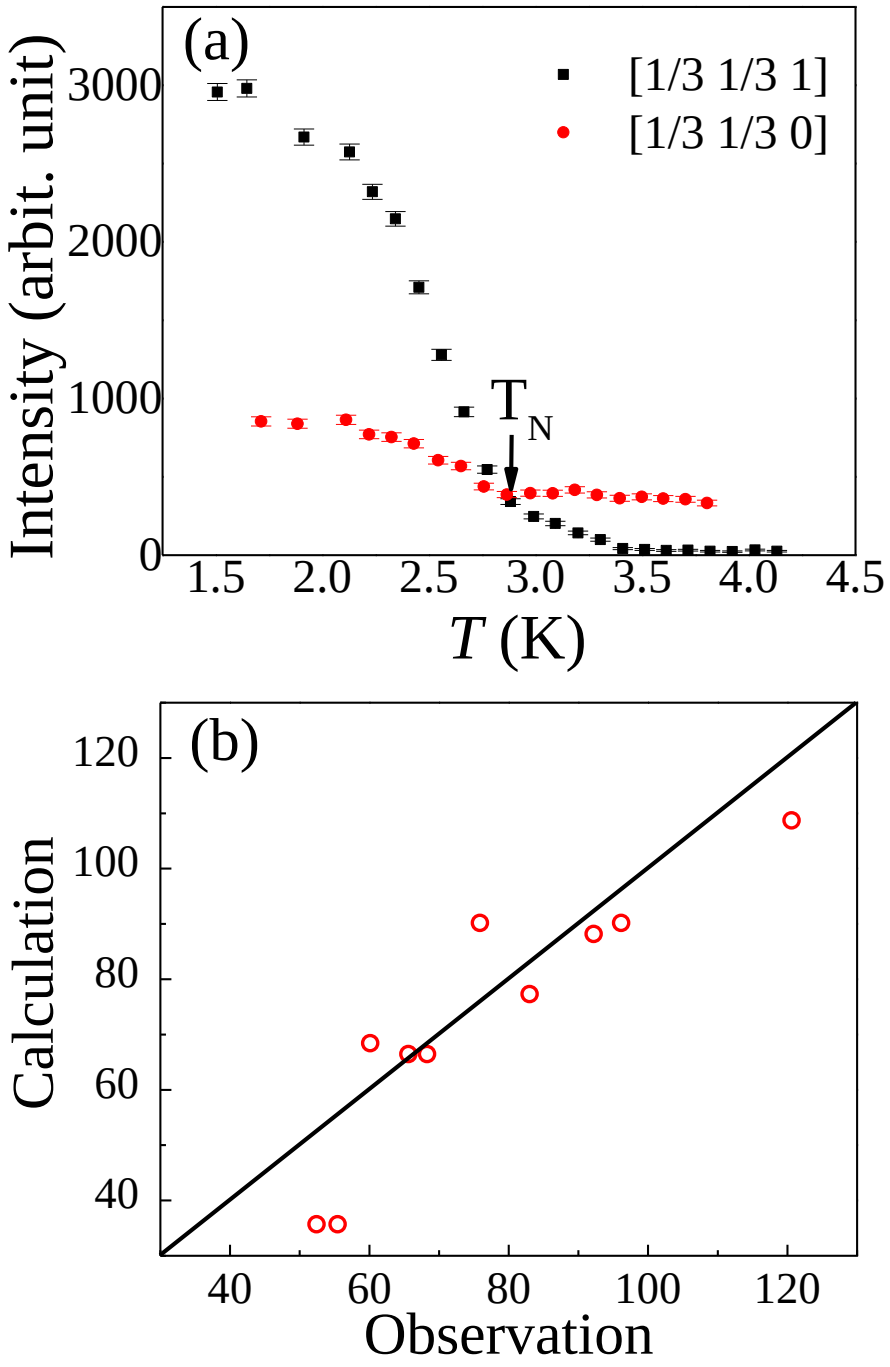

Figure 4.2: (a) The temperature dependence of the intensity for a magnetic peak [1/3 1/3 1] and [1/3 1/3 0]. The intensity of [1/3 1/3 0] is timed by a factor 20 for the visibility. Error bars represent one standard deviation. (b) The refinement result of the single crystal neutron diffraction data with a canted 120-degree spin structure.

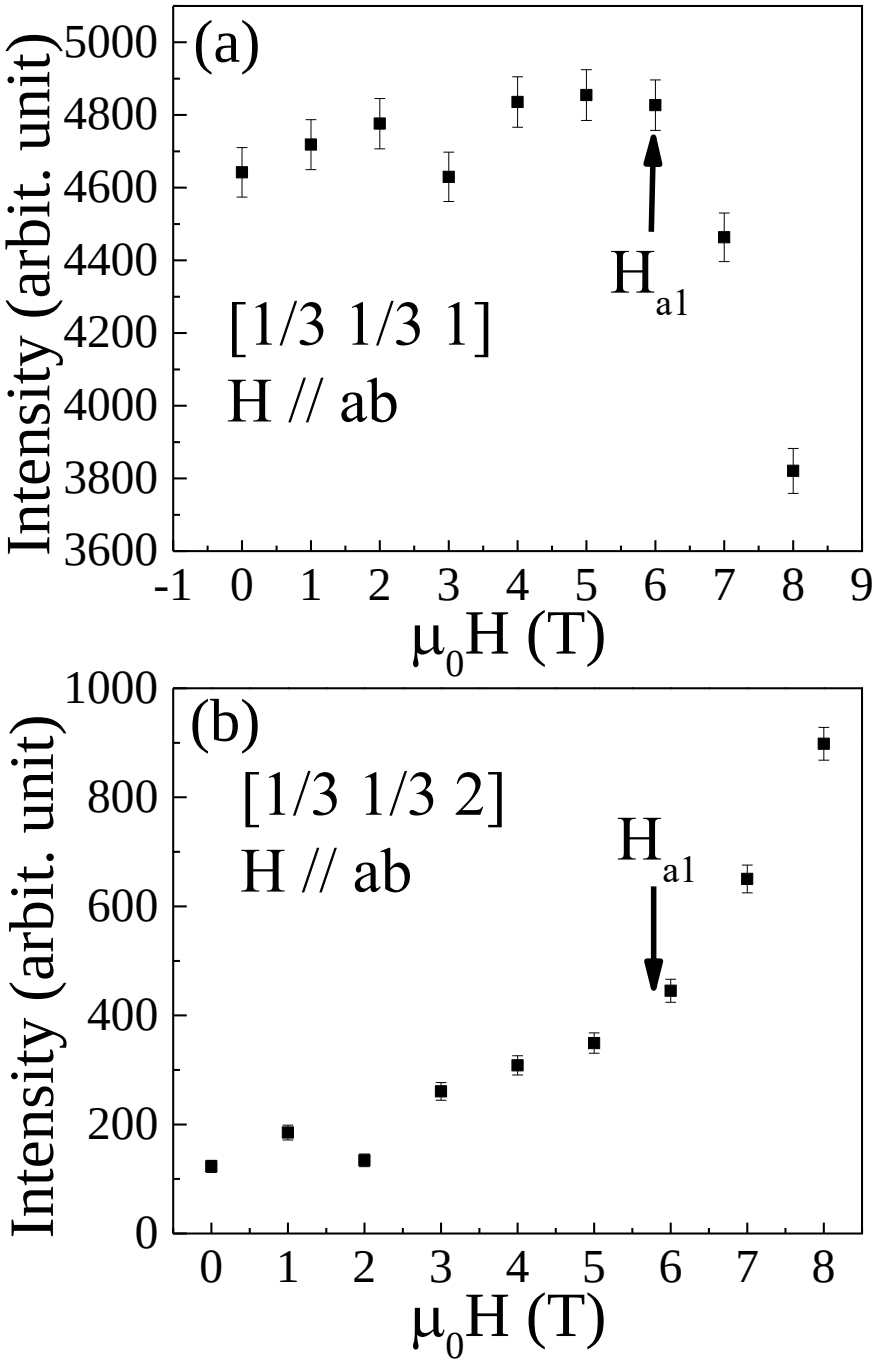

Figure 4.3: The field dependence of the intensity for magnetic peak [1/3 1/3 1] (a) and [1/3 1/3 2] (b) measured at 1.5 K. Error bars represent one standard deviation.

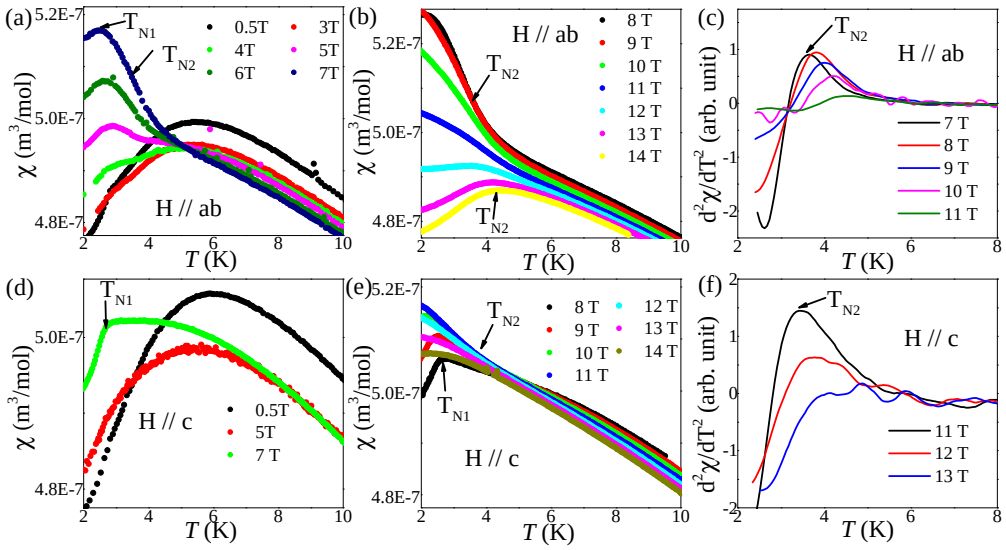

Figure 4.4: The temperature dependence of the DC susceptibility under different magnetic fields with H ∥ ab-plane (a, b) and H ∥ c-axis (d, e) for Sr-BCSO. The second-order derivative of the χ-T curves under high magnetic fields for H ∥ ab-plane (c) and H ∥ c-axis (f).

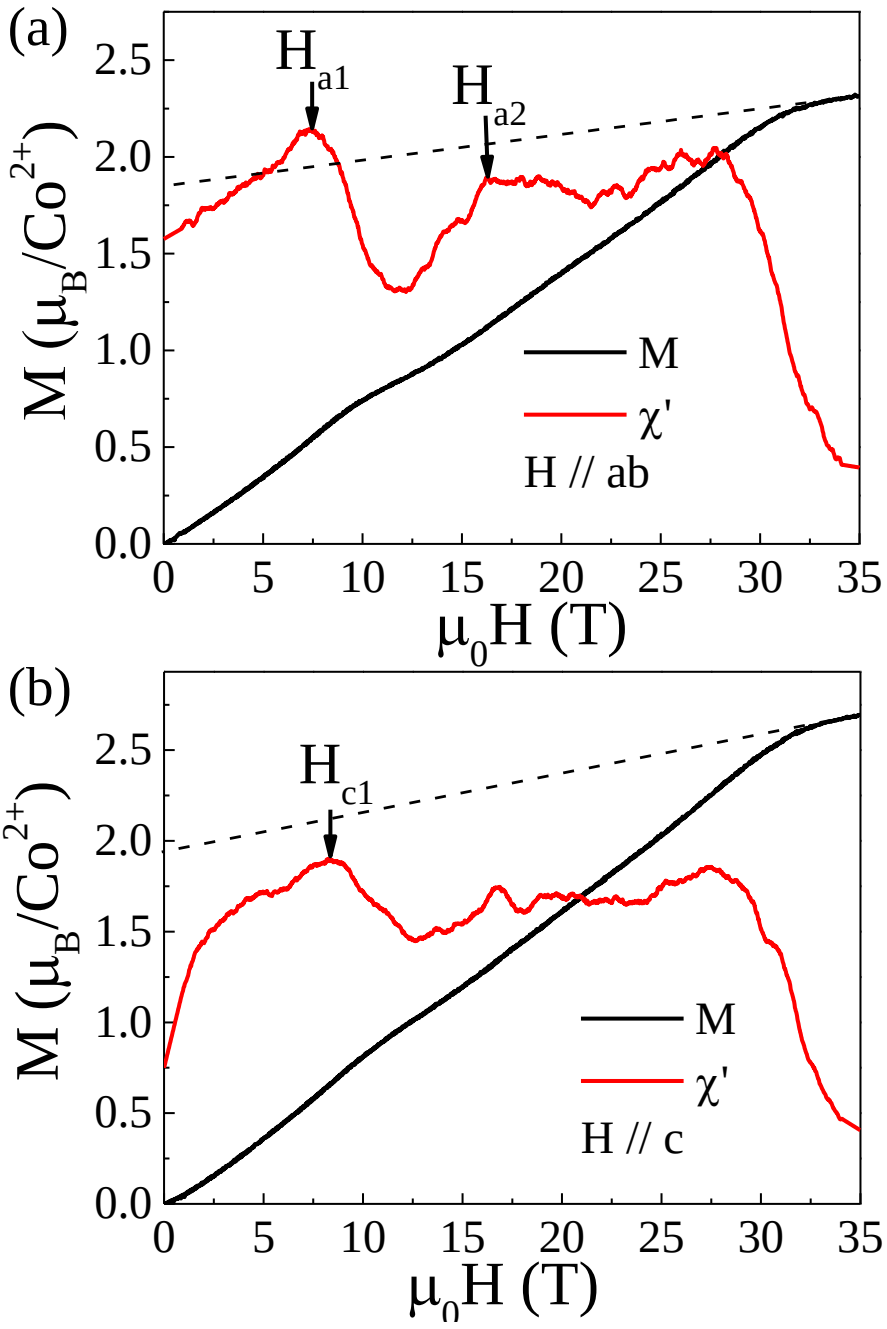

Figure 4.5: The dc magnetization (black line) and its derivative (red line) measured at 1.5 K with H ∥ ab-plane (a) and H ∥ c-axis (b). The dashed line represents the Van Vleck paramagnetic background.

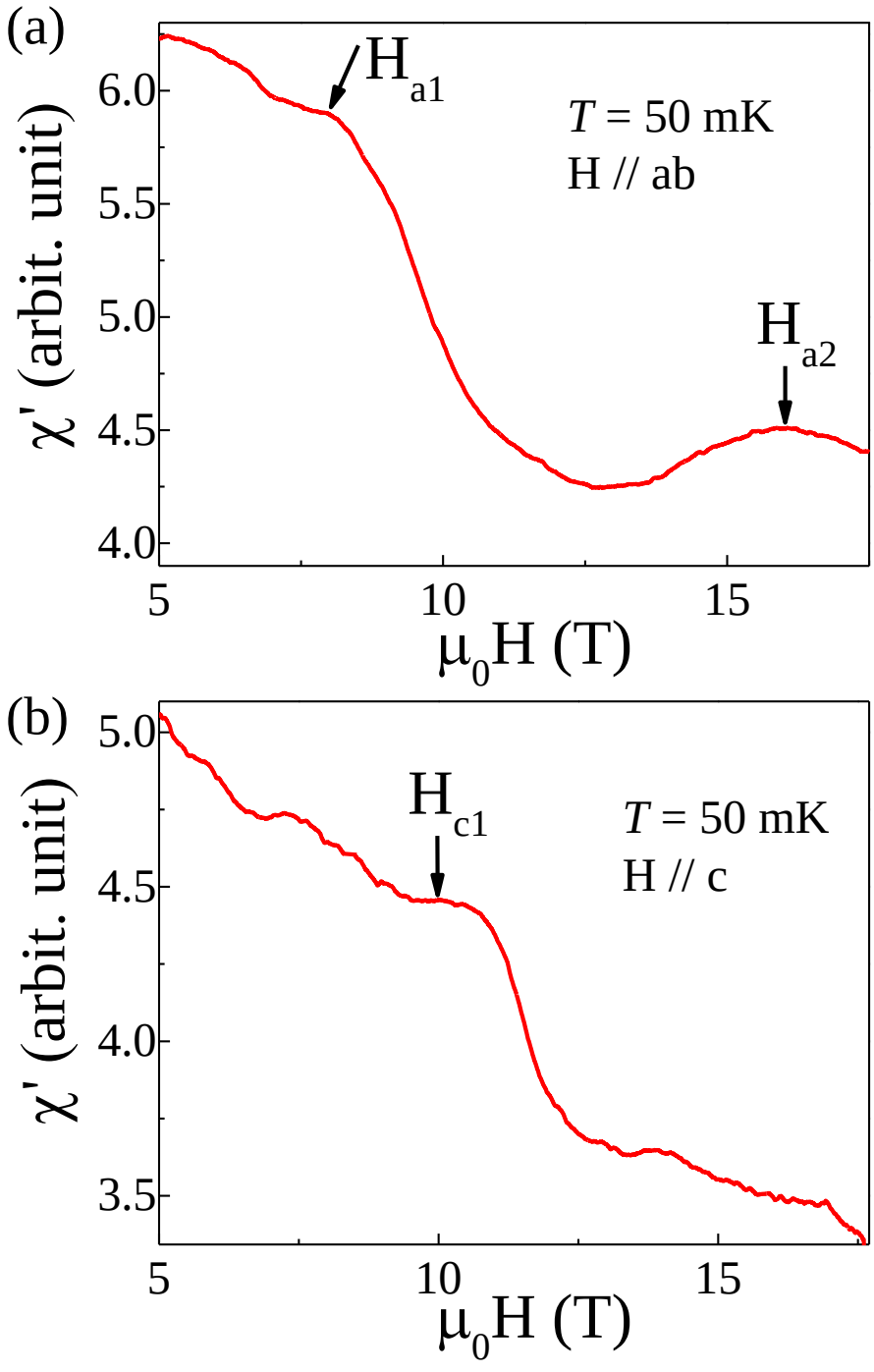

Figure 4.6: The AC susceptibility measured at 50 mK with H ∥ ab-plane (a) and *c*-axis (b).

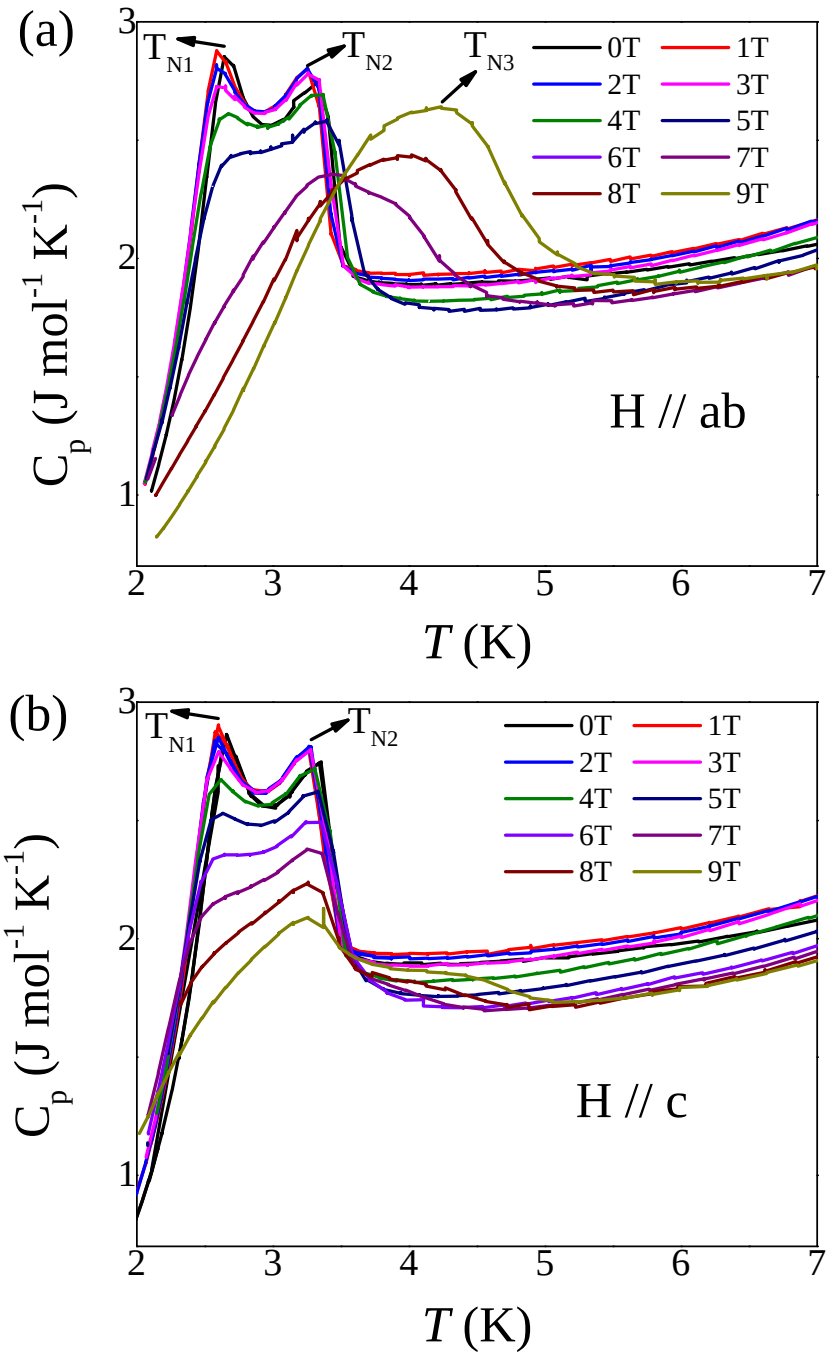

Figure 4.7: The temperature dependence of C_p measured with H ∥ ab-plane (a) and H ∥ c-axis (b).

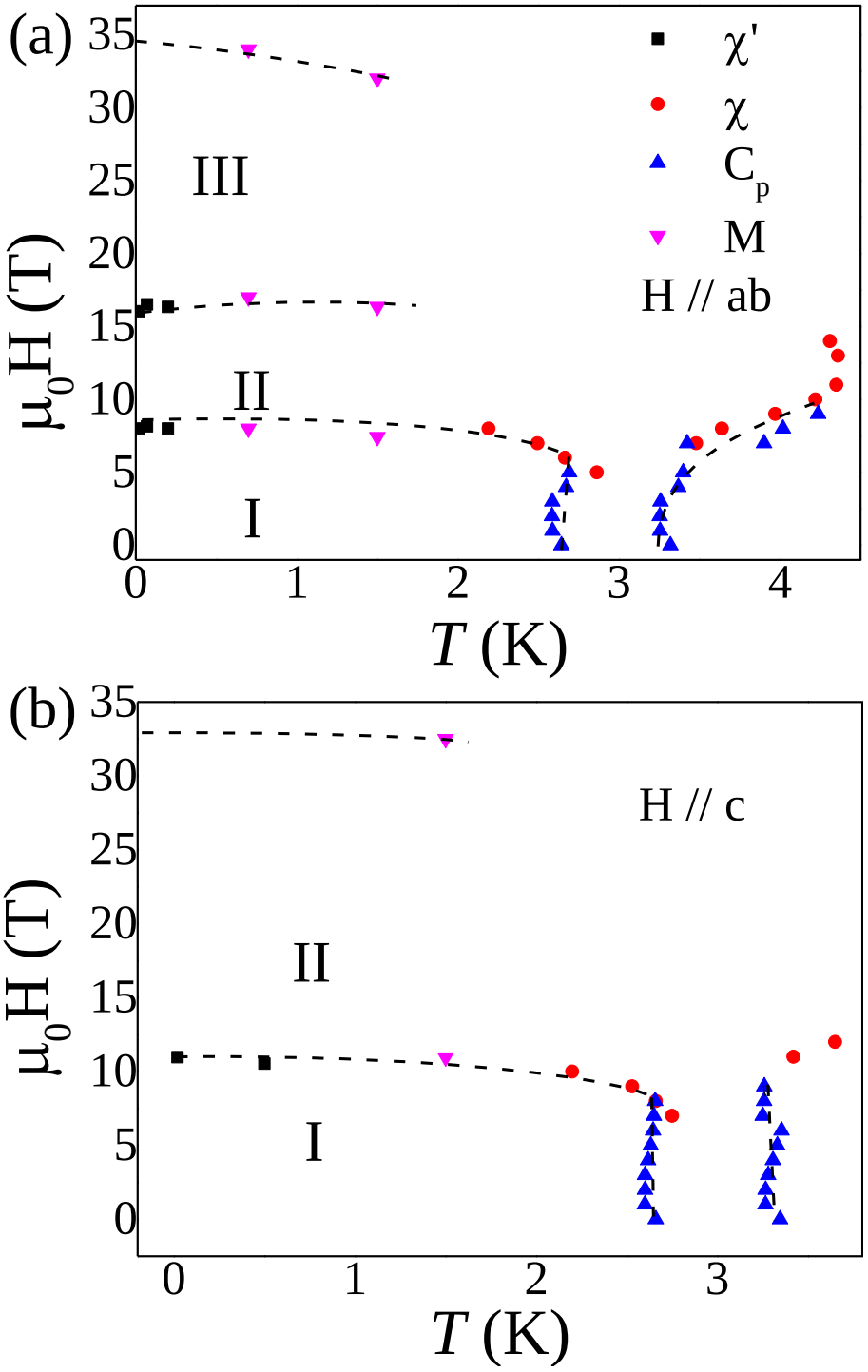

Figure 4.8: The magnetic phase diagram for H ∥ ab-plane (a) and H ∥ c-axis (b).

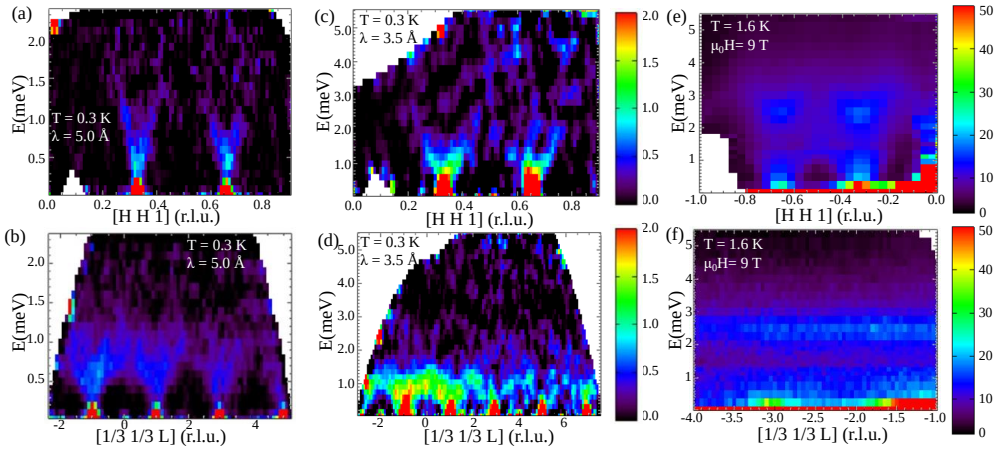

Figure 4.9: The zero field INS spectra along the [H H 1] (a) and [1/3 1/3 L] (b) directions, which were measured at 300 mK using the wavelength $\lambda = 5\,\text{Å}$; For (c, d), the zero field INS spectra were measured at 300 mK using the wavelength $\lambda = 3.5\,\text{Å}$. The INS spectra measured at 1.6 K with H $\parallel$ ab-plane and $\mu_0 H = 9$ T along [H H 1] (e) and [1/3 1/3 L] (f) directions.

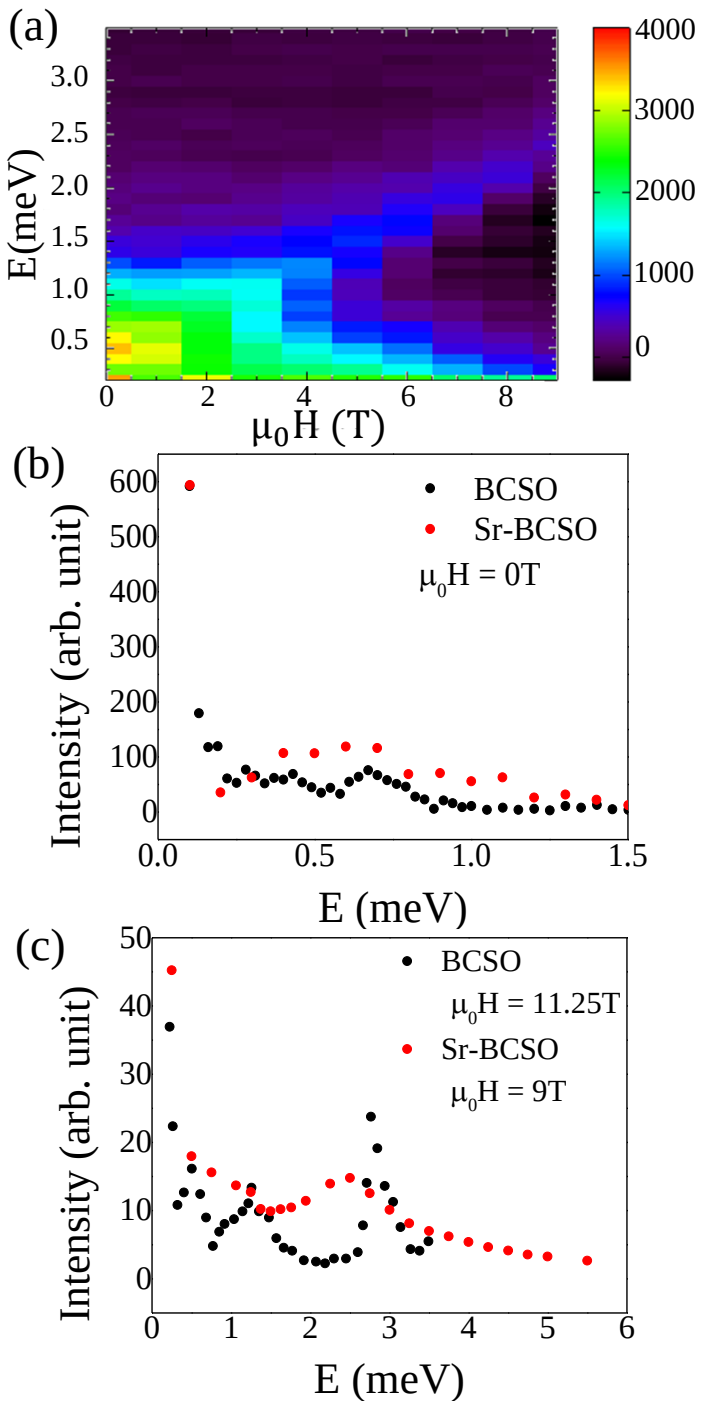

Figure 4.10: (a) The energy cut at [1/3 1/3 1] as the function of magnetic field with H ∥ ab-plane. Comparison of the energy cut between Sr-BCSO and BCSO at the [1/3 1/3 1] position at zero field (b) and applied field (c), which is 9 T for Sr-BCSO and 11.5 T for BCSO.

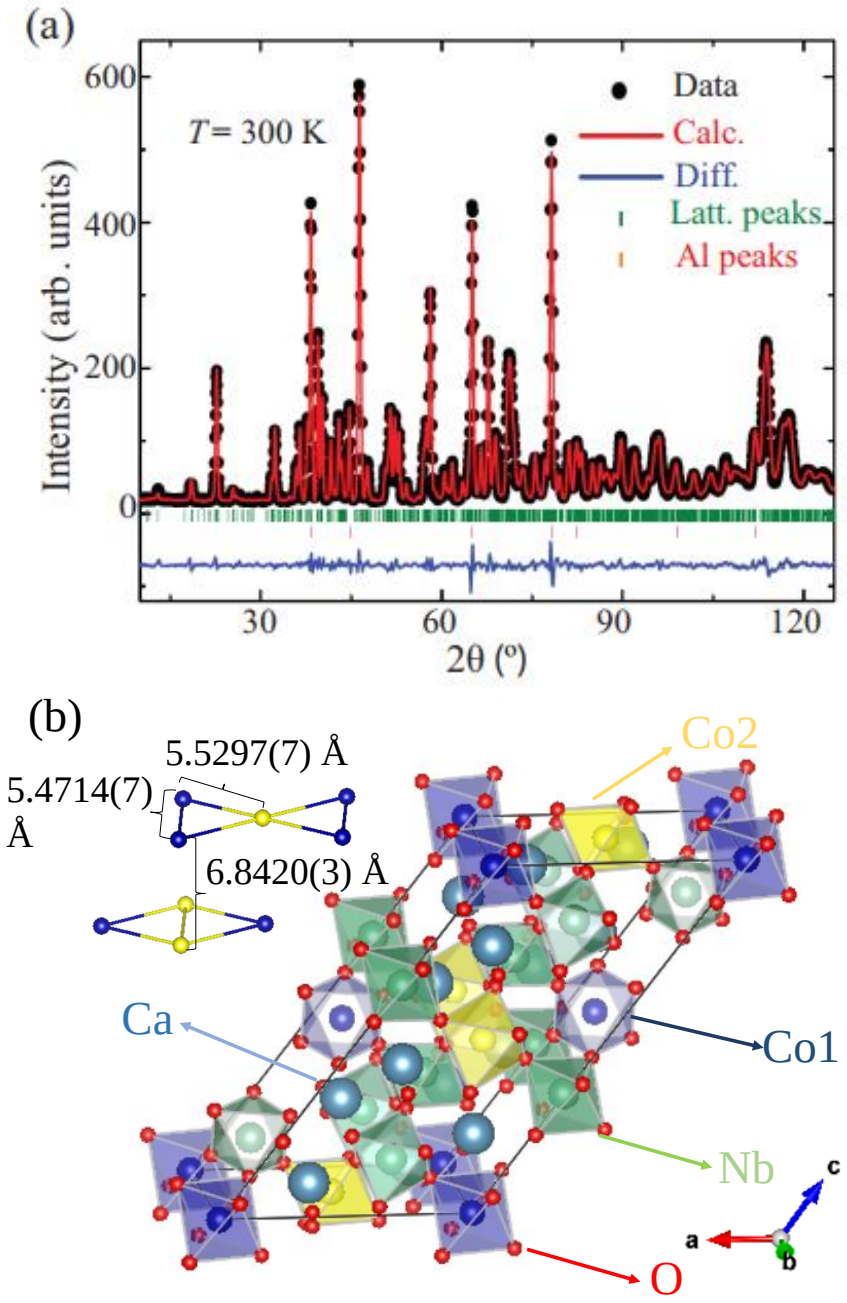

Figure 5.1: (a) Neutron diffraction patterns (black dots) and Rietveld refinements (red line) for CCNO at 300 K. Blue line at the bottom of each panel is the difference curve. The green and red ticks are the reflection positions for the nuclear phases and Al-can, respectively. The refinements were done with the P121/c1 space group. (b) The lattice structure with the Co-triangular lattice of CCNO. The blue and yellow spheres represent Co1 and Co2 on two different sites, respectively.

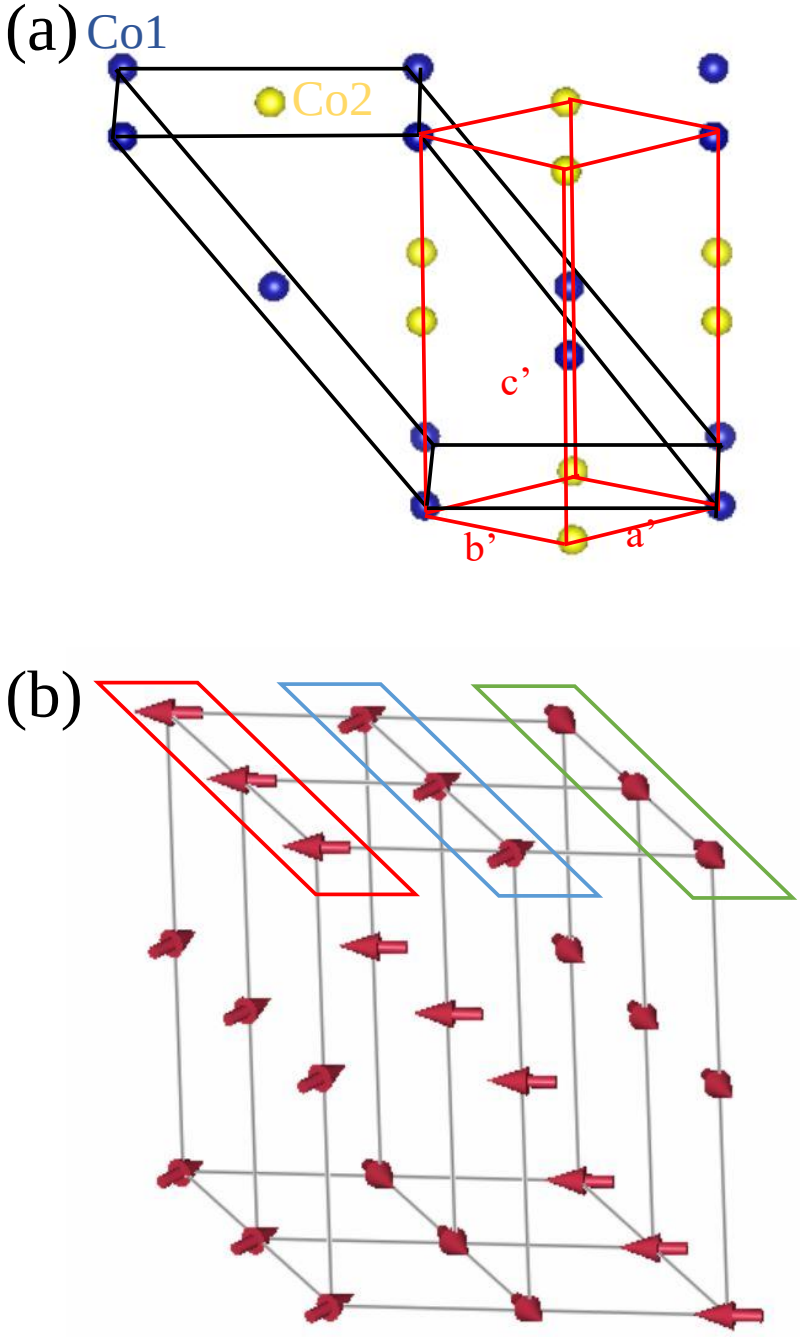

Figure 5.2: (a) Illustration of the transform of the unit cell from monoclinic (blue) to hexagonal (red) for CCNO. Here only the Co1 (blue sphere) and Co2 (yellow sphere) are plotted. (b) An illustration of spin structure proposed for CCNO.

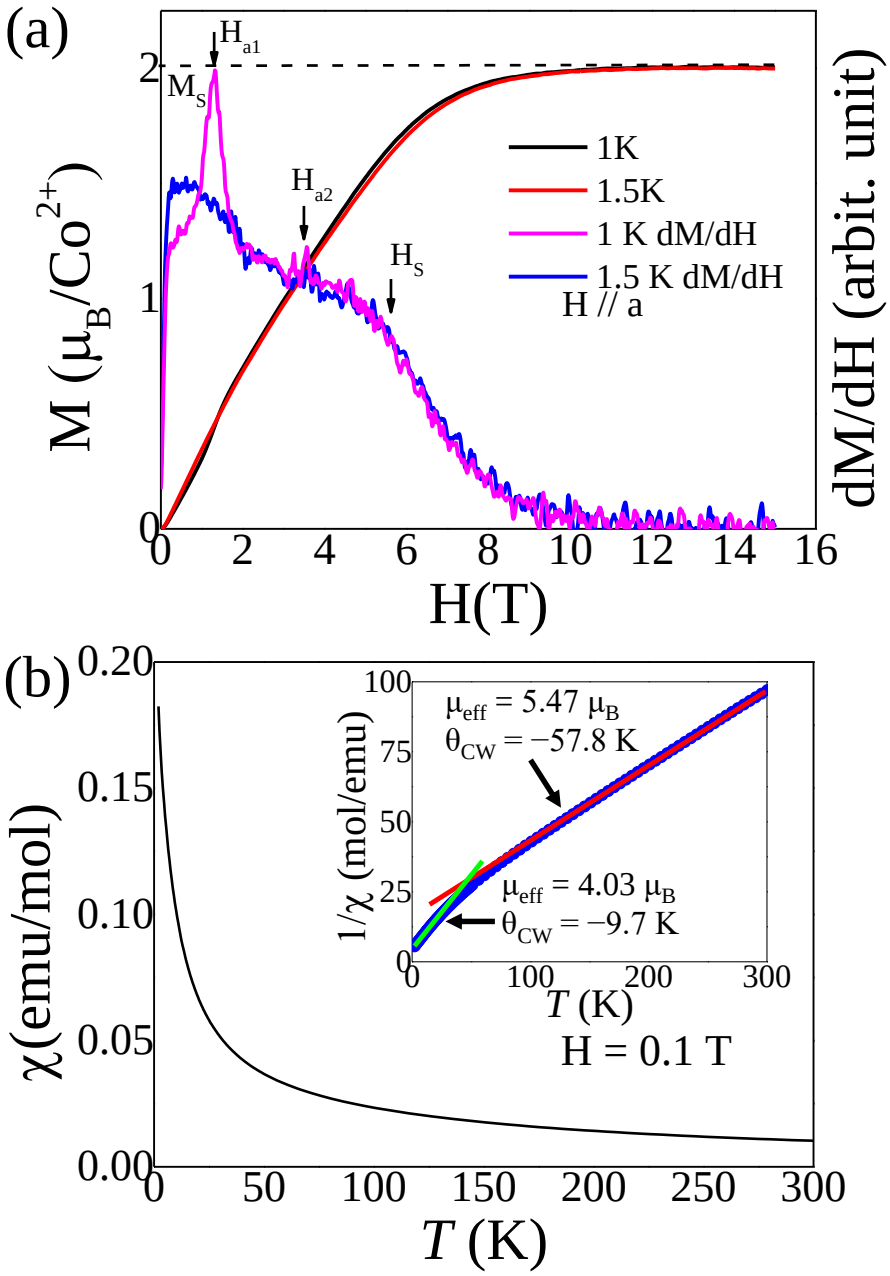

Figure 5.3: (a) The isothermal dc magnetization curve and its derivative (dM/dH) of CCNO measured at 1.0 K and 1.5 K with H ∥ a-axis. (b) Temperature dependence of the dc susceptibility measured at 0.1 T. Inset: the inverse dc susceptibility. The lines are Curie-Weiss fittings at two different temperature regions ($T \leq 50$ K for the green line and 100 K $\leq T \leq 300$ K for the red line).

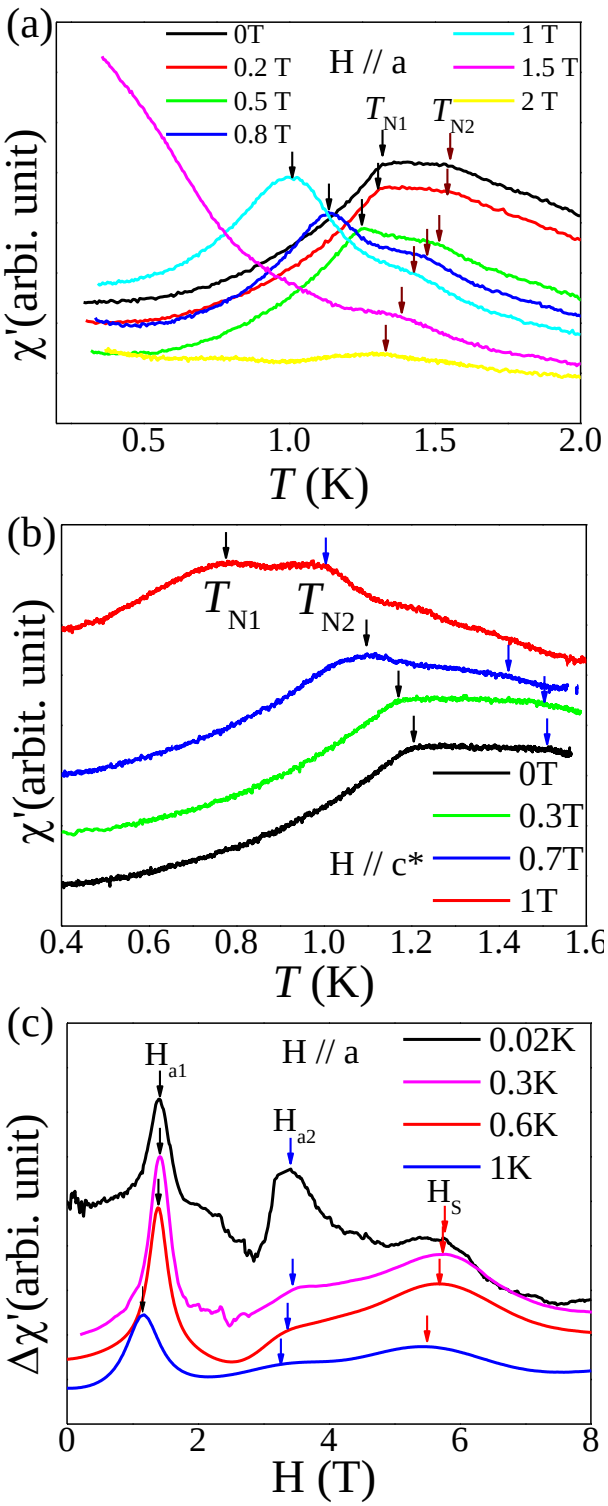

Figure 5.4: (a) The temperature dependence of ac susceptibility measured with dc field H ∥ a-axis. (b) The temperature dependence of ac susceptibility measured with dc field H ∥ c*-axis. (c) The field dependence of ac susceptibility with the dc field H ∥ a-axis.

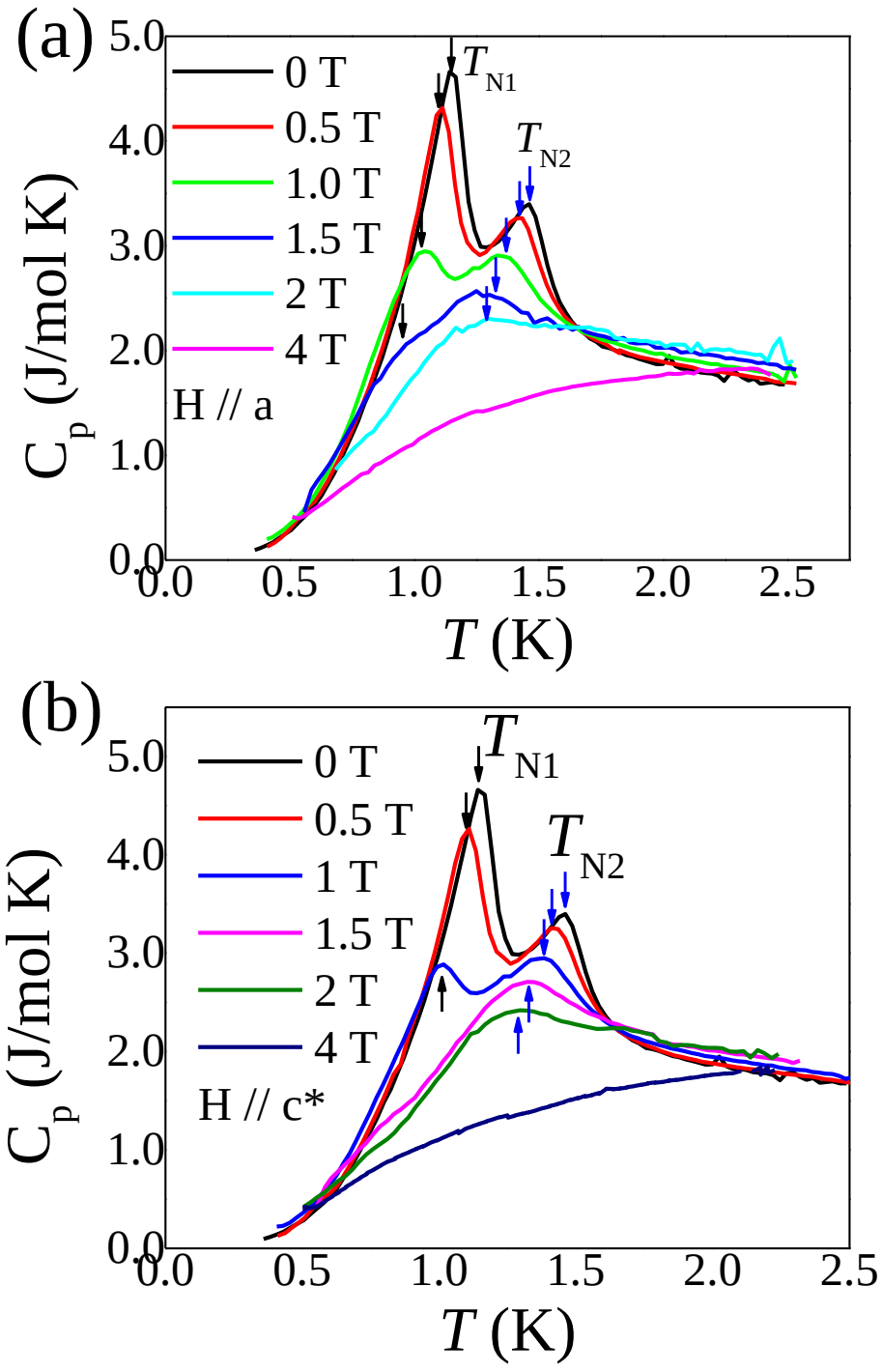

Figure 5.5: The temperature dependence of specific heat of CCNO with H ∥ a-axis (a) and H ∥ c*-axis (b).

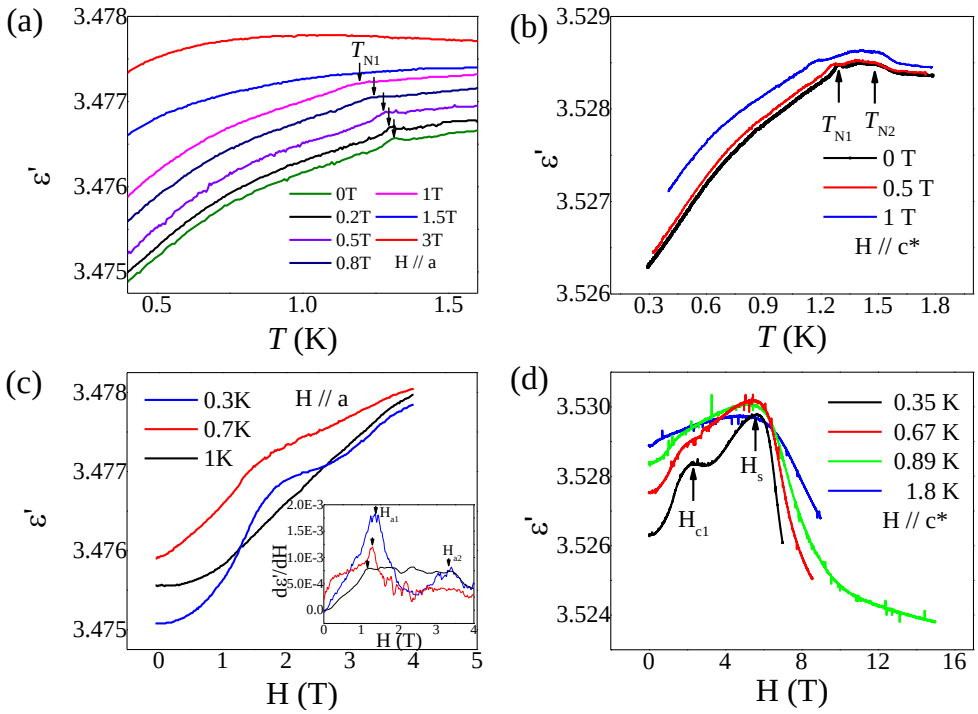

Figure 5.6: Temperature dependence of $\epsilon'(T)$ of CCNO at different fields with H $\parallel$ a (a) and H $\parallel$ c*-axis (b). Data was offset by 0.003. The field dependence of ϵ'(H) at different temperatures with H $\parallel$ a-axis (c) and H $\parallel$ c*-axis(d). Inset of (c): the derivative of the ϵ' with respect field.

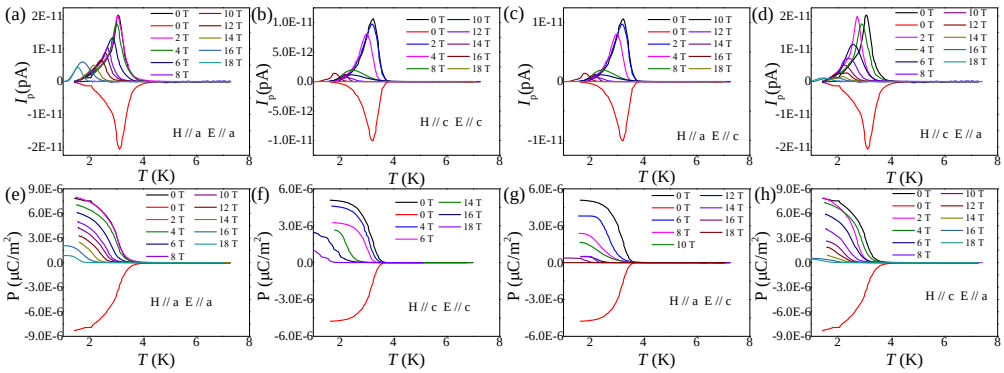

Figure 5.7: (a)-(d) Temperature dependence of the pyroelectric current of CNNO with H and E applied along the different crystallographic directions. (e)-(h) Temperature dependence of polarization of CNNO with H and E applied along different directions.

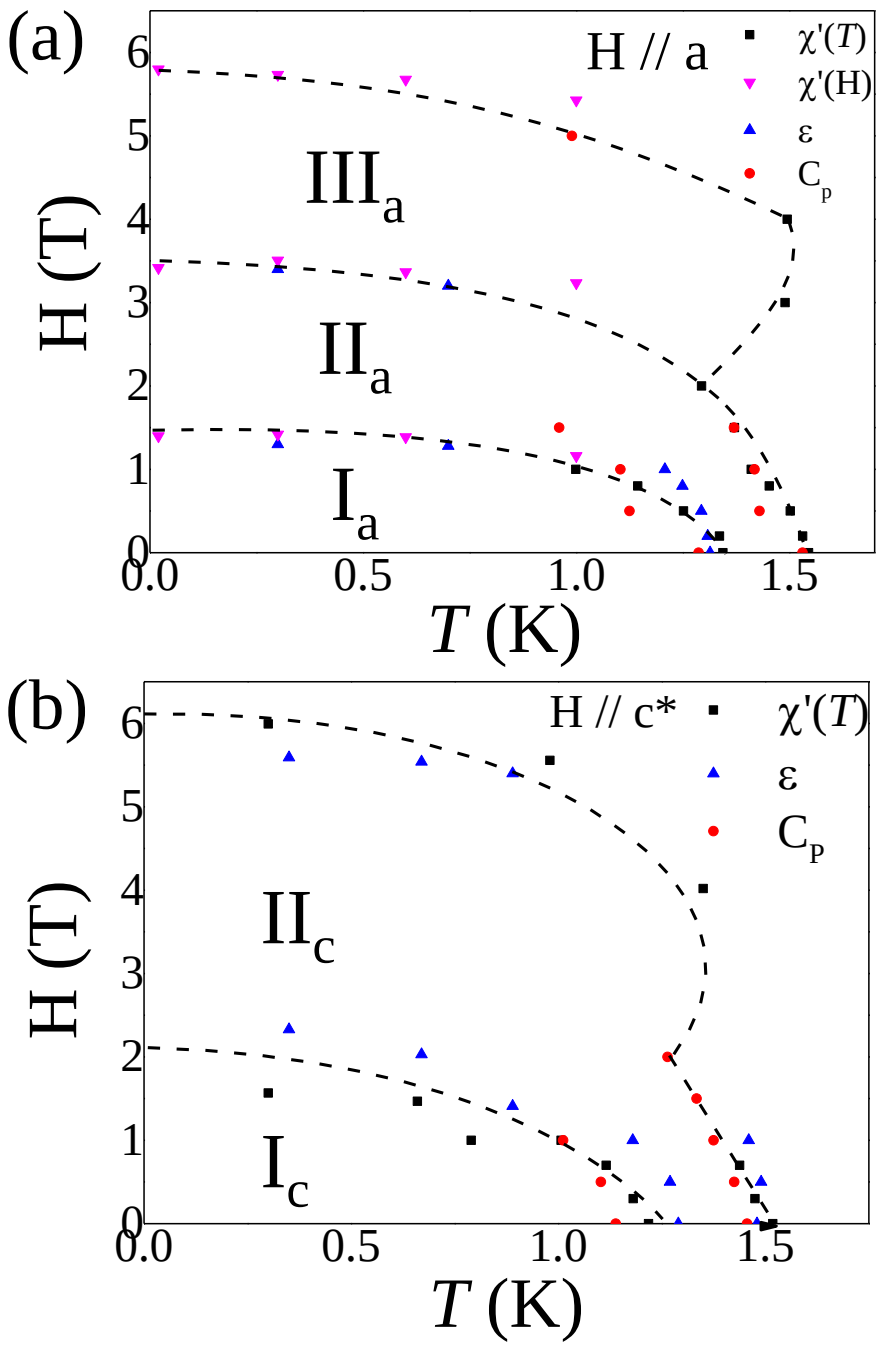

Figure 5.8: The magnetic phase diagrams of CCNO with H ∥ a-axis (a) and H ∥ c*-axis (b).

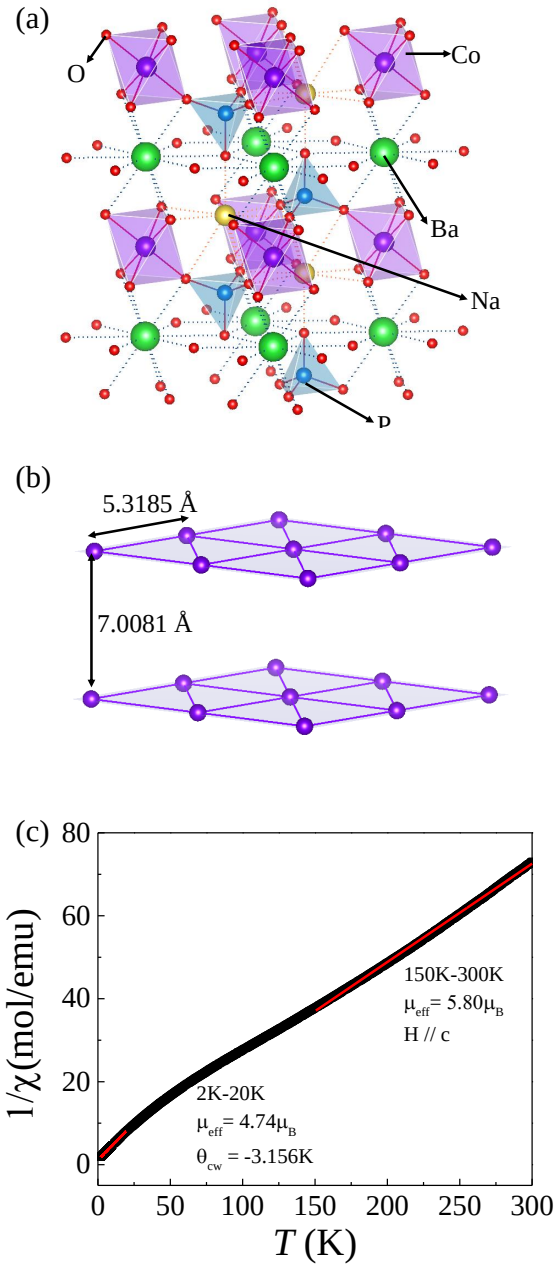

Figure 6.1: (a) The crystallographic structure. (b) The triangular lattice of Co^{2+} ions in the ab plane. (c) The inverse of the DC susceptibility measured with 0.1 T magnetic field along the ab plane. The solid lines are the Curie–Weiss fittings to high temperature or low-temperature data.

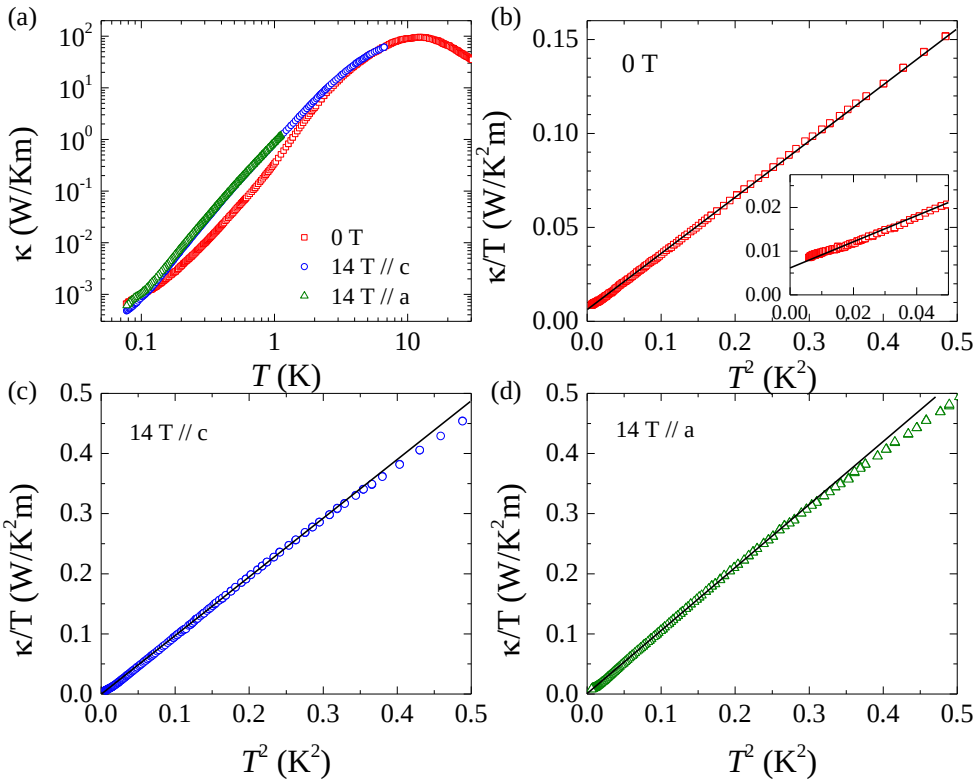

Figure 6.2: (a) The zero-field thermal conductivity of NBCPO in temperature range of 70 mK – 30 K. The heat current is along the a axis. The peak at 12 K is the so-called phonon peak. Also shown are the thermal conductivity in 14 T magnetic field along the c or the a axis. In most of this temperature region, high magnetic field enhances the thermal conductivity. (b) Data in zero field plotted in κ/T vs T^2. The solid line is a linear fit of the data at $T < 700$ mK. A nonzero residual thermal conductivity $\kappa_0/T = 0.0062$ WK^2 m^1 is resolved. The inset shows a magnified view of the lowest-temperature data. There is a very weak anomaly at $T < 100$ mK. (c), (d) Thermal conductivity in 14 T magnetic field plotted as κ/T vs T^2. The solid lines are a linear fits for data at $T < 550$ mK (for H $\parallel$ c) and at $T < 500$ mK (for H $\parallel$ a). There is no residual term ($\kappa_0/T = 0$).

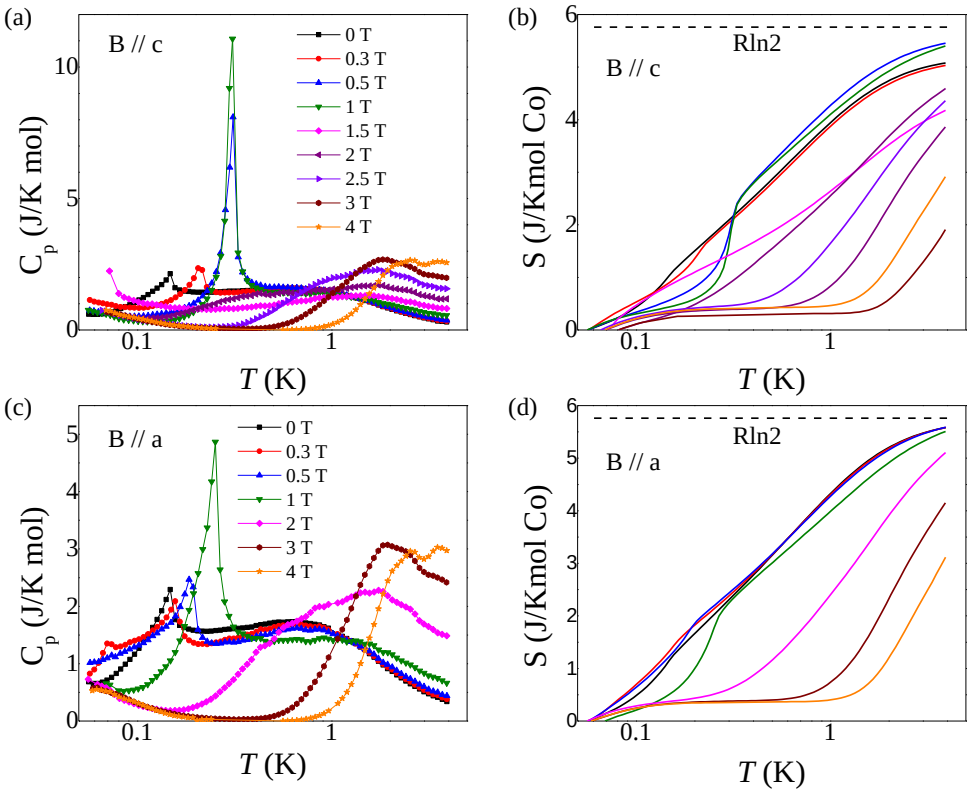

Figure 6.3: (a), (c) The zero-field data and those in different magnetic fields along the c axis or the a axis. The temperature range is 50 mK to 4 K. (b), (d) The magnetic entropy for H ∥ c and H ∥ a, obtained by integrating the magnetic specific heat.

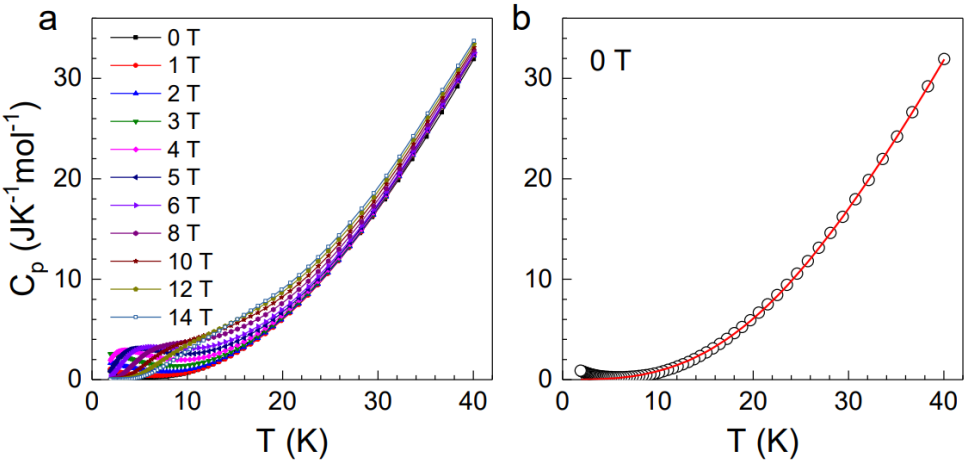

Figure 6.4: (a) Specific heat of NBCPO single crystal at 1.9 – 40 K and in various magnetic fields up to 14 T. (b) Zero-field data. The solid line shows the fitting to data at $T > 10$ K by using the formula of phonon specific heat, $C_{ph} = \beta T^3 + \beta_5 T^5 + \beta_7 T^7$.

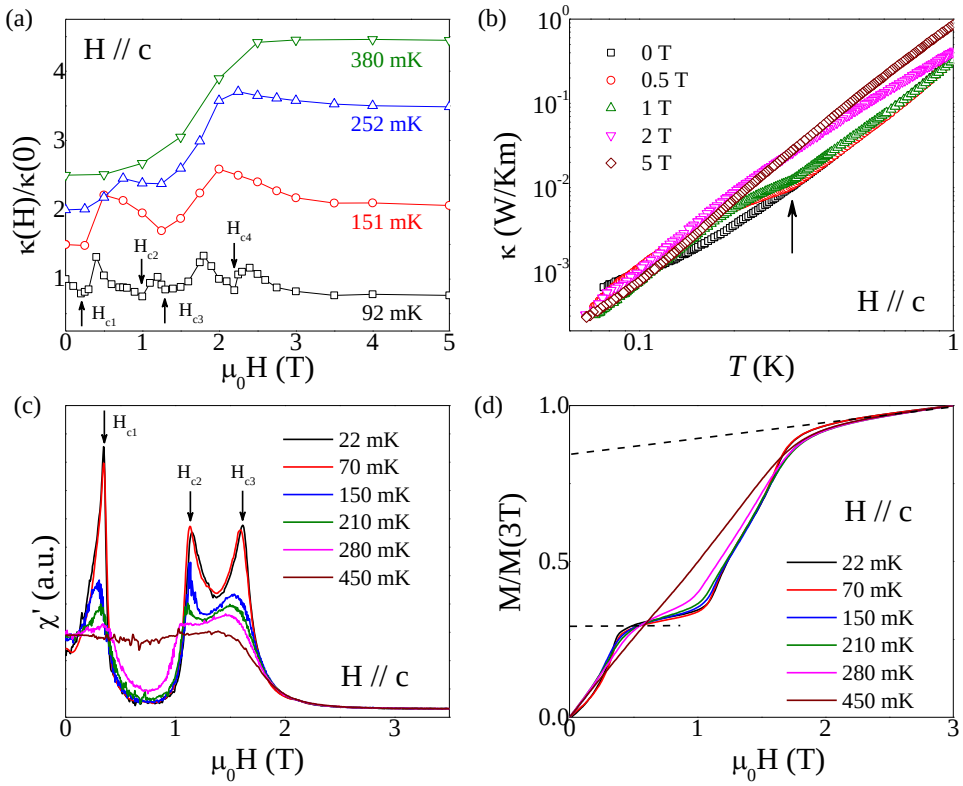

Figure 6.5: (a) Magnetic-field dependence of thermal conductivity at different temperatures. For clarifying, the 151 mK, 252 mK and 380 mK curves are shifted upward by 0.5, 1.0 and 1.5, respectively. At 92 mK, there are four minima indicated by arrows. With increasing temperature, the minima become weaker and disappear above 380 mK. (b) Temperature dependence of κ in different fields. At low fields of 0.5 and 1 T, there is a clear slope change of $\kappa(T)$ curves around 310 mK, which has good correspondence to the specific-heat anomaly. (c) AC magnetic susceptibility at different temperatures. There are three peaks in the low-temperature curves. (d) Magnetization curves obtained by integrating the AC susceptibility data and renormalized with the 3 T value. The lower dashed line indicates a $\sim$1/3 plateau and the upper dashed line indicates the Van Vleck paramagnetic background.

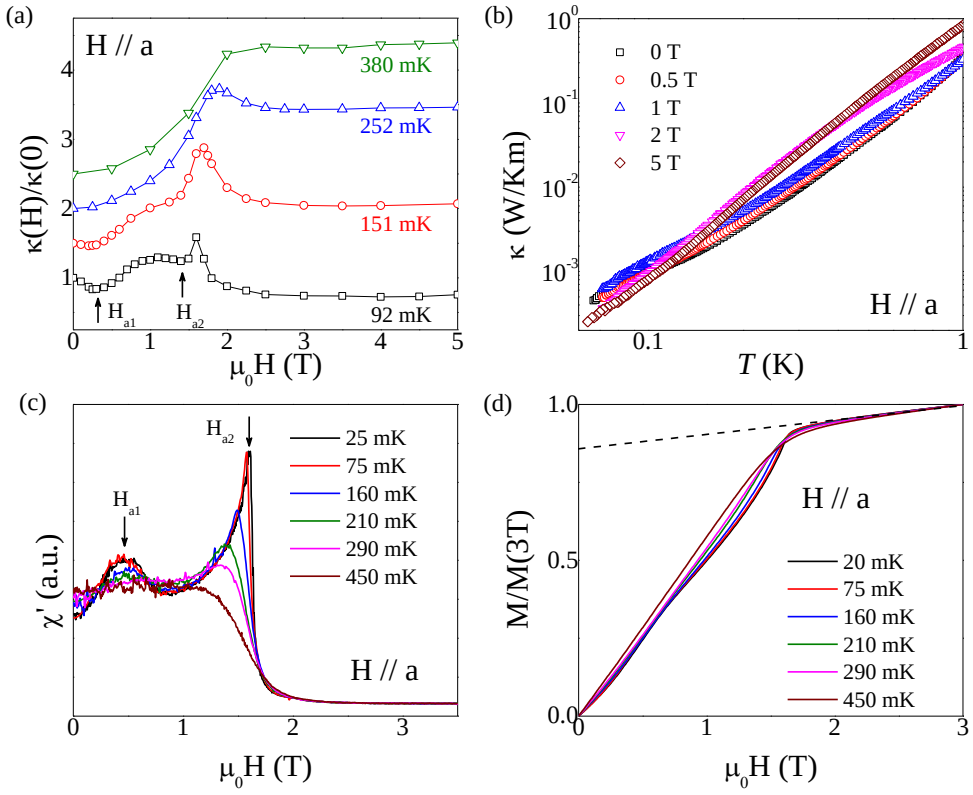

Figure 6.6: (a) Magnetic-field dependence of thermal conductivity at different temperatures. For clarifying, the 151 mK, 252 mK and 380 mK curves are shifted upward by 0.5, 1.0 and 1.5, respectively. At very low temperatures, there are two minima on the κ(H) curves which disappear above 252 mK. (b) Temperature dependence of κ in different fields. No clear anomaly is observed. (c) AC magnetic susceptibility at different temperatures. There are two peaks in the low-temperature curves. (d) Magnetization curves obtained by integrating the AC susceptibility data and renormalized with the 3 T value. The dashed line indicates the Van Vleck paramagnetic background.

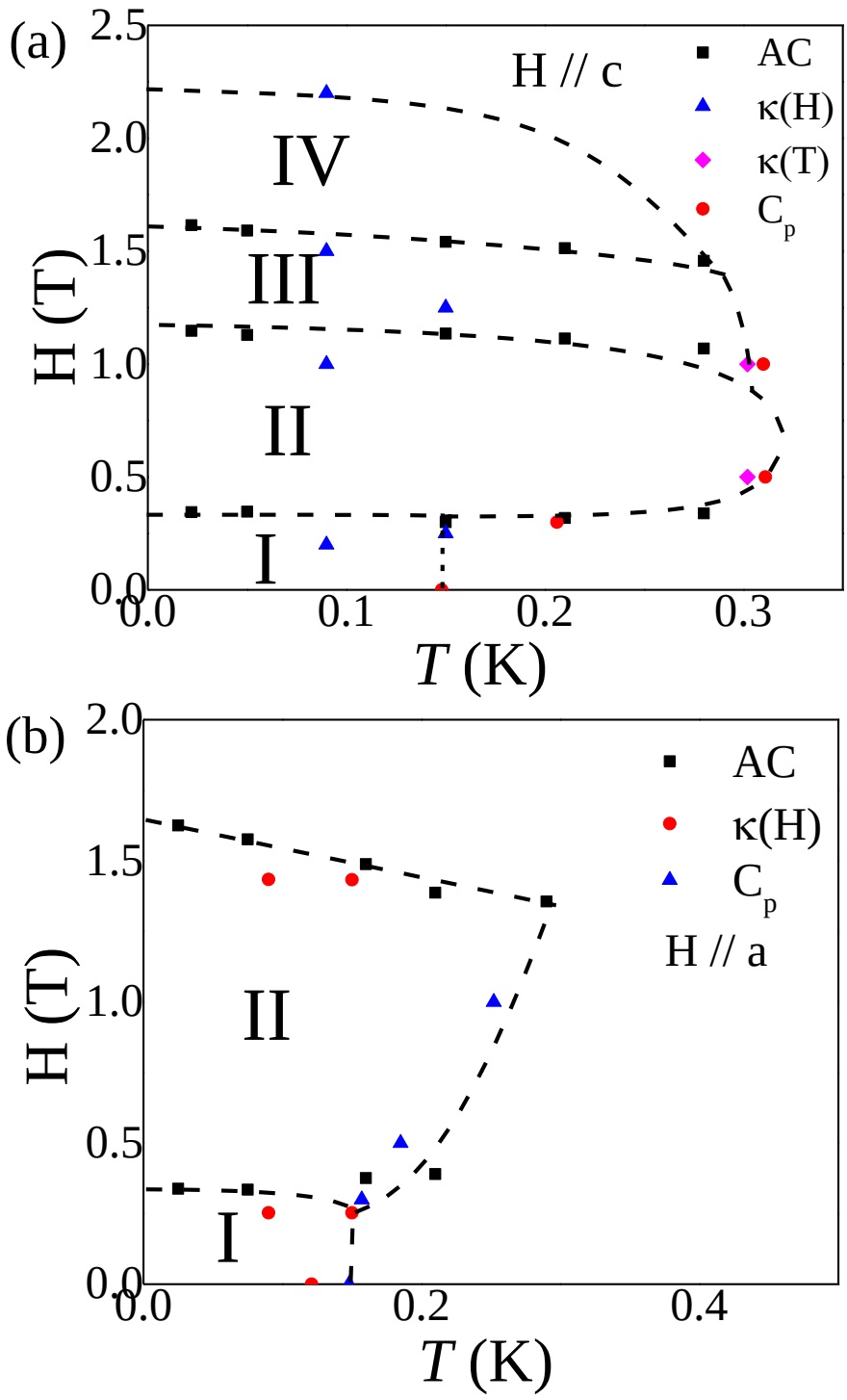

Figure 6.7: The magnetic phase diagrams of NBCPO for H ∥ c (a) and H ∥ a (b). The data points are obtained from the AC susceptibility (AC), specific heat (C_p) and temperature or field dependence of thermal conductivity ($\kappa(T)$ and κ(H)) measurements. The dashed lines are phase boundaries. For H ∥ c, there are four phases (I, II, III, and IV) in the low-temperature and low-field region. Whereas, there are two phase (I and II) at low-temperature and low-field for H ∥ a. The dashed lines are a guide to the eye.

Vita

Qing Huang was born on July 16th, 1993, in Anhui, China. He graduated from No. 2 High School Attached to East China Normal University in Shanghai, 2011. Then he joined the University of Science and Technology of China and received a B.S. in physics in 2015. In the August of the same year, he came to U.S. to pursue a Ph.D in condensed matter physics at the University of Tennessee, Knoxville. He has worked as a research assistant for six years in the group of Dr. Haidong Zhou. And he is expected to receive his Ph.D in May of 2022.